Dynamic Radiative Thermal Management and Optical Force Modulation with Tunable

Nanophotonic Structures Based on Thermochromic Vanadium Dioxide

by

Sydney Taylor

A Dissertation Presented in Partial Fulfillment
of the Requirements for the Degree
Doctor of Philosophy

Approved October 2020 by the
Graduate Supervisory Committee:

Liping Wang, Chair
Valana Wells
Hongbin Yu
Robert Wang
Jekanthan Thangavelautham
Christopher Massina

ARIZONA STATE UNIVERSITY

December 2020

ABSTRACT

This research focuses mainly on employing tunable materials to achieve dynamic radiative properties for spacecraft and building thermal management. A secondary objective is to investigate tunable materials for optical propulsion applications. The primary material investigated is vanadium dioxide (VO_2), which is a thermochromic material with an insulator-to-metal phase transition. VO_2 typically undergoes a dramatic shift in optical properties at T = 341 K, which can be reduced through a variety of techniques to a temperature more suitable for thermal control applications.

A VO_2-based Fabry-Perot variable emitter is designed, fabricated, characterized, and experimentally demonstrated. The designed emitter has high emissivity when the radiating surface temperature is above 345 K and low emissivity when the temperature is less than 341 K. A uniaxial transfer matrix method and Bruggeman effective medium theory are both introduced to model the anisotropic properties of the VO_2 to facilitate the design of multilayer VO_2-based devices. A new furnace oxidation process is developed for fabricating high quality VO_2 and the resulting thin films undergo comprehensive material and optical characterizations. The corresponding measurement platform is developed to measure the temperature-dependent transmittance and reflectance of the fabricated Fabry-Perot samples. The variable heat rejection of the fabricated samples is demonstrated via bell jar and cryothermal vacuum calorimetry measurements. Thermal modeling of a spacecraft equipped with variable emittance radiators is also conducted to elucidate the requirements and the impact for thermochromic variable emittance technology.

The potential of VO_2 to be used as an optical force modulating device is also investigated for spacecraft micropropulsion. The preliminary design considers a Fabry-

Perot cavity with an anti-reflection coating which switches between an absorptive "off" state (for insulating VO_2) and a reflective "on" state (for metallic VO_2), thereby modulating the incident solar radiation pressure. The visible and near-infrared optical properties of the fabricated vanadium dioxide are examined to determine if there is a sufficient optical property shift in those regimes for a tunable device.

ACKNOWLEDGEMENTS

TABLE OF CONTENTS

LIST OF TABLES

LIST OF FIGURES

CHAPTER 1 INTRODUCTION

1.1 Variable Emitters for Dynamic Thermal Management

As space exploration goals grow more advanced, there is a critical need for variable heat rejection technologies to enable a diverse assortment of missions. The international space station and human spaceflight vehicles currently in development rely on dual loop thermal control architecture to take advantage of desirable transport properties for the external loop, while avoiding toxic fluids for the internal cabin loop [1]. Variable heat rejection radiators could potentially eliminate the need for dual fluid loop thermal control by preventing the freezing of transport fluids in the radiator during cold phase operation. Similarly, variable radiators could potentially see use in robotic missions as a means to reduce or eliminate the need for survival heaters [2]. To this end, several technologies to achieve variable heat rejection have been developed, including louvers [3], origami surfaces [4], shape morphing radiators [5], electrochromic radiators [6], [7], and electrostatic radiators [2]. Thermochromic coatings are an economical solution for spacecraft thermal control because, unlike the previously mentioned variable heat rejection strategies, they require no moving parts, no electrical input, and typically add a negligible amount of mass [8]. When the radiator temperature is high, the thermochromic coating will have high infrared emittance to promote the radiative cooling effect. On the other hand, when the radiator temperature is low, the thermochromic coating will have low infrared emittance to minimize radiative loss. This temperature-dependent behavior would permit the spacecraft to passively respond to changes in internal heat load or spacecraft thermal environment.

1

Thermochromic coatings are also desirable for dynamic building thermal management. On average the U.S. Department of Energy estimates that 10% of the total energy consumed nationwide in buildings is used for cooling, and 37% is used for heating [9]. The energy used to cool buildings can be significantly reduced by applying coatings to the exterior surfaces which have high emittance in the infrared spectrum, thereby promoting radiative cooling. Conversely, in cold environments, low infrared emittance is desired to reduce the thermal emission loss and minimize the required building heating. To achieve sub-ambient radiative cooling, the coating should emit selectively in the atmospheric window (8-13 µm), where the atmosphere is transparent and the surface can radiate to outer space. Photonic crystal structures have been used extensively to achieve spectrally selective radiative coatings for both static radiative cooling [10]–[14] and thermophotovoltaic applications (TPV) [15]–[17]. Selective absorption/emission can also be achieved with Fabry-Perot resonance cavities [18], [19], multilayers [20], nanoparticles [21] and metamaterials [22]–[24]. The coatings presented in the aforementioned studies are not designed to have temperature-dependent emittance and the corresponding variable heat rejection. A tunable radiative coating with variable emittance could help to reduce energy consumption in buildings by limiting heat loss in cold weather with low emittance or promoting heat dissipation in warm weather by selectively emitting heat within the 8 to 13 µm atmospheric window to outer space.

One passive way to achieve variable heat rejection is through thermochromic materials that change their optical properties based on temperature [8], [25]. One option is lanthanum strontium manganese oxide (LSMO), which is another well-studied

thermochromic material which transitions from a metal at low temperatures to an insulator at high temperatures [26]. A weakness of LSMO is that it transitions over a very broad temperature range, so the optical property shift over the temperatures of interest is much smaller than that achieved with other thermochromic materials, such as vanadium dioxide (VO_2). The large property shift of VO_2 makes it uniquely promising for thermochromic variable emittance when incorporated into nano-engineered radiative coatings.

1.2 Radiation Pressure Modulation with Tunable Surfaces

Traditionally, solar radiation pressure has been considered as a detrimental force in spacecraft attitude control and micropropulsion; however, this dissertation work seeks to develop radiative coating technology which can take advantage of solar radiation pressure to provide efficient attitude control or micropropulsion for solar sailing and small spacecraft. Solar sail technology development is of interest to many space agencies worldwide due to the ability to use the energy of the incident photons to propel a spacecraft without the need for consumable fuel [27]. By varying the reflectivity of the exterior surface of the spacecraft, the momentum transfer to the spacecraft from the incoming photons can be changed, leading to a modulation in the radiation pressure incident on the surface, which can be used to steer the spacecraft or control the orientation [28]–[31]. The basis for this modulation in radiation pressure is that the photons impinging on a reflective surface will generate twice the momentum transfer as photons impinging on an absorptive surface [32]. Several technologies have been employed to modulate the solar radiation

pressure to achieve small torques capable of attitude control or orbit maintenance, including: reflective vanes [33], shape control [34], [35], actively controlled liquid crystal panels [8], [36], and other electrochromic coatings [37], [38]. Reflective vanes and shape control both require mechanisms and actuators to mechanically change the geometry of the surface that is exposed to solar radiation pressure. This requires increased mass and power in a spacecraft, which are often at a premium, especially on small science missions. Liquid crystals are designed to switch between specular and diffuse transmittance. When combined with a back reflector, the device switches between specular reflectance and diffuse reflectance, which yields a much smaller possible modulation in solar radiation pressure than a switch between absorptance and reflectance, or, ideally, a switch between reflectance and transmittance. Known for its large shift in optical properties upon phase transition, VO_2 may have potential as a tunable material for optical force modulation devices. This dissertation work includes the design and analysis of thermochromic radiation coatings which can selectively vary their reflectance in the visible and near-infrared spectra to deliver solar radiation pressure modulation.

1.3 Tunable Properties of Vanadium Dioxide (VO_2)

VO_2 undergoes a Mott phase transition from a monoclinic insulator to a rutile metal at 68 °C, exhibiting a corresponding shift in optical properties [39]. At temperatures below its transition, VO_2 is a monoclinic insulator, whereas at temperatures above its transition the VO_2 is a rutile metal. This shift can be taken advantage of to design a myriad of thermochromic devices such as smart windows [40]–[48], thermochromic infrared emitters

[49]–[51], and thermal rectifiers [52]–[54]. For example, Zheng et al. [55] designed and deposited a multifunctional $TiO_2/VO_2(M)/TiO_2(A)$ coating that can modulate its near-infrared transmittance for smart window applications, while also providing anti-fogging and self-cleaning functions [55]. Long et al. demonstrated a VO_2-based thermochromic double glazing for smart window applications [43]. Li Voti et al. [56] investigated multilayer VO_2/copper stacks that can provide tunable emissivity in the 3-5 µm atmospheric window which is useful for infrared sensing applications such as IR camera. Rensberg et al. [57] designed and fabricated a metasurface based on spatially selective defect engineering phase transition VO_2 which can act as a tunable emitter and polarizer. Long et al. [58] have fabricated thermally-switchable VO_2 metamaterial infrared absorbers/emitters which have high emittance at low temperatures and low emittance at temperatures above the VO_2 phase transition temperature. Although the metamaterial structure exhibits a substantial change in emittance, the high-to-low emittance change as the temperature increases is not desirable for radiative cooling. In addition to its thermochromic behavior, VO_2 is also electrochromic, meaning that the phase transition can also be induced by applying a small voltage [59].

Given the broad range of applications for which VO_2 can be employed, easy fabrication of high-quality VO_2 thin films is essential for the continued development and advancement of these devices. VO_2 thin films and nanostructures can be prepared using a variety of techniques, however, there exist significant challenges in fabricating stoichiometric VO_2 since vanadium forms many different oxides and is sensitive to the conditions of the preparation method [47]. The most common physical vapor deposition

5

method is DC magnetron sputtering [47], [60]–[63], where pure vanadium or vanadium pentoxide (V_2O_5) is reactively sputtered with an oxygen/argon mixture. This technique requires careful control of the chamber conditions, including substrate temperature, oxygen and argon partial pressures, and power. Typically, VO_2 is either sputtered at high substrate temperatures of 400-600 °C or is sputtered at lower temperatures and then subsequently annealed at 500-600 °C to improve the VO_2 thin film crystallinity [64]–[67]. A significant challenge, and the focus of much research effort, has been reducing the substrate temperature and eliminating the need for high temperature post-deposition annealing while still maintaining quality thermochromism characteristics for the VO_2 thin films.

Recently Gagaoudakis et al. [60] used low-temperature RF sputtering to fabricate VO_2 thin films on commercially available SnO_2-coated glass with a substrate temperature of 300 °C. Chang et al. [68] also fabricated Cr_2O_3/VO_2 bilayer coatings on quartz glass with magnetron sputtering at low temperature between 250 °C and 350 °C. Sun et al. [69] obtained high-quality VO_2 thin films by sputtering at 250 °C without subsequent annealing by depositing on a V_2O_3 interlayer. In addition, Sun et al. [70] deposited single-crystal VO_2 thin films via magnetron sputtering at 300 °C without subsequent annealing by inserting ZnO and TiO_2 layers between the VO_2 thin film and substrate. Other techniques used to deposit VO_2 include atomic layer deposition, which can be done at very low deposition temperatures (<150 °C), but requires a high temperature post-annealing step to achieve desired crystallinity [71]–[73], and pulsed laser deposition, which also generally requires high substrate temperatures [74]–[76]. Several wet chemistry methods are also commonly used to synthesize VO_2 [77]–[79].

Another significant challenge remaining for VO_2-based thermal management devices is a reducing the transition temperature to a range that is acceptable for thermal control applications, generally near 300 K. Impurity doping with metals, particularly tungsten, is a commonly employed technique to reduce the VO_2 temperature [80], [81]. Tungsten doping has been shown to reduce the transition temperature to around room temperature; however, the reduction is accompanied by a proportional decrease in the optical property shift. Another technique investigated to lower the VO_2 transition is defect engineering, where the VO_2 is irradiated by an Ar+ ion beam [57]. This technique can successfully reduce the transition temperature below room temperature, but the optical property shift is significantly decreased. Jiang et al. [66] demonstrated that the oxygen partial pressure during DC sputtering could have a significant role in reducing the VO_2 transition temperature. Liu et al. [67] similarly showed that the partial pressure of the O_2 during the post-anneal could also be used to tune the transition temperature of the VO_2. These two techniques accomplished a much more modest decrease in the transition temperature, but did not have as detrimental an effect on the optical property shift. A major obstacle to the development of VO_2-based variable emittance, where a room temperature transition (or lower) is typically required, is the need to reduce the transition temperature while retaining an acceptable shift in the optical properties.

1.4 Primary Objectives of This Dissertation

For the first topic included in this research, a thermal emitter consisting of a lossless dielectric spacer placed between a VO_2 thin film and an opaque aluminum substrate is

developed with both wavelength-selective and temperature-modulated emittance. To this end, uniaxial expressions for the transfer matrix method and Bruggeman effective medium theory are developed and the theoretical performance and physical mechanisms of the proposed structure are explored in Chapter 2. Chapter 3 discusses the fabrication and comprehensive characterization of VO_2 thin films, starting with the development of a new furnace oxidation process for fabricating high quality VO_2 thin films. In Chapter 4, the fabrication process for the Fabry-Perot emitter and the optical characterization is discussed. Calorimetry-based thermal measurements for both room-temperature ambient and space simulated environments are presented in Chapter 4. In Chapter 5 systems-level thermal modeling of a representative human spacecraft is undertaken to reveal the transition temperature requirements for human spacecraft thermal control. In Chapter 6, the potential for VO_2 to be used in optical force applications is discussed. The conclusions and future work are summarized in Chapter 7.

CHAPTER 2 THEORETICAL DESIGN OF A VO₂-BASED VARIABLE EMITTER

2.1 Fabry-Perot (FP) Emitter Structure Design

The proposed variable emittance device consists of an asymmetric Fabry-Perot resonance cavity, formed by a lossless silicon spacer inserted between a VO₂ thin film and an opaque aluminum mirror substrate [82]. When the VO₂ is metallic at temperatures above 345 K, the VO₂ serves as the top mirror completing the Fabry-Perot cavity and the structure provides an absorption enhancement in the mid-infrared wavelength regime around $\lambda = 10$ µm due to the wave interference effect, promoting radiative cooling (Figure 1). On the other hand, when the VO₂ is insulating below 341 K, the Fabry-Perot cavity is not formed and the structure takes on the properties of the substrate, becoming highly reflective.
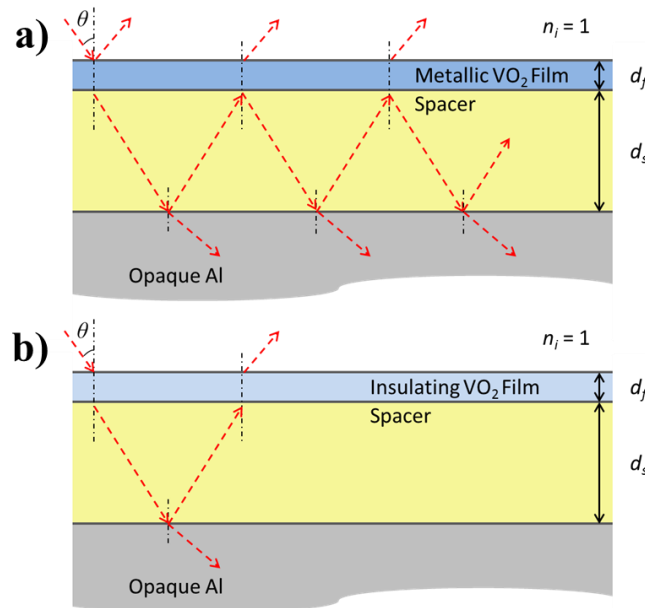
Figure 1. Schematic of the proposed variable emitter and wave propagation when the VO₂ is (a) metallic (T > 345 K) and (b) insulating (T < 341 K). d_f and d_s are the thickness of the VO₂ film and the lossless spacer ($n = 3.4$), respectively.

In addition to simplicity, another advantage of the Fabry-Perot cavity variable emitter design is spectral tunability. The Fabry-Perot resonance wavelength and corresponding emission enhancement can be easily tuned by varying the thickness of the spacer material. A thinner layer will yield a smaller resonance wavelength, while a larger spacer layer will produce a larger resonance wavelength [83]. Similarly, the amplitude and width of the emittance peak can be tuned via the thickness of the VO_2 top thin film mirror. This tunable selectivity is useful particularly for applications like building radiative cooling, where it is ideal to emit only in the atmospheric window (8-13 µm) so that the coating can achieve temperatures well below ambient through radiative cooling to outer space. Additionally, the integration of thermochromic VO_2 into the Fabry-Perot structure allows the coating to either radiatively cool or reduce thermal emission, depending on the temperature.

2.2 Temperature-Dependent Optical Constants of VO₂

VO_2 is an insulator-to-metal transition material that undergoes a Mott phase transition at 341 K and a corresponding dramatic shift in optical properties [39]. Below 341 K, the VO_2 is a uniaxial monoclinic insulator with a dielectric function that can be represented by an ordinary component (ε_O) and an extraordinary component (ε_E). Both the ordinary and extraordinary dielectric components for the insulating VO_2 phase can be described by the Lorentz oscillator model, $\varepsilon_d(\omega) = \varepsilon_\infty + \sum_{j=1}^{N} S_j \omega_j^2 / (\omega_j^2 - i\gamma_j \omega - \omega^2)$, where the values for S_j, ω_j, and γ_j for both components were experimentally determined by Barker

et al. [84]. However, at temperatures above 345 K, the VO_2 becomes a rutile metal whose dielectric function can be calculated via the Drude model $\varepsilon_m = -\omega_p^2 \varepsilon_\infty / (\omega^2 - i\omega\omega_c)$, where the plasma frequency ω_p, collision frequency ω_c, and high frequency dielectric constant ε_∞, can also be found in [84]. Qazilbash et al. [39] demonstrated that the phase change takes place over a range of temperatures, rather than being instantaneous. Therefore, a model must be developed to describe the behavior of the VO_2 within this transition temperature regime. Below 341 K the VO_2 is insulating, however as the temperature rises in the transition range, metallic inclusions form in the insulating host, creating an inhomogeneous composite medium. The Bruggeman effective medium theory (EMT) [85] is introduced to obtain the effective dielectric constant $\varepsilon_{eff}(\lambda)$ of the VO_2 during the phase transition:

$$f \frac{\varepsilon_m - \varepsilon_{eff}}{\varepsilon_{eff} + q(\varepsilon_m - \varepsilon_{eff})} + (1-f) \frac{\varepsilon_d - \varepsilon_{eff}}{\varepsilon_{eff} + q(\varepsilon_d - \varepsilon_{eff})} = 0 \tag{1}$$

where each term represents the depolarization field of a constituent material. The dielectric constant of the metallic inclusions, $\varepsilon_m(\lambda)$, is approximated by the dielectric constant of the rutile metal at 345 K. Likewise, the dielectric constant of the insulating material is assumed to be equal to the dielectric constant of the insulating VO_2 at 341 K. f is the volume fraction of the metallic puddles, which gets larger as the temperature increases during the phase transition. The depolarization factor q is determined by the shape of the inclusion. Both the volume fraction and the depolarization factor have been tabulated in [39] as a function of temperature. As Eq. (1) has two solutions, the one with a positive value for the imaginary part should be selected as the correct dielectric function for the effective medium.

Since Barker et al. [84] reported uniaxial dielectric behavior for the insulating VO_2, the effective medium is also assumed to be uniaxial, where ε_O and ε_E are substituted into Eq. (1) as ε_i to get the ordinary component ($\varepsilon_{eff,O}$) and the extraordinary component ($\varepsilon_{eff,E}$) respectively. Note that the f obtained from [28] is used for both components, while the q obtained from [28] is only applied to the ordinary case, i.e. q_O. A depolarization factor of $q_E = (1-2q_O)$ is used to calculate $\varepsilon_{eff,E}$ by considering that the sum of the depolarization factors must equal one. Table 1 summarizes the depolarization factors and volume fractions used to calculate the effective dielectric constant of the VO_2 during phase transition from [39].

Table 1. Ordinary depolarization factor q_O, extraordinary depolarization factor q_E, and volume fraction f for selected temperatures used to compute the optical constants of VO_2 in phase transition.

T (K)	q_O	$q_E = 1-2q_O$	f
342	0.2	0.6	0.18
342.6	0.33	0.34	0.31
343	0.45	0.1	0.48
343.6	0.5	0	0.7

The transition of the real and imaginary parts of both dielectric constants, $\varepsilon_{eff,O}$ and $\varepsilon_{eff,E}$, is depicted in Figure 2 for selected temperatures. The pole behavior at wavelengths between 17 and 20 µm in Figure 2(a), along with the corresponding peaks at 17 and 20 µm in Figure 2(b), indicates epsilon-near-pole (ENP) modes in the ordinary dielectric constant [86]. These modes are characteristic of the Lorentz model used to predict the insulating VO_2 optical properties and will lead to absorption enhancements in the proposed multilayer

12

structure [86], [87]. The dramatic shift in optical properties, as evidenced in Figure 2, is the basis for the variable emittance sought for dynamic radiative cooling.
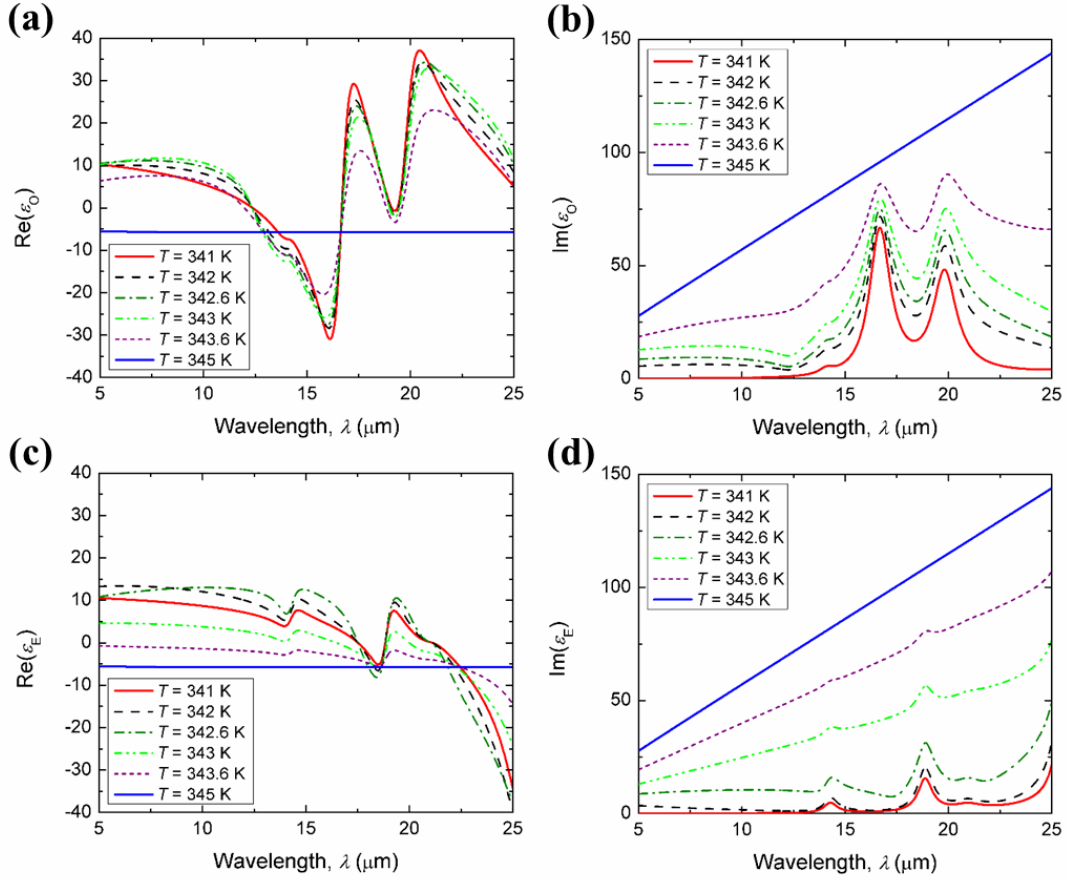
Figure 2. Evolution of the (a) real and (b) imaginary portions of the ordinary VO$_2$ dielectric constant during phase transition. Phonon modes for insulating VO$_2$ are seen at 17 and 20 µm. The (c) real and (d) imaginary portion of the extraordinary VO$_2$ dielectric function also show a dramatic shift as the temperature is increased through the transition temperature regime.

2.3 Uniaxial Transfer Matrix Method

While the goal of this research is to demonstrate the emissive ability of the proposed multilayer structure, direct calculation of emittance can be computationally intensive, especially for structures with many layers. In the interest of providing a generalized methodology, the emittance is calculated via the indirect method presented by Wang et al. [88], which can easily model structures with multiple layers. Here, the method is extended to account for uniaxial layers at thermal equilibrium. To model the absorption of the proposed emitter, the spectral directional transmittance and spectral directional reflectance are first calculated using the matrix formulation of thin film optics. The electric field of the wave in each layer can be described in terms of forward and backward waves, where A and B are the amplitudes of the forward and backward waves respectively. If the magnetic field H is obtained from Maxwell's equations, then the z-component of the Poynting vector can be calculated. By applying the interface boundary conditions at each layer, the relationship between the backward and forward waves in the incident medium and the substrate is:

$$\begin{pmatrix} A_1 \\ B_1 \end{pmatrix} = M \begin{pmatrix} A_N \\ B_N \end{pmatrix} \tag{2}$$

where $M = \prod_{l=1}^{N-1} P_l D_l^{-1} D_{l+1}$. The expressions for the dynamical matrix, D_j, and the propagation matrix, P_j, are listed below for both s- and p-polarized waves:

$$P_j^s = \begin{pmatrix} e^{-ik_z^s d_j} & 0 \\ 0 & e^{-ik_z^s d_j} \end{pmatrix} \tag{3}$$

$$P_j^p = \begin{pmatrix} e^{-ik_z^p d_j} & 0 \\ 0 & e^{-ik_z^p d_j} \end{pmatrix} \tag{4}$$

14

$$D_j^s = \begin{pmatrix} 1 & 1 \\ \dfrac{k_j^s}{\mu_{jO}} & -\dfrac{k_j^s}{\mu_{jO}} \end{pmatrix} \tag{5}$$

$$D_j^p = \begin{pmatrix} 1 & 1 \\ \dfrac{k_j^p}{\varepsilon_{jO}} & -\dfrac{k_j^p}{\varepsilon_{jO}} \end{pmatrix} \tag{6}$$

where d_j is the layer thickness of layer j. ε_O and μ_O are the ordinary dielectric function and magnetic permeability respectively. The uniaxial z-direction wavevectors, k_j^s and k_j^p, are [89]:

$$k_j^s = \sqrt{k_0^2 \varepsilon_{iO} \mu_{iO} - \mu_{iO} k_x^2 / \mu_{iE}} \tag{7}$$

$$k_j^p = \sqrt{k_0^2 \varepsilon_{iO} \mu_{iO} - \varepsilon_{iO} k_x^2 / \varepsilon_{iE}} \tag{8}$$

By considering that there is no backward wave in the substrate ($B_N = 0$), the reflection and transmittance coefficients can be calculated from:

$$R_\lambda^{'} = rr^* = \left| \frac{M_{21}}{M_{11}} \right|^2 \tag{9}$$

$$T_\lambda^{',s} = \frac{\mathrm{Re}(k_{z,N}^s / \mu_{N,O})}{\mathrm{Re}(k_{z,1}^s / \mu_{1,O})} \left| \frac{1}{M_{11}} \right|^2 \tag{10}$$

$$T_\lambda^{',p} = \frac{\mathrm{Re}(k_{z,N}^p / \varepsilon_{N,O})}{\mathrm{Re}(k_{z,1}^p / \varepsilon_{1,O})} \left| \frac{1}{M_{11}} \right|^2 \tag{11}$$

where $k_0 = \omega/c_0$ and $k_x = k_0 \sin\theta_i$. Note that in the proposed structure with the Al substrate in Fig. 1, $T_\lambda^{'}$ represents the energy transmitted into, or basically absorbed by, the substrate.

As the Al substrate is opaque, the spectral-directional emittance is determined indirectly through the energy balance and Kirchhoff's law:

$$\varepsilon_\lambda^{'} = \alpha_\lambda^{'} = 1 - R_\lambda^{'} \tag{12}$$

It is important to note that this relation is applied by assuming that the layers are all at the same temperature. For this study, the incident medium was assumed to be vacuum. This method can be used to determine the radiative properties of a multilayer structure composed of isotropic and uniaxial layers, including layers with nanostructures such as nanoparticles and nanowires whose composite dielectric function can be approximated by an effective medium theory.

2.4 Radiative Properties and Performance of the Proposed FP Structure

The aluminum substrate in this study is modeled as 200 nm, causing the structure to be opaque. The spacer thickness (d_c) used in these calculations is 730 nm, which is approximately the thickness where Fabry-Perot resonance occurs at $\lambda = 10$ µm for metallic VO$_2$. The required spacer thickness to achieve Fabry-Perot resonance at the target wavelength can be predicted by $t = m\lambda_{res} / 4n_c$, where m is an odd integer [83]. The 25 nm VO$_2$ thickness (d_f) was iteratively determined to produce an emittance peak of unity at $\lambda = 10$ µm. The optical properties for aluminum were calculated from the Drude model, using the constants presented in Ref. [90]. The dielectric layer is modeled as an arbitrary material with refractive index n and an extinction coefficient of $k = 0$. The dielectric constant is then calculated from $\varepsilon = (n + ik)^2$. A negligibly small extinction coefficient is consistent with

the typical properties of dielectric materials such as undoped silicon or magnesium fluoride in the infrared spectrum. The refractive index is chosen to be $n = 3.4$ here, which is the case for intrinsic silicon in the mid-infrared [91], [92].

A well-performing dynamic thermal emitter is defined by low absorptance when the VO_2 is insulating and high broadband absorption around a wavelength of 10 µm when the VO_2 is metallic. In Figure 3, the spectral normal emittance is modeled as a function of wavelength for the proposed structure when the VO_2 is in its metallic and insulating phases. Intermediate temperatures are also plotted to show the development of the spectral emittance during phase transition. Overall, the insulating case has the desired low emittance (<10%), however there are some peaks at $\lambda = 10, 13, 17$, and 20 µm where the absorption is enhanced. Since insulating VO_2 is modeled as a Lorentz oscillator, the absorption peaks near $\lambda = 13$, 17, and 20 µm are related to the ENP enhancement identified in Section 2.2. The peak at $\lambda = 10$ µm in both the metallic and insulating case is due to Fabry-Perot resonance. This structure holds promise as a switchable thermal emitter because the difference in emittance between the insulating and metallic layers is large. Note that the metallic emittance is nearly ten times the insulating emittance at $\lambda = 10$ µm.
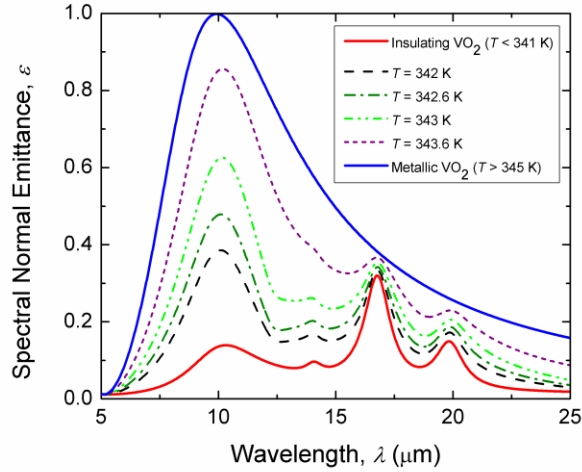
Figure 3. Spectral normal emittance for the proposed structure. When the VO$_2$ is metallic, the coating has high broadband emissivity around 10 µm. Apart from VO$_2$ phonon modes, the coating has high reflectivity when VO$_2$ is dielectric.

A possible limitation of 1D multilayer emitters based on the wave interference effect is that the performance is sometimes sensitive to incidence angle [93]. Since the emitter would be deployed as part of a thermal management system for a building or spacecraft, its performance at nonzero incidence angles is also important. Figure 4 models the emittance of the proposed structure as a function of incident wavelength and angle, for both the insulating and metallic phases. When VO$_2$ is metallic, the emittance peak is calculated to be broadband and high for all but the largest angles for both polarizations. The broadband emittance peak is a result of the optical properties of the VO$_2$, which is a poor reflector compared to noble metals such as silver or gold, leading to a broader emission peak. A similar phenomenon is demonstrated with tungsten in the solar spectrum by Fang et al. [94]. Low emittance is seen for almost all wavelengths and angles for the

18

insulating phase. As discussed previously, the areas of higher narrowband emittance near $\lambda = 17$ and $20\,\mu m$ are caused by ENP modes intrinsic to insulating VO_2. The area of higher emittance at 10 µm wavelength in the insulating case is caused by weak Fabry-Perot resonance.
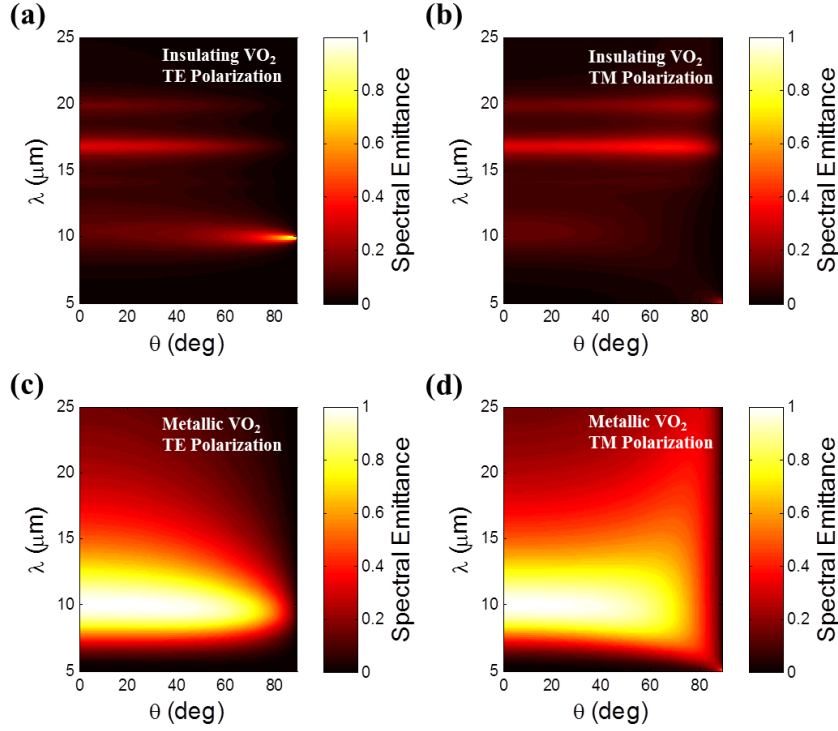
Figure 4. The uniaxial transfer matrix method is used to calculate the angle dependence of the spectral emissivity for (a) TE waves in the metallic case, (b) TM waves in the metallic case, (c) TE waves in the insulating case, and (d) TM waves in the insulating case.

To verify that the high emittance observed around $\lambda = 10$ µm is caused by Fabry-Perot resonance, the normalized total phase shift inside the cavity and the angle dependent resonance wavelength are plotted in Figure 5. The total phase shift is calculated from:

$$2\Psi = 2\beta + \varphi_b + \varphi_s \tag{13}$$

19

where $\beta = 2\pi n_s d_s \cos\theta_c/\lambda$ is the phase shift traveling in the cavity. φ_b and φ_s are the phase angle of the reflection coefficients at the top and bottom interfaces of the cavity respectively. Fabry-Perot resonance occurs when the total phase shift inside the cavity is in integer multiples of 2π, leading to standing waves inside the cavity. Figure 5(a) shows how the total phase shift varies as a function of wavelength for both the metallic and insulating VO_2 cases for normal incidence. The curves cross 0 at $\lambda = 10\,\mu m$, indicating that there is a Fabry-Perot absorption enhancement at approximately 10 µm for both the insulating and the metallic scenarios. In the high temperature case, the top mirror is the metallic VO_2. In the insulating VO_2 case, the interface between the VO_2 thin film and the air is weakly reflective due to the difference in refractive indices between the incident medium (vacuum, $n = 1$) and the dielectric layers ($n \sim 2.5$-3 for VO_2 and $n = 3.4$ for the dielectric spacer considered). An identical spectral normal emission profile can be produced by considering just 730-nm-thick silicon on aluminum, a structure that Kats et al. discussed which also produced Fabry-Perot resonance [83]. The added thickness of the VO_2 layer in addition to the spacer thickness explains why the insulating resonance condition occurs slightly to the right of the metallic resonance condition.

In Figure 5(b), the interfacial spectral reflectance between the spacer material and the VO_2 thin film is shown as a function of wavelength. The strength of the Fabry-Perot absorption is determined by the thickness and optical properties of the thin film mirror. For insulating VO_2, the interface reflectance is low, except for the 15-20 µm spectral range, where the insulating VO_2 behaves like a metal due to the ENP modes characteristic of the Lorentz model used to predict the optical properties of insulating VO_2. The lower

reflectance of the spacer/VO$_2$ interface results in a weaker Fabry-Perot resonance response. The comparatively higher reflectance of the spacer/metallic VO$_2$ interface leads to a stronger Fabry-Perot absorption at the resonance wavelength.
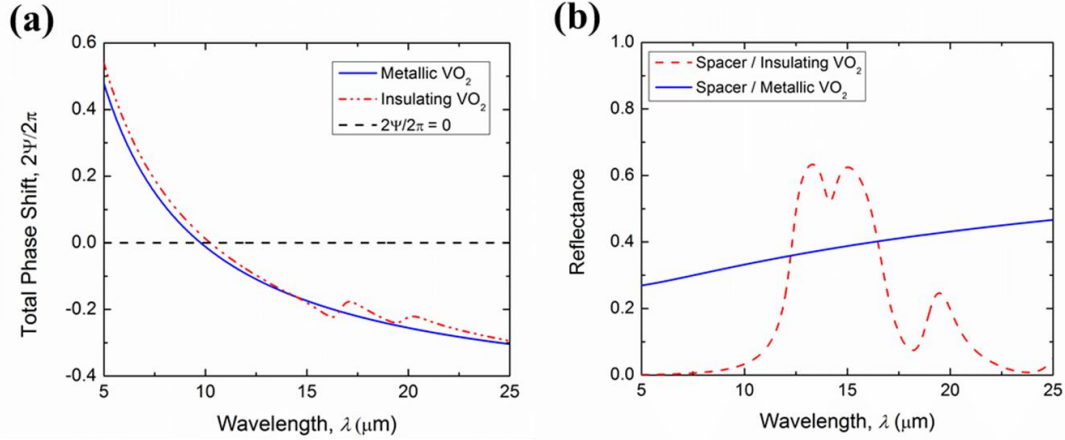
Figure 5. The (a) resonance condition is fulfilled for both the insulating and metallic phases of VO$_2$ at approximately $\lambda = 10$ μm, where the total phase shift in the cavity is equal to an integer multiple of $2\pi m$. (b) The interfacial reflectance between the cavity material and the VO$_2$ is higher when VO$_2$ is metallic over most of the wavelength range considered.

To further elucidate the physical mechanisms behind the dynamic radiative properties of the proposed structure, the layer absorptions for both insulating and metallic VO$_2$ have been plotted in Figure 6. The spectral normal absorptance in the aluminum substrate can be obtained as $\alpha_s = T'_\lambda$. As the lossless spacer does not contribute to the total absorption of the multilayer structure, the total structure absorption can be considered as $\alpha_f + \alpha_s = \alpha'_\lambda$. Therefore, the spectral normal absorptance in the thin film VO$_2$ layer is $\alpha_f = \alpha'_\lambda - \alpha_s = 1 - R'_\lambda - T'_\lambda$. When VO$_2$ is metallic (Figure 6a), most of the absorption occurs in the VO$_2$ thin film layer since VO$_2$ is absorbing. When VO$_2$ is insulating (Figure 6b), the

absorption due to Fabry-Perot resonance occurs primarily in the aluminum substrate since the insulating VO_2 thin film is semi-transparent. At wavelengths between 15 and 20 µm, the VO_2 ENP modes lead to several weak absorption peaks. The difference in the optical properties of VO_2 allows the structure to dynamically switch between radiative cooling at high temperatures and minimizing thermal loss at low temperatures.
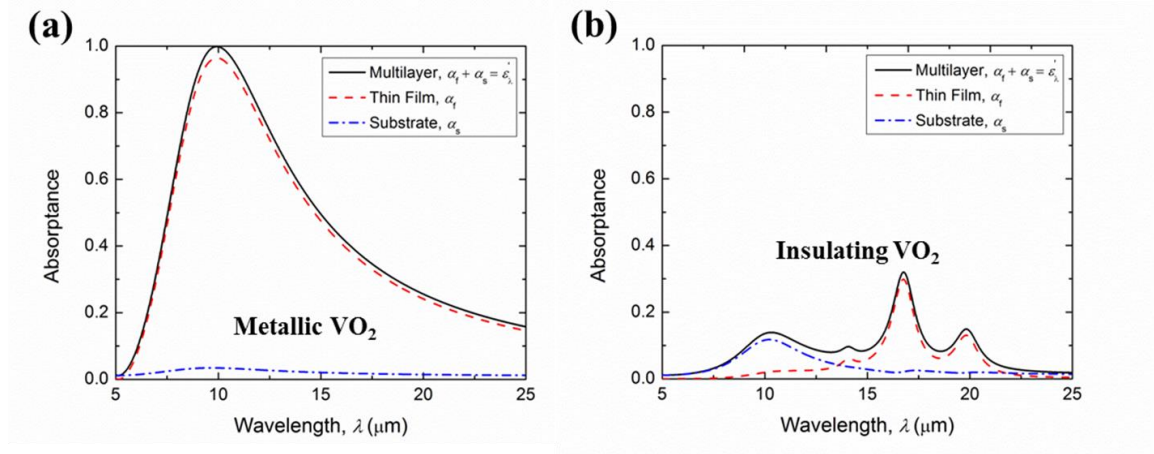
Figure 6. When VO_2 is (a) metallic, absorption occurs primarily in the VO_2 thin film layer. When VO_2 is (b) insulating, most of the Fabry-Perot absorption occurs in the aluminum substrate layer. The ENP modes for insulating VO_2 lead to high absorption in the thin film VO_2 layer between 15 and 20 µm.

The total normal emittance can be determined from [32].

$$\varepsilon_N = \frac{1}{\sigma T^4} \int_{0.3\mu m}^{40\mu m} \varepsilon_\lambda'(T,\lambda,\theta = 0) E_{b\lambda}(T,\lambda) d\lambda \tag{14}$$

where $E_{b\lambda}$ is the spectral blackbody emissive power and σ is the Stefan-Boltzmann constant. Likewise, the total hemispherical emittance can be calculated via [32]:

$$\varepsilon = \frac{2}{\sigma T^4} \int_{0.3\,\mu m}^{40\,\mu m} E_{b\lambda}(T,\lambda) \int_0^{\pi/2} \varepsilon_{\lambda}^{'}(T,\lambda,\theta) \cos\theta \sin\theta \, d\theta \, d\lambda \tag{15}$$

where $\varepsilon_{\lambda}^{'}(T,\lambda,\theta)$ is the spectral directional emissivity with an emission angle of θ. As shown in Figure 7(a), the coating achieves a total normal emittance variation of 0.41 from 0.08 to 0.49 (red dashed line) and a total hemispherical emittance variation of 0.38 from 0.07 to 0.45 over the course of the phase transition (blue solid line).

The total hemispherical emissive power, which represents the dynamic cooling power that could be achieved for extraterrestrial applications such as satellites and other spacecraft, can be calculated via [32]:

$$q_{\text{rad,extraterr}} = \varepsilon \sigma T^4 \tag{16}$$

As presented in Figure 7(b), the temperature-dependent total hemispherical emissive power (blue solid line) achieves a 6.5 fold enhancement or an increase of 309 W/m^2 from 56 W/m^2 at 341 K to 365 W/m^2 at 345 K.

The tunable emissive power also makes the proposed coating a good candidate for applications in building cooling, where spectral selectivity in thermal emission is needed to dissipate the energy through the atmospheric window into outer space. When considering the cooling power for buildings and other terrestrial systems, the effect of radiation from the atmosphere must be considered. In the terrestrial case without considering solar heating and convective heat transfer, the net radiative cooling power of

23

the coating ($q_{rad,terr}$) can be taken as the difference between the power radiated by the sample, and the power absorbed by the sample from the atmosphere [11], [22]:

$$q_{rad,terr} = q_{rad,extraterr} - q_{atm} \qquad (17)$$

where the emissive power absorbed from the atmosphere q_{atm} can be calculated from:

$$q_{atm} = 2 \int_{0.3\mu m}^{40\mu m} E_{b\lambda}(T_{atm},\lambda) \int_{0}^{\pi/2} \varepsilon_{atm}(T_{atm},\lambda,\theta)\varepsilon_{\lambda}^{'}(T,\lambda,\theta)\cos\theta\sin\theta\,d\theta\,d\lambda \qquad (18)$$

The atmospheric emittance ε_{atm} is given by $\varepsilon_{atm}(\lambda,\theta) = 1 - t(\lambda)^{1/\cos\theta}$, where t is the AM1.5 transmittance spectra of the atmosphere in the zenith direction [11], [41], [95]. T_{atm} is the atmospheric temperature, which is taken to be 300 K. The net emissive power $q_{rad,terr}$ through the atmospheric window is shown in Figure 7(b) as a function of the coating temperature (red dashed line). The emissive power increases from 38 W/m^2 at the onset of the VO$_2$ phase transition (i.e., 341 K) to 281 W/m^2 at the end of the phase transition (i.e., 345 K), resulting in 7.3 fold enhancement in cooling power and an increase of 242 W/m^2. Since a significant portion of the total hemispherical emissive power is radiated within the atmospheric window, this structure shows good potential as a dynamic radiative coating for building cooling applications.
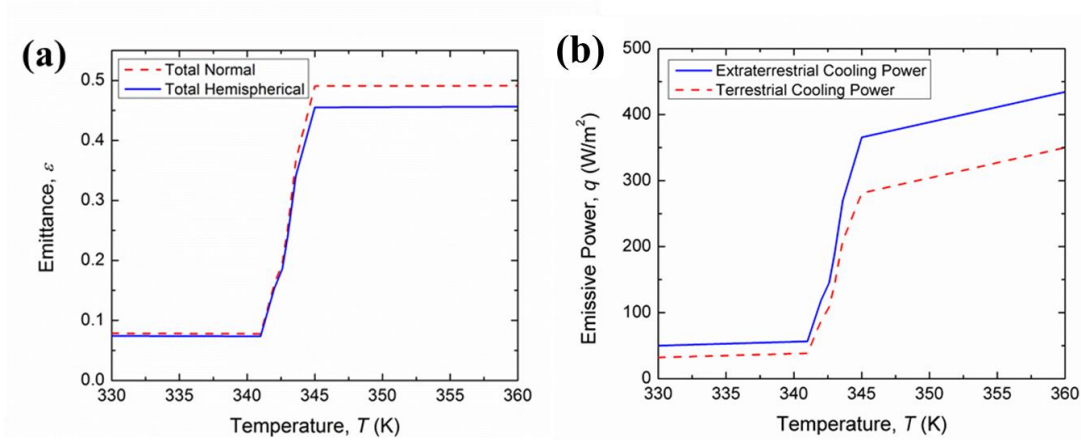
Figure 7. (a) The total hemispherical emissivity achieves a variation of 38% from 341 K to 345 K, while the normal case achieves a 41% variation. (b) The total emissive power (extraterrestrial cooling power) achieves a variation of 309 W/m², while the building cooling power (terrestrial cooling power) achieves a variation of 242 W/m².

Using a combination of uniaxial wave propagation theory, Bruggeman EMT, and an indirect calculation of emissivity, a dynamic VO_2-based Fabry-Perot emitter had been designed, the physical mechanisms have been elucidated, and the temperature-dependent performance has been predicted. The difference in the emittance as the VO_2 changes from an insulator to metal suggests that this type of emitter could be beneficial for applications in spacecraft and building thermal control. The next chapter will discuss the fabrication of the thermochromic VO_2 thin films that are critical to deliver the desired variable emittance.

CHAPTER 3 FABRICATION AND INFRARED SPECTROMETRIC

CHARACTERIZATION OF VANADIUM DIOXIDE THIN FILMS

To fabricate the proposed Fabry-Perot emitter, first a repeatable and effective method for fabricating high quality VO_2 thin films had to be developed. The development of a low-temperature method based on electron beam evaporation and subsequent annealing in an oxygen environment is described in this chapter, along with the characterization of the fabricated VO_2 thin films. The composition and morphology of the films are characterized using x-ray diffraction (XRD), Raman spectroscopy, and atomic force microscopy (AFM). The optical performance of the prepared films is demonstrated using temperature-dependent Fourier transform infrared (FTIR) spectroscopy measurements. The insulating and metallic VO_2 dielectric constants for films prepared through this method are fitted. The heating and cooling curves are measured to demonstrate the transition temperatures and hysteresis characteristics of the prepared VO_2 films. The filling fraction is also determined to provide a convenient means to model the VO_2 properties in phase transition.

First, the refractive index, n, and the extinction coefficient, κ, of the silicon substrate are determined to aid in the VO_2 property fitting process. Then a 30 nm vanadium thin film is deposited on the silicon substrate using electron beam evaporation. Afterwards RMS roughness and thickness are measured to complete the materials characterization for the vanadium thin film. Then the film is oxidized to form the VO_2 thin film. Similarly, the surface roughness and thickness of the prepared VO_2 are measured, as well as the

composition via XRD patterns and Raman spectra. The flow chart for the fabrication and characterization process is shown in Figure 8 as a guide.
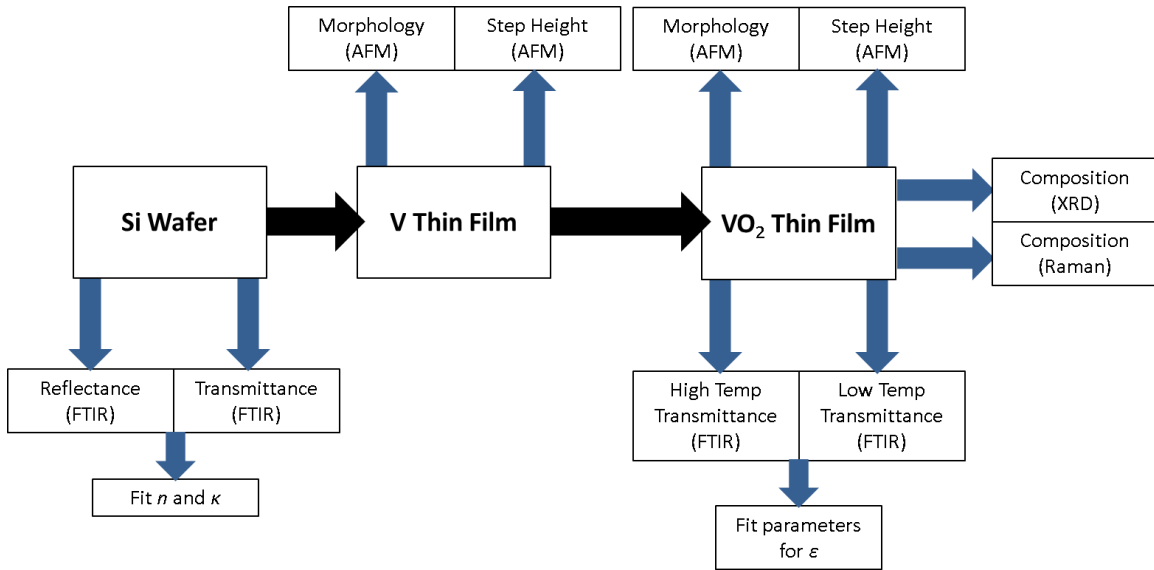
Figure 8. Flow chart describing the procedure for the fabrication, material characterizations, and optical characterizations.

3.1 Furnace Oxidation Fabrication Process

Each sample was fabricated on a double-side-polished 385-μm-thick lightly-doped silicon wafer substrate ($10<\rho<25$ Ω-cm, <100> orientation, Virginia Semiconductor Inc.) that measures approximately 1 cm × 2 cm in size. Lightly doped silicon substrates were chosen intentionally to achieve high transparency across the near-infrared and mid-infrared wavelengths of interest ($\lambda = 2.5$ μm to $\lambda = 20$ μm). Prior to the deposition of thin film vanadium, the silicon substrates were cleaned with isopropyl alcohol and blow dried using nitrogen gas. 30 nm vanadium thin films were deposited on the silicon substrates from vanadium pellets (99.99% purity, Kurt J. Lesker Co) via electron beam evaporation (Lesker

PVD75 Electron Beam Evaporator). The base pressure of the chamber and deposition rate were kept at 3×10^{-6} Torr and 0.7 Å/s, respectively, during the deposition process.

Subsequently, the samples were oxidized in a Thermco Minibrute ambient pressure tube furnace to induce the V to VO_2 transformation. Figure 9 shows the configuration for the Minibrute tube furnace. The samples are first loaded onto a quartz boat and allowed to heat in the hot zone of the furnace for 10 mins while the quartz tube is purged with nitrogen at a 60 SLPM flow rate. After reaching 300 °C, 0.5 SLPM pure O_2 was mixed with the 60 SLPM N_2 gas to oxidize the surface. After the oxidization process, the sample is immediately transferred to the cold end of the tube furnace and is allowed to reach to room temperature for 10 minutes under a nitrogen purge.
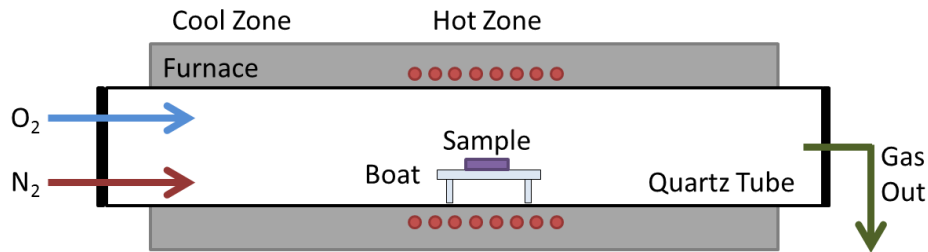
Figure 9. Schematic of the Thermco Minibrute atmospheric tube furnace and the vanadium thin film annealing process.

This dissertation work includes a parametric study to determine the required furnace conditions for high quality VO_2 thin films. First, an initial parametric study was conducted to determine the best temperature and gas flow rate for the oxidation (Table 2). From Figure 10(a), it is apparent that the furnace conditions have a drastic effect on the vanadium oxide composition. Samples 1 and 2, which were oxidized at 300 °C, exhibited a significant change in transmittance upon phase transition. On the other hand, Samples 3

and 4, which were oxidized at 400 °C showed no evidence of a temperature-dependent phase transition, indicating that these films are not thermochromic VO_2. The films were later determined to be V_2O_5 via x-ray diffraction.

Table 2. Sample conditions for the initial parametric study.

Sample	Time (min.)	O_2 flow (SLPM)	Temperature (°C)	ΔTrans (%)
1	20	1.5	297	9
2	**60**	**0.5**	**303**	**20**
3	15	1.5	399	0
4	60	0.5	403	0

a)

b)
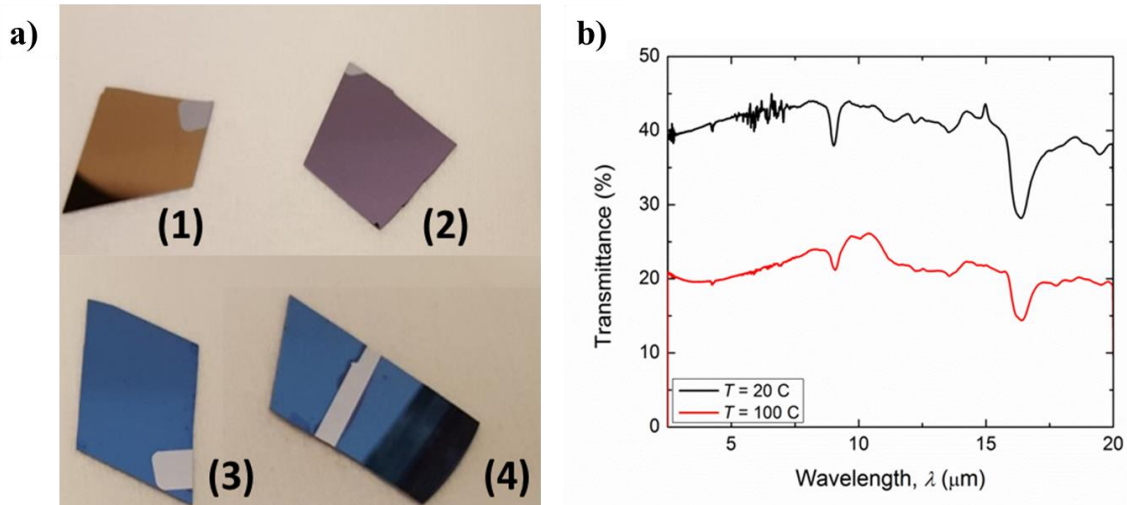
Figure 10. (a) Samples fabricated in the initial parametric study and (b) the temperature-dependent transmittance of Sample 2, which achieved the best transmittance change.

The optimal oxidation temperature, gas flow rates, and time were determined via several parametric studies. Table 3 shows an example parametric study for the oxidation

temperature, where all samples were oxidized for one hour under 0.5 SLPM O_2 and 60 SLPM N_2, while the temperature was varied between 250 °C and 400 °C. It can be seen that an oxidation temperature of $T = 300$ °C results in the largest change in transmittance, while the other temperatures yielded no signs of phase transition upon heating. Similar studies were also undertaken to determine the optimal O_2 flow rate, N_2 flow rate, and oxidation time. Close surface and color inspection shows that the vanadium samples underwent significant chemical transformation as evidenced by a metallic hue (vanadium) to a lilac (VO_2) color change. The optimal VO_2 oxidation temperature was determined to be 300 °C and the optimal O_2 flow rate was found to be 0.5 SLPM. The oxidation time is dependent on the thickness of the VO_2, i.e. a thicker layer will take longer to fully oxidize. A VO_2 sample is considered fully oxidized when the transmittance exceeds 50%, approaching the transmittance of the bare silicon substrate. After the material synthesis step, the samples were structurally characterized through Raman spectroscopy and XRD measurements.

Table 3. Oxidation temperature study

Oxidation Temperature (°C)	$\lambda = 2.5$ μm		$\lambda = 10$ μm	
	Transmittance (T = 20 °C)	Transmittance (T = 100 °C)	Transmittance (T = 20 °C)	Transmittance (T = 100 °C)
200	15.6	15.6	13.6	13.6
250	17.2	17.2	16.7	16.7
300	32.1	20.1	34.6	21.8
350	52.5	52.5	45.5	43.7
400	54.8	54.8	51.5	48.6

3.2 Material and Optical Characterizations

X-ray diffraction (XRD) patterns (PANanalytical X'Pert PRO MRD) were used to identify the crystalline phases of the oxidized films. Figure 11(a) shows the XRD pattern for Sample B, which was oxidized for 2 hour and 15 minutes. The XRD pattern for the pure vanadium precursor film is also shown in Figure 11(a). Since the film is quite thin (55 nm) and VO_2 has weak XRD peaks, a scan step time of 1 second was used to get a sufficiently low noise measurement. Additionally, a zero-background quartz plate was used for the measurement to eliminate diffraction contributions from the aluminum sample holder. The peaks at 27, 37, 42, 56, and 65° are characteristic of VO_2 [77]. Full-width-at-half-maximum (FWHM) values of the XRD peaks were extremely narrow, even though this suggests that single crystal domain is large, the films are polycrystalline in nature. Similarly, Raman spectroscopy (Renishaw InVia spectroscopy system) was used to investigate the composition of the fabricated films as shown in Figure 11(b). A 488 nm laser source with a 100x lens was used for the measurement. The Raman peak at 520 cm^{-1} is characteristic of the silicon (100) wafer that the films were prepared on. The other peaks at 146 cm^{-1}, 194 cm^{-1}, 223 cm^{-1}, 261 cm^{-1}, 303 cm^{-1}, 391 cm^{-1}, 441 cm^{-1}, 614 cm^{-1}, and 826 cm^{-1} are characteristic of VO_2 [96]–[99]. All the Raman peaks exhibited FWHM values smaller than 6 cm^{-1} which demonstrates the highly crystalline nature of these VO_2 films.

In addition to the composition, the morphology of the prepared VO_2 thin films was also investigated using atomic force microscopy. Two 1 µm by 1 µm scans were taken, one of the pure vanadium thin film, and one of Sample B. The pure vanadium thin film thickness was 30 ± 1.5 nm and the oxidized film was 55 ± 1.5 nm. The thickness was

determined by measuring the height of a step that was created on the sample during fabrication. In addition to the thickness, the RMS surface roughness of the films was also measured to be 0.79 nm for the pure vanadium thin film and 4.72 nm for the prepared VO_2 film. Figure 11(c) shows the AFM image for the thin vanadium film. The small, uniform grains are characteristic of a high-quality metal film deposited by physical vapor deposition techniques. Figure 11(d) shows the topology for a vanadium dioxide thin film prepared via the method outlined in Section 3.1. The grain sizes are much larger than the pure vanadium thin film, which is characteristic of metal oxides. An AFM measurement of the steps on Samples A and C confirmed that the thickness of all three samples was consistent (60 ± 1.5 nm for Sample A and 57 ± 1.5 nm for Sample C). For all three samples, the thin film thickness approximately doubled due to the incorporation of oxygen atoms during the furnace oxidation.
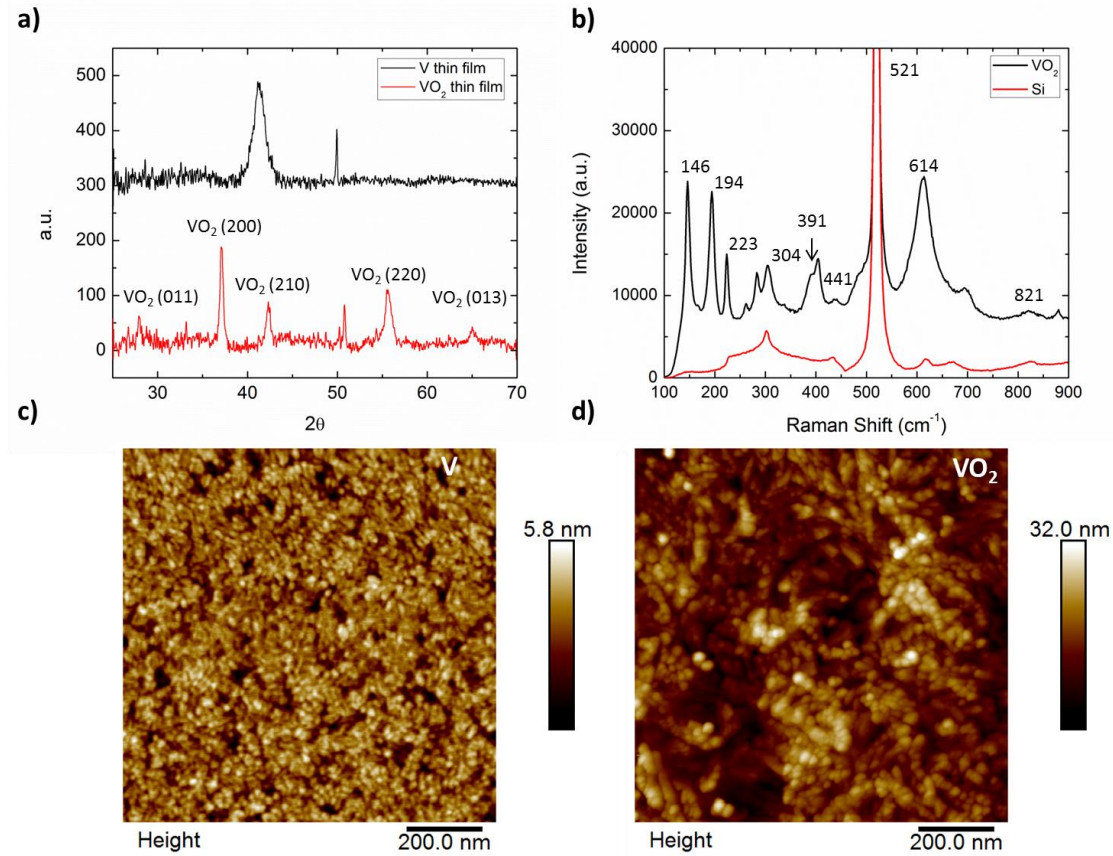
Figure 11. (a) XRD pattern for VO_2 thin film, (b) Raman spectra for the silicon substrate (black) and VO_2 thin film (red), (c) AFM image for the pure vanadium thin film, and (d) AFM image for the VO_2 thin film.

3.3 Dielectric Constant Fitting from Temperature-Dependent Transmittance

The fitting process for the fabricated VO_2 thin films is based on a least-squares fit to optical measurements of the prepared samples. Therefore, accurate optical properties for the silicon substrate first had to be determined. The room temperature refractive index, n, and the extinction coefficient, κ, were extracted from reflectance and transmittance measurements of the bare silicon wafer. The specular near-normal spectral reflectance was

measured with a Harrick variable-angle reflectance accessory for semi-transparent samples in a Nicolet iS50 FTIR spectrometer. The specular normal spectral transmittance was also measured in the Nicolet iS50 spectrometer bench. Both measurements were taken with a resolution of 16 cm^{-1} and averaged over 100 scans. The FTIR spectrometer was purged with nitrogen gas throughout the measurement. Figure 12(a) shows the room temperature reflectance and transmittance measurements used to fit the n and κ of the lightly doped silicon substrate.

An optical model of a silicon wafer is constructed according to ray-tracing theory in order to extract the optical constants of the silicon substrate. In this theory, the reflectance and transmittance can be calculated from Eq. (19) and Eq. (20), respectively [32], [87]:

$$R_{\lambda}' = \rho_{\lambda}' + \frac{\rho_{\lambda}'(1 - \rho_{\lambda}')^2 \tau_{\lambda}'}{1 - \rho_{\lambda}'^2 \tau_{\lambda}'^2} \tag{19}$$

$$T_{\lambda}' = \frac{(1 - \rho_{\lambda}')^2 \tau_{\lambda}'}{1 - \rho_{\lambda}'^2 \tau_{\lambda}'^2} \tag{20}$$

where ρ_{λ}' is the interfacial reflectance between the air and silicon, which can be calculated from Fresnel's equations, and τ_{λ}' is the internal transmittance, which is defined as:

$$\tau_{\lambda}' = exp(-\frac{4\pi\kappa d}{\lambda \cos \theta_2}) \tag{21}$$

where d is the thickness of the wafer, κ is the extinction coefficient of silicon, λ is the wavelength, and θ_2 is the refraction angle inside the slab. Given the experimental reflectance and transmittance data for the silicon substrates, the system consisting of Eqns. (19), (20), and (21) can be solved to extract the two unknown wafer optical properties (n

34

and κ) at a given wavelength. Figure 12(b) shows that the n for the silicon substrate is consistently ~3.42 across the wavelength range considered, which agrees well with the known properties for silicon wafers [91], [92], [100]. The silicon substrate has two phonon modes at 9 µm and 16 µm as shown in Figure 12(c), which are responsible for the dips seen in the transmittance and reflectance measurements at these locations [92], [101]. These extracted optical properties are used in the VO_2 property fitting routine to determine the dielectric constant for the insulating and metallic properties of the prepared VO_2 thin film.
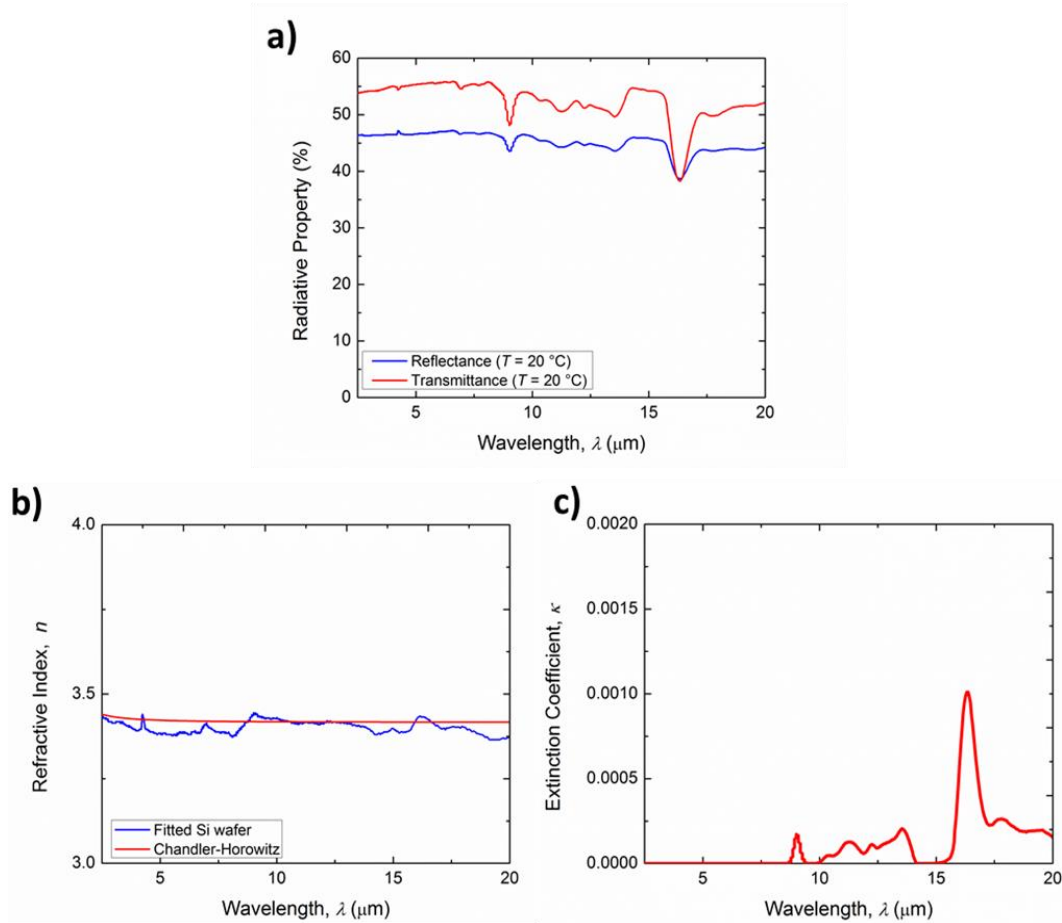
Figure 12. (a) Transmittance (red) and reflectance (blue) for the silicon wafer substrate, (b) fitted refractive index for the silicon wafer (blue) and comparison to literature (red), and (c) extinction coefficient for the silicon wafer.

The specular spectral temperature-dependent transmittance of the three prepared VO_2 thin films was measured in the Nicolet iS50 spectrometer at normal incidence from 2.5 µm to 20 µm with a resolution of 16 cm^{-1}. The measurement was performed in air and was averaged over 32 scans. In addition to being measured at room temperature (insulating VO_2), the samples were also measured at $T = 100$ °C, where the VO_2 has completely transitioned to its metallic phase. Figure 13 shows the temperature-dependent

transmittance for the three VO$_2$ thin films on silicon that were oxidized for one hour and fifteen minutes (Sample B) and two hours (Sample A and C). Sample B shows the best phase transition properties, with a near-infrared transmittance change of 26% and a mid-infrared transmittance change of 17%. Samples A and C achieve similar transmittance changes in both regimes. The dips in reflectance at 9 µm and 16 µm correspond to the silicon phonon modes that can be seen in both the transmittance and reflectance measurements for the silicon substrates, as well as the peaks in the wavelength-dependent extinction coefficient. The peak near 10 µm in the metallic phase is a characteristic of the thin film VO$_2$. The transmittance of all the prepared VO$_2$ samples is comparable to that of the silicon substrate, indicating that the present fabrication method is capable of producing highly transparent VO$_2$ thin films.
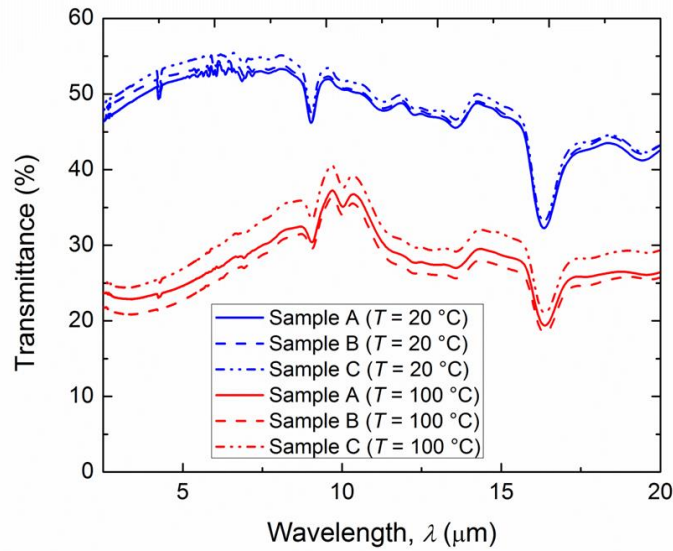
Figure 13. Temperature-dependent transmittance for three samples: Sample A (solid lines), Sample B (dashed lines), and Sample C (dash dotted lines). The blue curves represent the room temperature transmittance and the red curves represent the heated VO$_2$ transmittance at $T = 100$ °C.

The dielectric constant of both the insulating and metallic VO_2 is fitted using a least-squares approach and a genetic algorithm minimization routine. In this method, the sum of the squared residuals between the measurement and the calculated transmittance F based on the optical model is minimized using a genetic algorithm routine [102]:

$$F = \sum_{k=1}^{N} (T_{\text{exp}} - T_{\text{theo}})^2 \tag{22}$$

where T_{exp} is the transmittance measured in the experiment and T_{theo} is the modeled transmittance. T_{theo} is calculated from an expanded version of the ray tracing theory that is used to extract the n and κ for the silicon wafer. The expanded version considers a thin film on top of a thick, incoherent substrate. The expression to model the transmittance of a slab with a thin film on top is [87]:

$$T_{\text{theo}} = \frac{\tau_a \tau_s \tau}{1 - \rho_s \rho_b \tau^2} \tag{23}$$

where τ_a is the transmittance from the air through the top thin film layer, τ_s is the transmittance from the lower interface of the substrate to the air, ρ_s is the substrate reflectance, and ρ_b is the reflectance of the thin film originating from the substrate. Thin film optics can be used to determine τ_a and ρ_b, while τ_s and ρ_s can be determined from Fresnel's equations. All four parameters are calculated from the optical properties of the VO_2 and the silicon wafer.

The optical properties of the insulating VO_2 were fitted to a classical Lorentz oscillator model [84]. The expression used to fit the VO_2 properties is:

$$\varepsilon_d(\omega) = \varepsilon_\infty + \sum_{j=1}^{N} \frac{S_j \omega_j^2}{\omega_j^2 - i\gamma_j\omega - \omega^2} \qquad (24)$$

where ε_∞ is the high frequency dielectric constant, S_j is the phonon strength, ω_j is the phonon frequency, and γ_j is the damping coefficient. The genetic algorithm is used to minimize F according to ε_∞, S_j, ω_j, and γ_j subject to some bounds selected for each parameter. ε_∞ is limited to be between 0 and 30, while S_j and γ_j are limited to be between 0 and 10. The phonon frequency ω_j is bounded between 400 cm^{-1} and 4000 cm^{-1}, which is the measurement range. A four-oscillator model was considered. Figure 14(a) shows the comparison between the calculated transmittance based on the fitted properties and the experimentally determined transmittance. An excellent fit was achieved for the insulating VO_2. The fitted Lorentz oscillator model parameters are summarized in Table 4.

Table 4. Fitting parameters for the dielectric constants of fabricated VO_2 film at the insulating phase in the IR range.

Insulating VO_2 Properties				
E_{inf}	Oscillator index j	S_j	ω_j (cm^{-1})	γ_j
	1	0.561	697	0.080
20	2	2.295	513	0.100
	3	2.084	607	0.100
	4	0.598	826	0.100

The optical properties of the metallic VO_2 were fitted to a dispersion model. The dispersion model is characterized by three terms: the high-frequency dielectric constant, the Drude term which describes the free electron contribution to the dielectric constant,

and the Lorentz term which describes the phonon contributions to the dielectric constant. The expression for the dispersion model used is [103]:

$$\varepsilon_m(\omega) = \varepsilon_\infty - \frac{\omega_n^2}{\omega^2 + i\omega_c\omega} + \sum_{j=1}^{N} \frac{S_j}{1 - \frac{\omega^2}{\omega_j^2 - i\gamma_j\frac{\omega}{\omega_j}}} \tag{25}$$

where ω_n is carrier density parameter and ω_c is the collision frequency. ε_∞, S_j, ω_j, and γ_j are the high frequency dielectric constant, phonon strength, phonon frequency, and damping coefficient, respectively. Four oscillators were also used for the Lorentz term to achieve a satisfactory fit for the metallic VO_2. As with the insulating VO_2 fit, the genetic algorithm is used to minimize F according to ε_∞, ω_n, ω_c, ω_j, S_j, and γ_j subject to some bounds selected for each parameter. ε_∞ is limited to be between -40 and 40, while S_j and γ_j are limited to be between 0 and 10. The phonon frequency ω_j is bounded between 400 cm^{-1} and 4000 cm^{-1}, which represents the measurement range. The comparison between the experimental data and the fitted model is in Figure 14(b). The model parameters for the metallic fit are also summarized in Table 5.

Table 5. Fitting parameters for the dielectric constants of fabricated VO_2 film at the metallic phase in the IR range.

Metallic VO₂ Properties						
E_{inf}	Oscillator index j	S_j	ω_j (cm^{-1})	γ_j	ω_n (cm^{-1})	ω_c (cm^{-1})
-16.7	1	3.563	2357.7	0.429	17620	7816
	2	1.86	591.7	0.101		
	3	3.53E-04	413.7	19.894		
	4	0.658	1858.8	0.158		

The real part of the dielectric function for both the insulating and the metallic VO_2 is shown in Figure 14(c), while the imaginary part is shown in Figure 14(d). It is worthwhile to note that the fabrication process for the VO_2 and the substrate material that the films were deposited on has a significant effect on the optical properties [71]. Therefore, the determination of the optical properties for this fabrication method will assist the development of VO_2-based devices using the fabrication method outlined in this paper.
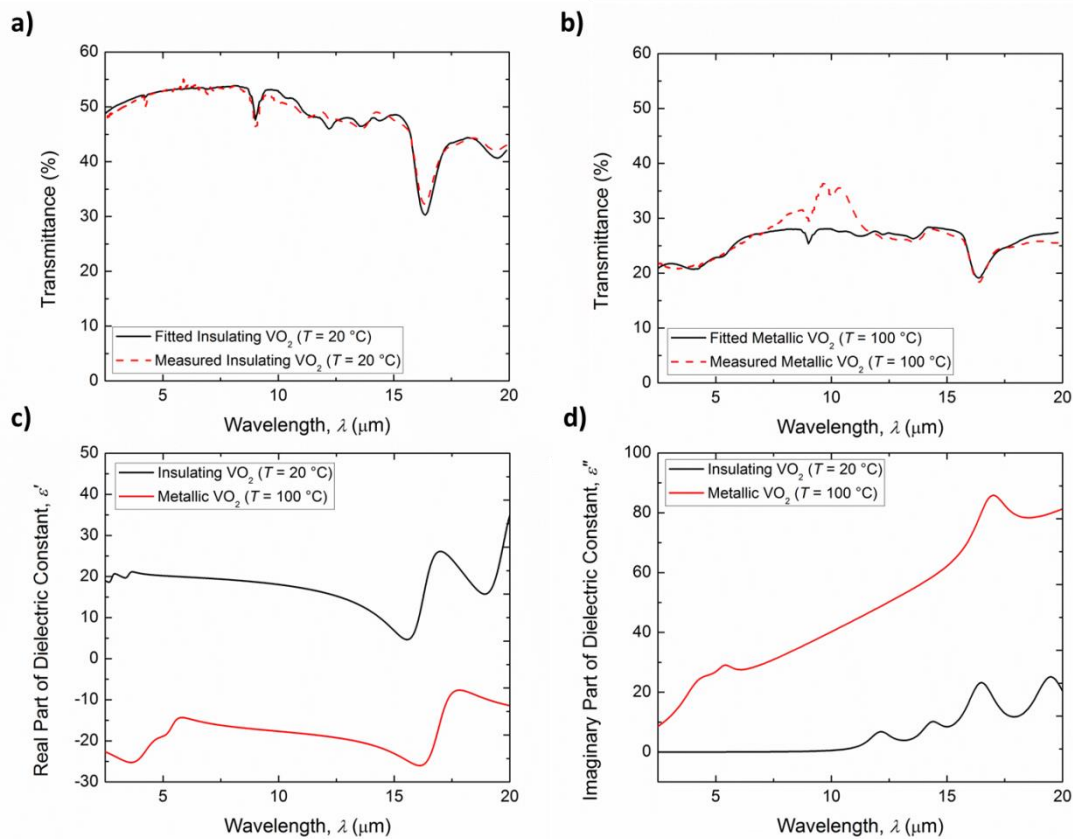
Figure 14. (a) Lorentz oscillator fit for the insulating VO_2, (b) dispersion relation fit for the metallic VO_2, (c) real part of the dielectric function for insulating VO_2 (black) and the metallic VO_2 (red), and (d) imaginary part of the dielectric function for the insulating VO_2 (black) and the metallic VO_2 (red).

3.4   Hysteresis Effect with Heating/Cooling Curves

Besides the optical property shift, the nature of the phase transition and the optical properties within the transition regime is also of interest when designing VO_2 based coatings. Of critical consideration are the transition temperature, width of the transition regime, and the hysteresis between the transition during heating and the transition during cooling. In addition to the insulating and metallic phase properties, many applications also require an understanding of the VO_2 properties in phase transition. To this end, the temperature-dependent properties of the transitioning VO_2 were measured using FTIR spectroscopy in a Janis VPF-800 cryostat, customized with translation and rotation stages, which is mounted in the sample compartment of the Nicolet iS50 spectrometer (Figure 15a). The cryostat enables vacuum measurements of samples with a much more accurate sample temperature measurement. The cryostat is equipped with zinc selenide windows to permit infrared transmittance measurements. The temperature of the sample is controlled with a Lakeshore 335 cryogenic temperature controller. After each set-point on the heating and cooling curves was reached, 10 minutes were allotted for the sample temperature to stabilize at the set-point. The FTIR settings for these measurements are the same as for the measurements mentioned earlier. The transmittance spectra were taken incrementally as Sample B was heated from room temperature to 97 °C, providing the measurement for the heating curve. Similarly, the sample was allowed to cool from 97 °C to room temperature, resulting in the sample's cooling curve measurement. During the measurement, the cryostat sample chamber was pumped to 5×10^{-5} Torr. Figure 15(c) shows both the heating and cooling curves for two wavelengths, $\lambda = 2.5$ µm and $\lambda = 10$ µm, corresponding to the near-

42

infrared and mid-infrared respectively. For the near-infrared heating curve (red solid line), the transition begins at 57 °C and finishes at 77 °C (λ = 2.5 µm). For the near-infrared cooling curve, the transition takes place between 37 °C and 57 °C, resulting in a hysteresis of 20 °C. This hysteresis could likely be reduced by a different choice of substrate, such as quartz, or by increasing the thickness of the deposited VO_2. The transmittance change over the transition regime for the near-infrared wavelengths is 26%. Similarly, Sample B has a 17% change in the mid-infrared (λ = 10 µm) and the transition regime for both heating and cooling is identical to that for λ = 2.5 µm.

The VO_2 can be considered as an inhomogeneous composite medium to aid in the description of its optical properties during phase transition. The filling fraction f is the fraction of material in the composite that is metallic. At low temperatures, when VO_2 is insulating, the filling fraction is 0. Once the start of the transition temperature range is reached, metallic inclusions begin to form in the VO_2 film and the filling fraction increases from 0 to 1 with temperature. After the temperature has increased beyond the upper limit of the transition range, the filling fraction will be 1, indicating that all of the VO_2 is metallic. The transition VO_2 can be modeled by considering the material as a composite medium of insulating and metallic constituents. The Bruggeman effective medium theory (EMT) is employed here to model the effective dielectric constant of the fabricated sample during the phase transition [85]:

$$f \frac{\varepsilon_m - \varepsilon_{eff}}{\varepsilon_{eff} + q(\varepsilon_m - \varepsilon_{eff})} + (1 - f) \frac{\varepsilon_d - \varepsilon_{eff}}{\varepsilon_{eff} + q(\varepsilon_d - \varepsilon_{eff})} = 0 \qquad (26)$$

where ε_{eff} is the effective dielectric constant, ε_m and ε_d are the metallic and insulating dielectric functions. The depolarization factor q describes the shape of the inclusions in the

43

composite medium. In this case, since the VO$_2$ film is very thin, the inclusions are assumed to be disk-shaped, which have a corresponding q of 0.5. The filling fraction f at each selected temperature is determined by a least-squares fitting between the experimental transmittance and the modeled transmittance. The metallic and insulating dielectric functions are given by the models described in Section 4. In Figure 15(d), the fitted filling fraction is show for each temperature point collected during the experiment.
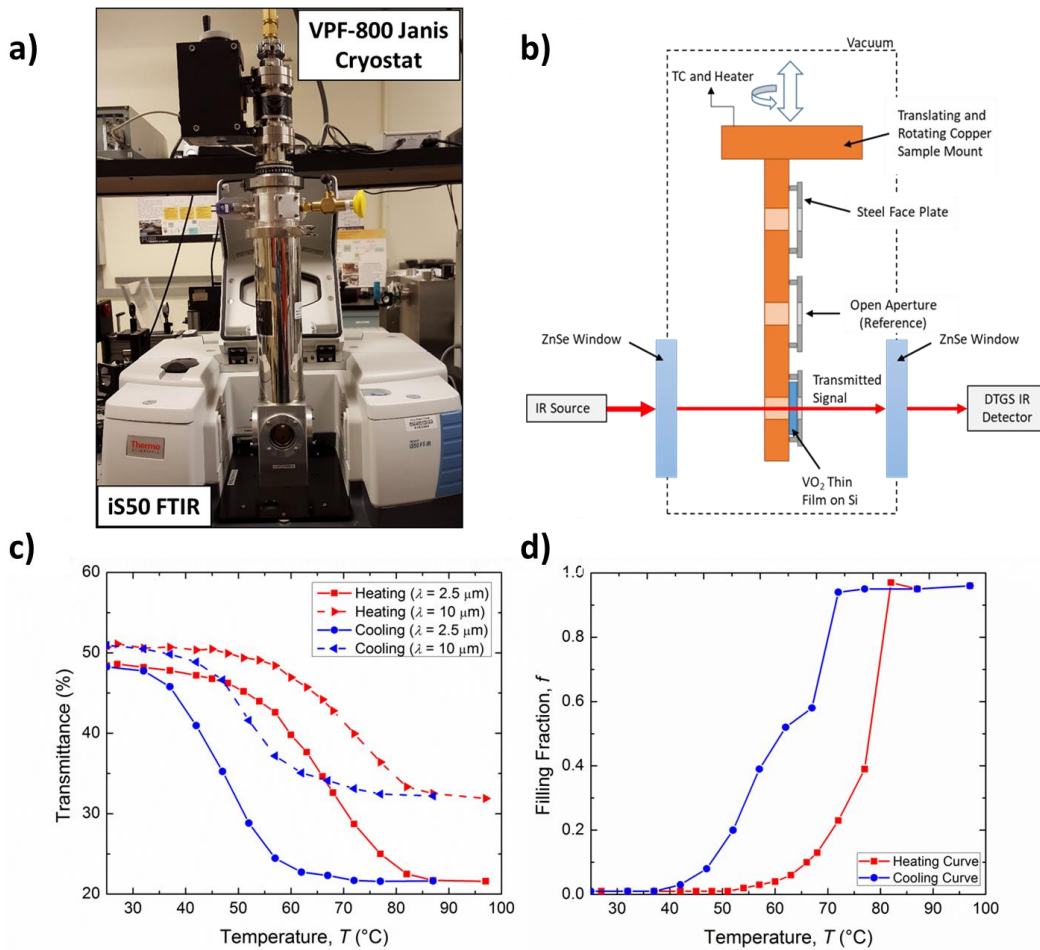
Figure 15. (a) Experimental set-up and (b) schematic of the temperature-dependent transmittance experiment in vacuum. (c) Heating and cooling curves for Sample B and (d) temperature-dependent filling fraction for VO$_2$ in phase transition upon heating and cooling for selected temperatures.

Besides the full heating and cooling hysteresis, the hysteresis when the VO_2 is only partially heated and then cooled is also of interest, especially for transient systems modeling. It has not been previously reported whether the VO_2 would transition back to the insulating state along the same curve as if it had been fully heated beyond the conclusion of the transition, or if another trend would emerge. To answer this question, a 60-nm-thick VO_2 thin film was prepared on undoped silicon to characterize the partial heating effect on the hysteresis in the infrared regime. As with the full heating and cooling curve measurement, the partial hysteresis measurements were taken using the Janis VPF-800-FTIR cryostat. The vacuum pressure was maintained below 5×10^{-5} Torr and the temperature was controlled with the Lakeshore 335 cryogenic temperature controller. Once the setpoint temperature was reached, 15 minutes were allotted to allow the sample to reach steady-state. Figure 16(a) shows the temperature-dependent FTIR measurements for the VO_2 when it is heated one quarter through the transition range and then cooled, while panels (b) and (c) show the results for halfway heated and three quarters of the way heated. In each figure the full heating and cooling curves are shown for reference. From the figure, it is clear that if the VO_2 is partially heated, the hysteresis upon cooling will be different than if the VO_2 had been heated to a temperature beyond its transition range. An empirical expression is developed here to assist with modeling efforts. The transmittance of the VO_2 thin films during cooling after partial heating at a given temperature T, $\Gamma_p(T)$, can be described by a simple proportionality expression:

$$\frac{\Gamma_i - \Gamma_f(T)}{\Gamma_i - \Gamma_m} = \frac{\Gamma_i - \Gamma_p(T)}{\Gamma_i - \Gamma_p(T_h)} \tag{27}$$

45

where Γ_i is the transmittance when the VO$_2$ is purely insulating, $\Gamma_f(T)$ is the transmittance for the full cooling curve at the given temperature, T_m is the transmittance when the VO$_2$ is entirely metallic, and $\Gamma_p(T_h)$ is the transmittance when the VO$_2$ is partially heated to temperature T_h. Figure 16(d) shows the normalized transmittance for the full and partial heating curves, where 0 indicates entirely insulating VO$_2$. A normalized transmittance change of 1 indicates the composition of the VO$_2$ at the temperature when it was allowed to cool (metallic for the full heating curve, and a mix of insulating and metallic VO$_2$ for the partial heating curves). As can be seen in the figure, for a given temperature, of the portion of VO$_2$ that had transitioned during heating, the percentage that had transitioned back when that temperature was reached during cooling is the same for the full heating, quarter heating, half heating, and three quarters heating curve. A similar trend is likely to exist for the fabricated Fabry-Perot emitter sample as well. The hysteresis characteristics of that sample will be discussed in the next chapter.
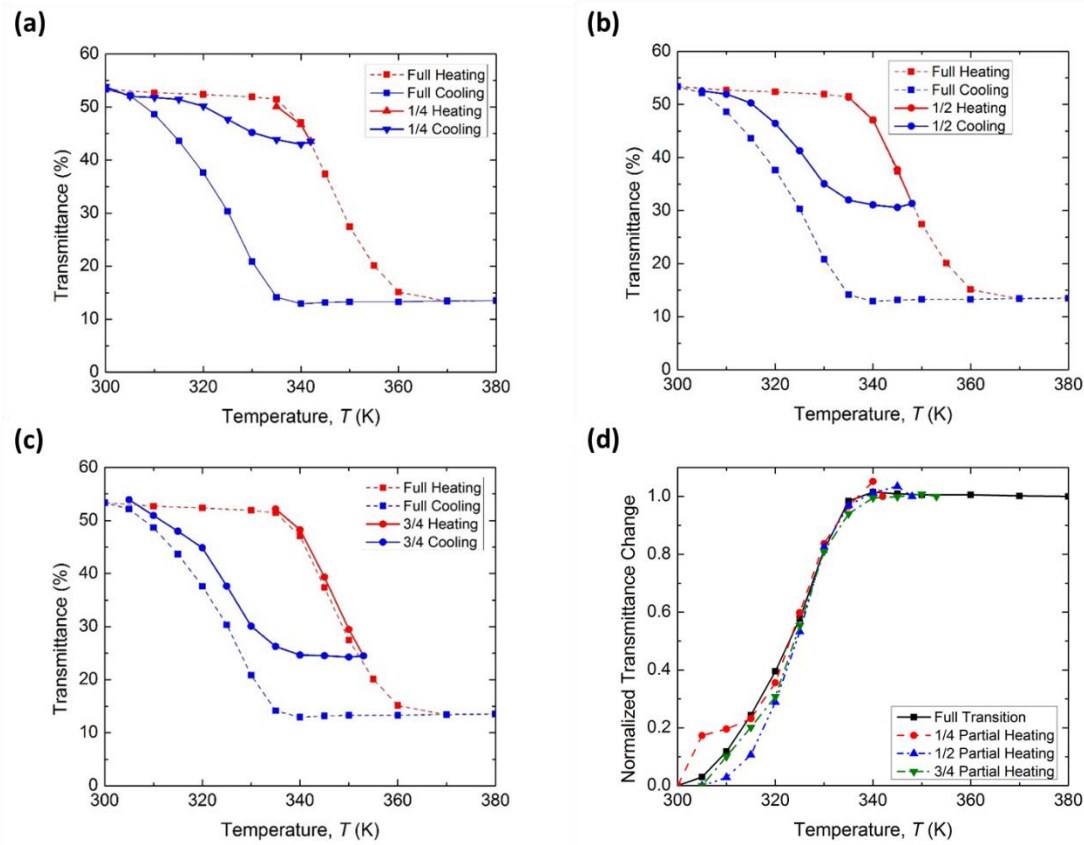
Figure 16. Temperature-dependent FTIR measurements for (a) one quarter partial heating, (b) one half partial heating, and (c) three quarters partial heating. (d) Normalized transmittance change for the full and partial heating curves.

The temperature stability of the VO₂ thin films is also of concern for thermal control coatings based on VO_2, particularly for spacecraft thermal control coatings, where the coating may be exposed to cryogenic or high temperatures. Besides exposure to extreme temperatures, thermal cycling may also be of concern for many thermal control applications. To address these concerns, the optical properties of the VO_2 thin films were measured at both cryogenic temperatures, and high temperatures (up to 450 °C). The VO_2

thin films were cycled 10 times between room temperature and cryogenic temperatures to determine if thermal cycling would have an impact on the optical properties of the films. From Figure 17(a), it can be seen that the transmittance of the VO_2 thin films at $T = 300$ K and $T = 77$ K is nearly identical, indicating excellent cryogenic thermal stability. Additionally, the VO_2 thin films were cycled between 300 K and 77 K ten times to demonstrate their stability under thermal cycling. The temperature was held for half an hour at both 77 K and 300 K for each cycle. The ramp rate for the heating and cooling was 15 K/min. As shown in Figure 17(a), the thermal cycling did not have a significant impact on the transmittance. After the experiment, the sample was visually inspected and did not show any signs of delamination. The high temperature measurements for the VO_2 thin film are shown in Figure 17(b). From the figure it can be seen that, after heating beyond 200 °C, the VO_2 thin film starts to become unstable, as seen by the significant decrease in infrared transmittance, especially at longer wavelengths. After the experiment, the thin film sample did not transition back to the insulating state and there was a clear color change from lilac to tan. The maximum expected temperature for dynamic radiative cooling applications is not usually above 200 °C, so the VO_2 thin film's stability up to 200 °C is acceptable for the applications considered in this dissertation.
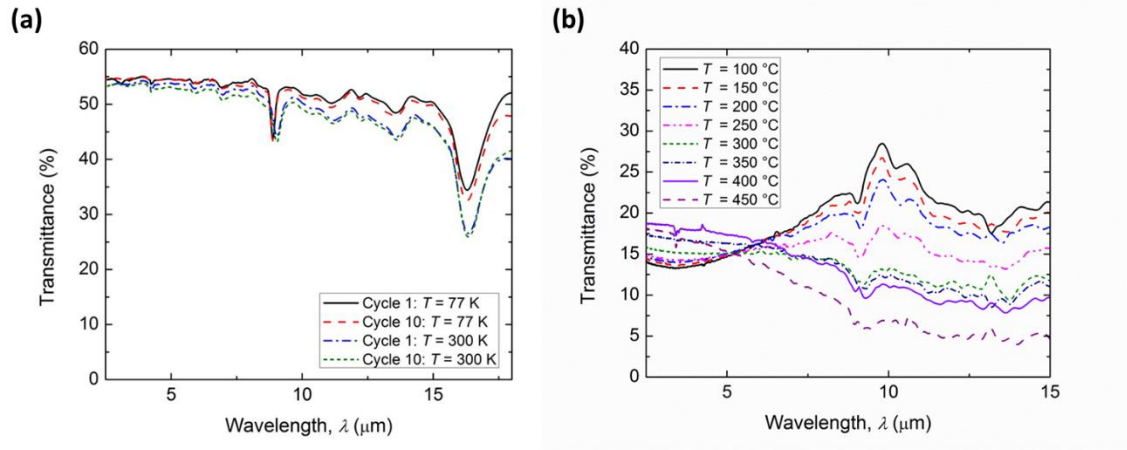
Figure 17. (a) Transmittance of VO$_2$ thin films at cryogenic temperatures, (b) transmittance of VO$_2$ thin films for high temperatures.

In this chapter, a facile and repeatable technique for stoichiometric VO$_2$ was developed. The resulting thin films were characterized and models were presented to describe the VO$_2$ optical properties in the insulating, transition, and metallic phases. The temperature-dependent optical properties and thermal performance were also measured to demonstrate the potential for dynamic radiative cooling applications. The nature of the transition hysteresis was also elucidated for partial heating of the VO$_2$ thin films samples. Finally, the temperature stability and thermal cycling durability of the fabricated VO$_2$ thin films was examined with temperature-dependent FTIR measurements in vacuum. The results from these measurements indicate good potential for VO$_2$ to be used in dynamic thermal control applications, laying a foundation for the development of the VO$_2$-based FP emitter coating discussed in the next chapter.

CHAPTER 4 OPTICAL CHARACTERIZATION AND EXPERIMENTAL DEMONSTRATION OF VARIABLE FABRY-PEROT EMITTER

This chapter discusses the sample fabrication, optical characterizations, and thermal performance for the FP emitter sample presented in Chapter 2. In Chapter 2, a silicon spacer inserted between a VO_2 thin film and an aluminum substrate was proposed as a variable emittance coating for dynamic radiative cooling applications. Additional studies have also proposed VO_2-based dynamic radiative cooling coatings for spacecraft applications. Sun et al. [104] fabricated a meta-OSR based on VO_2 that achieves a substantial increase in emittance upon VO_2 phase transition, however the emittance is not selective in the atmospheric window and the metasurfaces are fabricated via electron beam lithography, which is typically costly over large areas. Several studies have also investigated the performance of VO_2-based thin film designs. For example, Tazawa et al. [105], [106] simulated $SiO/V_{1-x}W_xO_2$/blackbody and $SiO/V_{1-x}W_xO_2$ stacks whose steady-state temperature could be tuned by altering the proportion of tungsten. In a recent work, Kort-Kamp et al. [107] designed a multilayered thin film stack with multiple layers of VO_2 that offered a considerable change in emittance. Ono et al. [108] designed a Fabry-Perot emitter consisting of a VO_2 thin film, MgF_2 spacer and a tungsten substrate with a top solar reflector that achieved excellent radiative cooling performance. Although the results from these theoretical studies show great promise for dynamic radiative cooling with VO_2 thin films, several challenges exist with the fabrication and experimental demonstrations of these devices. The designed devices require either many layers or thick layers (<1 µm) which are difficult to fabricate. Hendaoui et al. [109] fabricated a Fabry-Perot emitter with

50

a SiO$_2$ spacer that achieved excellent performance for dynamic spacecraft thermal control, however the phonon modes in the spacer material prevent the device from achieving spectral selectivity in the atmospheric window. The emitter sample studied in this dissertation work consists of an aluminum mirror, a silicon spacer, and a VO$_2$ thin film, respectively fabricated using electron beam evaporation, RF magnetron sputtering, and a furnace oxidation technique [110]. The high refractive index of the silicon enables a much smaller spacer thickness to be used, while the lack of strong phonon modes in the infrared regime makes it possible to achieve spectral selectivity in the atmospheric window. Sputtering is also employed in industry to fabricate coatings on large areas and non-planar geometries. The VO$_2$ and silicon layers can be applied to both aluminum structures and flexible foils with vapor deposited aluminum, which are extensively used in the aerospace industry.

In addition to the fabrication and temperature-dependent optical characterization of the proposed Fabry-Perot emitter, this chapter will also discuss two calorimetry-based thermal measurements that simulate a building ambient temperature and the space environment, respectively. In each case, the steady-state variable heat rejection of the fabricated sample will be experimentally demonstrated and compared to the theoretical performance. The effect of partial heating and cooling on the hysteresis for the Fabry-Perot coating will also be demonstrated with the cryothermal experiment that simulates the space environment. The effectiveness of the coating for both terrestrial and extraterrestrial dynamic radiative cooling is also predicted. Finally, the cryogenic and high-temperature stability of the proposed coating will be investigated.

4.1 Fabrication and Infrared Spectrometric Characterization

A well-performing selective radiative cooling coating should have high infrared emittance at high temperatures and low IR emittance at low temperatures (Figure 18a). The coating should have selectively high emittance around $\lambda = 10$ µm, which corresponds to the peak thermal emission of a body at room temperature. To achieve this selective behavior, the coating structure proposed in Chapter 2 is a Fabry-Perot (FP) resonance cavity consisting of: an opaque aluminum substrate mirror, a silicon spacer with 500 nm thickness, and a 60-nm-thick VO_2 thin film. When the VO_2 is metallic, the FP cavity is formed and the structure has high broadband emittance around the target wavelength (Figure 18b). The emission enhancement also spans the 8-13 µm atmospheric window, which is desirable for building cooling. On the other hand, when the VO_2 is insulating at low temperatures, the emittance of the metafilm structure is minimized (Figure 18c), as the VO_2 and silicon layers are semi-transparent, while the aluminum substrate is highly reflective. This change in emittance yields temperature-dependent heat rejection that can be used to design dynamic thermal management systems.
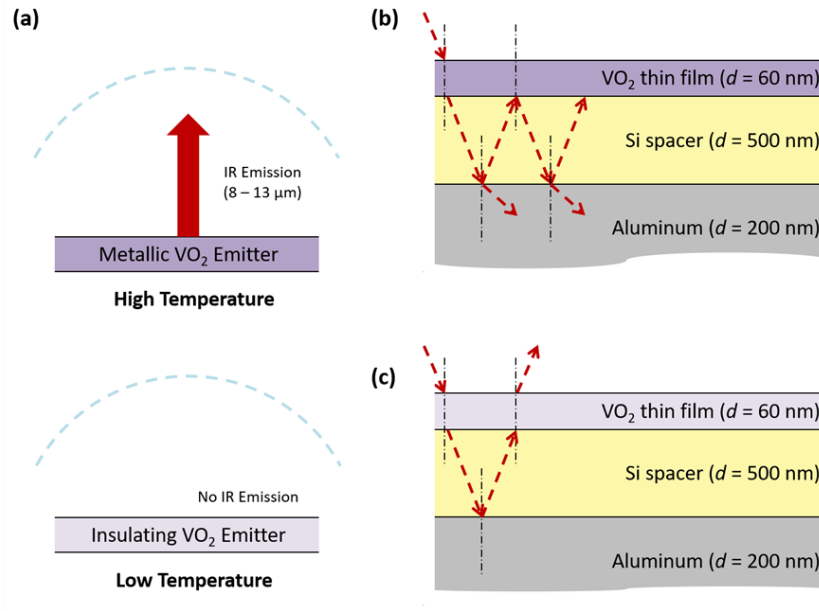
Figure 18. Schematics of (a) dynamic radiative cooling, and behaviors of the tunable metafilm emitter with (b) metallic VO_2 at high temperatures or (c) insulating VO_2 at low temperatures.

Figure 19 illustrates the final fabrication process developed for the VO_2-based tunable metafilm emitters using electron beam evaporation, RF magnetron sputtering, and thermal oxidation techniques. First, 200 nm of aluminum was deposited via electron beam evaporation (Lesker PVD75 Electron Beam Evaporator) from aluminum pellets (99.99% pure, Kurt J. Lesker Co) onto 385-µm-thick double-side-polished lightly-doped silicon substrates (Virginia Semiconductor, $\rho > 20$ Ω-cm) of 1 inch squares. The silicon substrates were pre-cleaned with isopropyl alcohol and blow dried with compressed nitrogen gas. The base pressure of the deposition chamber was 1×10^{-6} Torr and the rate was maintained at 2.5 Å/s throughout the deposition. After the aluminum deposition, a silicon spacer was RF magnetron sputtered (Lesker PVD75 Sputterer) onto the aluminum substrate layer from an

undoped monocrystalline silicon target (Kurt J. Lesker Co., $\rho > 1$ Ω-cm). The base pressure

of the sputtering chamber was 5×10^{-7} Torr and the deposition pressure was 3.0 mTorr. A

power of 135 W was used for the deposition, which yielded a silicon deposition rate of 0.4

Å/s. Due to concerns with substrate heating, the silicon was deposited in three 150-200 nm

intervals, with half an hour allotted for substrate cooling in between each interval. The

vacuum remained unbroken throughout the entire silicon spacer deposition. Two samples

were fabricated with slightly different Si spacer thicknesses of 430 nm and 500 nm

respectively for Sample 1 and Sample 2. Finally, a VO_2 thin film of the same thickness was

prepared for both samples using a two-step thermal oxidation process [111]. In the first

step, a pure vanadium film was deposited using electron beam evaporation (Lesker PVD75

Electron Beam Evaporator). Then the vanadium precursor thin film was oxidized in a tube

furnace (Thermco Minibrute) at 300 °C for 3 hours. The O_2 flow rate was 0.5 SLPM and

the N_2 flow rate was 60 SLPM throughout the oxidation.
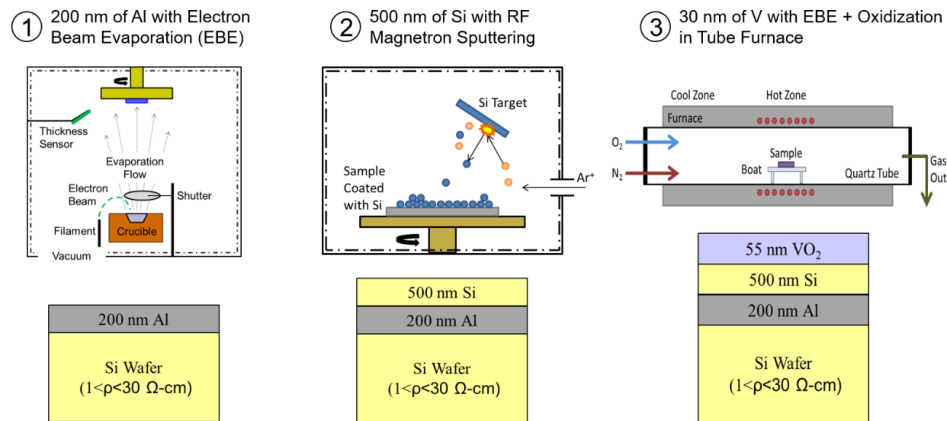
Figure 19. Fabrication processes for the tunable metafilm emitter (Sample 2): (1) a 200-nm-thick aluminum mirror is deposited by electron beam evaporation; (2) a 500-nm-thick silicon spacer is RF magnetron sputtered onto the substrate mirror; (3) a 60-nm-thick $_2$ thin film layer is prepared via a two-step furnace oxidation method.

One concern with using sputtered silicon was that the roughness of the sputtered film may lead to some discrepancies between the predicted performance and the experimental results. The topology of the film was examined via scanning electron microscopy (SEM) as shown in Figure 20(a). Further, the surface roughness of the silicon film was evaluated by an atomic force microscopy (AFM) measurement as shown in Figure 20(b), where the root-mean-squared (RMS) surface roughness of the Si film was determined to be 4.66 nm from the AFM topography measurement (Bruker Multimode). This value is comparable to the RMS roughness of the VO_2 from the thermal oxidation method [111] and is not believed to cause considerable scattering in the mid-infrared.
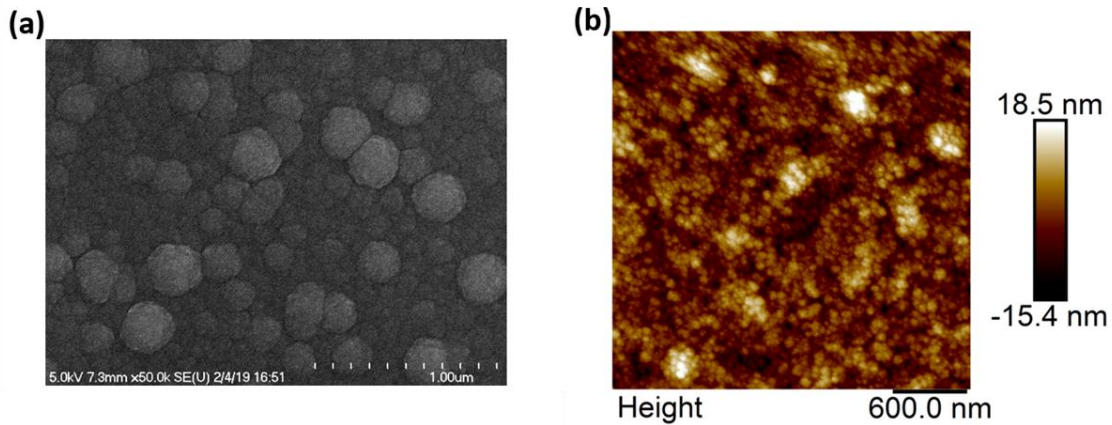
Figure 20. (a) SEM image and (b) AFM measurement for the sputtered silicon spacer on the 200-nm aluminum film and lightly doped silicon substrate.

To examine the optical quality of the sputtered silicon, the refractive index (n) and extinction coefficient (κ) in the infrared from 2 to 20 µm in wavelength were fitted from the modeling based on the spectral reflectance (R'_λ) and spectral transmittance (T'_λ)

measured by FTIR at room temperature. The 500-nm sputtered silicon layer was prepared

on an insulating 60-nm vanadium dioxide layer deposited on an undoped silicon substrate

(Figure 21a). The measured infrared radiative properties of this sample are presented in

Figure 21(b). The optical model combined thin-film optics for the sputtered Si layer and

insulating VO$_2$ film with ray tracing for the 500-µm-thick undoped Si substrate [87] as:

$$T'_\lambda = \frac{\tau_a \tau_s \tau}{1 - \rho_s \rho_b \tau^2}$$ (28)

$$R'_\lambda = \rho_a + \frac{\rho_s \tau_a^2 \tau^2}{1 - \rho_s \rho_b \tau^2}$$ (29)

where τ_a is the transmittance from the air through the silicon and vanadium thin films, τ_s is

the transmittance from the bottom interface of the silicon substrate to the air, ρ_s is the silicon

substrate-air interfacial reflectance, and ρ_b is the reflectance from the silicon substrate

incident on the two thin films. Thin-film optics was used to determine τ_a and ρ_b. On the

other hand, τ_s and ρ_s were calculated from Fresnel's equations. Finally, the internal

transmittance coefficient (τ) is given by:

$$\tau'_\lambda = exp\left(-\frac{4\pi\kappa d}{\lambda \cos\theta_2}\right)$$ (30)

Note that the optical constants of the VO$_2$ film prepared by the furnace oxidation method

were obtained in Chapter 3. Therefore, the refractive index (n) and extinction coefficient

(κ) for the sputtered silicon layer are the only unknowns in the above system.

Figure 21(c) shows that the fitted refraction index for the sputtered silicon is about

3.4 over the infrared spectrum, which is consistent with the well-studied properties of

undoped silicon wafers [92]. Figure 21(d) shows the fitted extinction coefficient for the

sputtered silicon, which is likewise consistent with the typical properties of undoped silicon, except for in the longer wavelengths, where the extinction coefficient is slightly elevated. This may help to explain higher than expected emittance later on in the longer infrared wavelengths for the sample measurement at high temperatures.
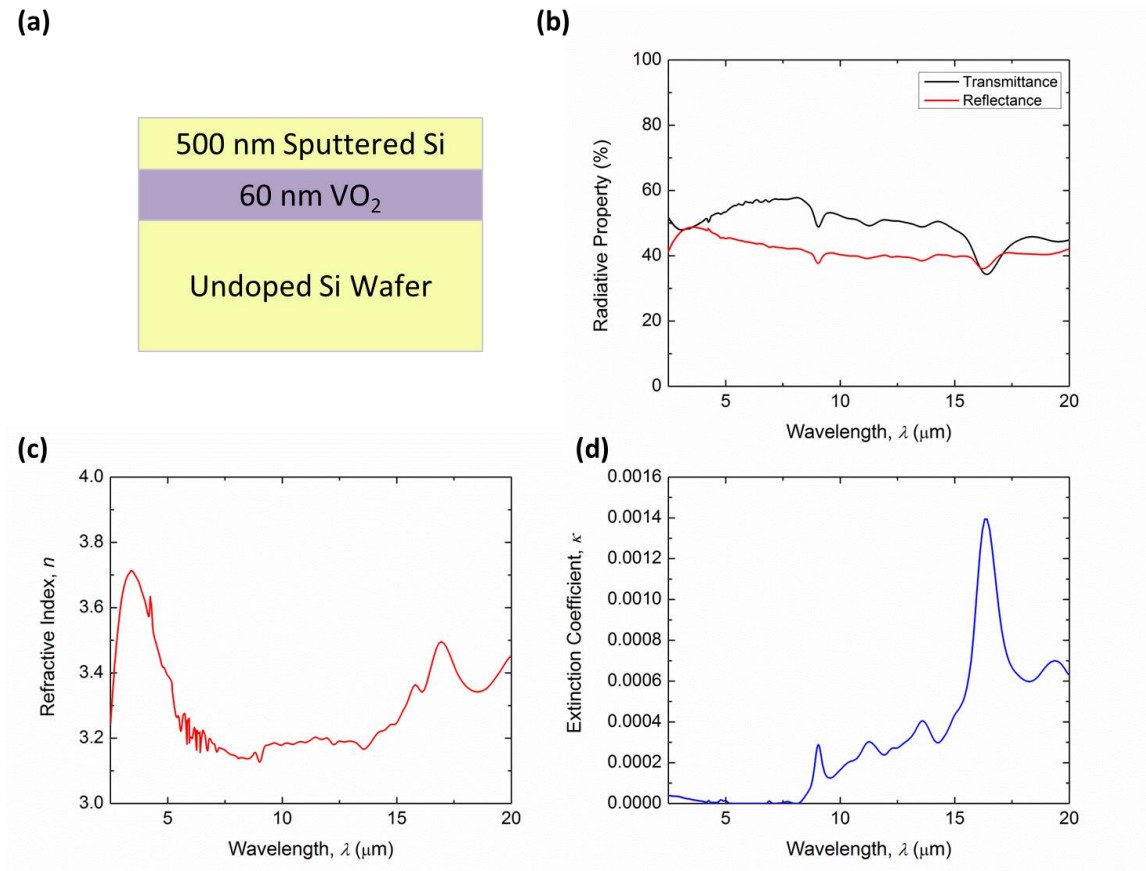
Figure 21. (a) Sample used to fit the optical properties for the sputtered silicon, (b) FTIR transmittance (black) and reflectance (red) measurements, (c) refractive index, n, and (d) extinction coefficient, κ, for the sputtered silicon.

The specular near-normal spectral reflectance of the fabricated emitter sample was measured using a Harrick Seagull reflectance accessory in a Thermo Scientific iS50

Nicolet FTIR spectrometer. The measurement was averaged over 32 scans, with a resolution of 16 cm^{-1}. A heater stage was used to vary the sample temperature from room temperature up to 100°C with an accuracy of 1.5°C from a K-type thermocouple. After the sample temperature reached the set-point, 10 minutes were allotted for the sample to reach steady state before the measurement was taken. Figure 22(a) shows the spectral near-normal reflectance at room temperature (i.e., 20°C) and 100°C for two fabricated samples. At room temperature, the reflectance is over 90% for nearly all of the mid-infrared wavelength range, indicating that the emittance, which is $\varepsilon'_\lambda = 1 - R'_\lambda$ for opaque samples, is less than 10% over most of the wavelength spectrum of interest. The reflectance dips near wavelengths $\lambda = 9$, 17, and 19 µm can be attributed to the phonons from the insulating VO$_2$ [111], while the larger reflectance dip near 7 µm in wavelength can be explained by weak FP resonance due to the index mismatch between air and the silicon spacer [82]. On the other hand, at 100°C, the spectral reflectance is only 5% near $\lambda = 9$ µm, indicating that the emittance is 95%. The experimentally observed variable emittance fits well with the expected behavior for dynamic radiative cooling (i.e., low emittance at low temperatures and high emittance at high temperatures). The spectra for both samples exhibit the same pronounced emission peak when the VO$_2$ is metallic, indicating good consistency between samples. The theoretical spectral normal reflectance was calculated via thin-film optics [87] for the fabricated tunable metafilm emitter (Sample 2), where the layer thicknesses were taken to be the measured thicknesses of the fabricated structure. The optical properties of the aluminum layer are determined from the Drude model with constants from Ref. [87]. The optical properties for the sputtered silicon and VO$_2$ layers were respectively fitted in

58

this chapter and in Chapter 3. Previous calculations also showed that the emitter was diffuse such that the total normal emittance and the total hemispherical emittance were nearly identical [82]. The theoretical temperature-dependent spectral reflectance of the fabricated emitter is plotted in Figure 22(b). At high temperatures, the metallic VO_2 along with the Al mirror form strong FP resonance inside the Si spacer. However, based on the thickness of the silicon spacer deposited for the fabricated sample, the theoretical emittance peak is located at ~6 µm, rather than the nearly 10 µm from the FTIR measurement, which might be due to temperature-induced phenomena either inside the sputtered silicon or inside the silicon-VO_2 interface upon heating. Both the theoretical and the experimental results show a near-unity peak in emittance upon phase transition. The evolution of the spectral normal emittance as the temperature is increased from room temperature to above the VO_2 phase transition is shown for Sample 2 (d_s = 500 µm) in Figure 22(c). One interesting characteristic to note is that the VO_2 layer transitions at a lower temperature in the shorter wavelengths, as evidenced by the quick rise of the emittance in the 5 µm to 10 µm wavelength range. At 75 °C, the VO_2 has completed its transition in all wavelength regimes, which can be seen by comparing the emittance at 75 °C and that at 100 °C. The total normal emittance ε_N of the fabricated sample is calculated via [32]:

$$\varepsilon_N = \frac{\int_{2.5 \ \mu m}^{20 \ \mu m} \varepsilon'_\lambda(T,\lambda,\theta=0)E_{b\lambda}(T,\lambda)d\lambda}{\int_{2.5 \ \mu m}^{20 \ \mu m} E_{b\lambda}(T,\lambda)d\lambda} \tag{31}$$

where $E_{b\lambda}$ is the spectral blackbody emissive power. As shown in Figure 21(d), the total emittance is low (i.e., 0.14) at temperatures below the VO_2 phase transition, upon which the total emittance increases to 0.60, making this thermochromic emitter a promising candidate for dynamic thermal control applications.

59
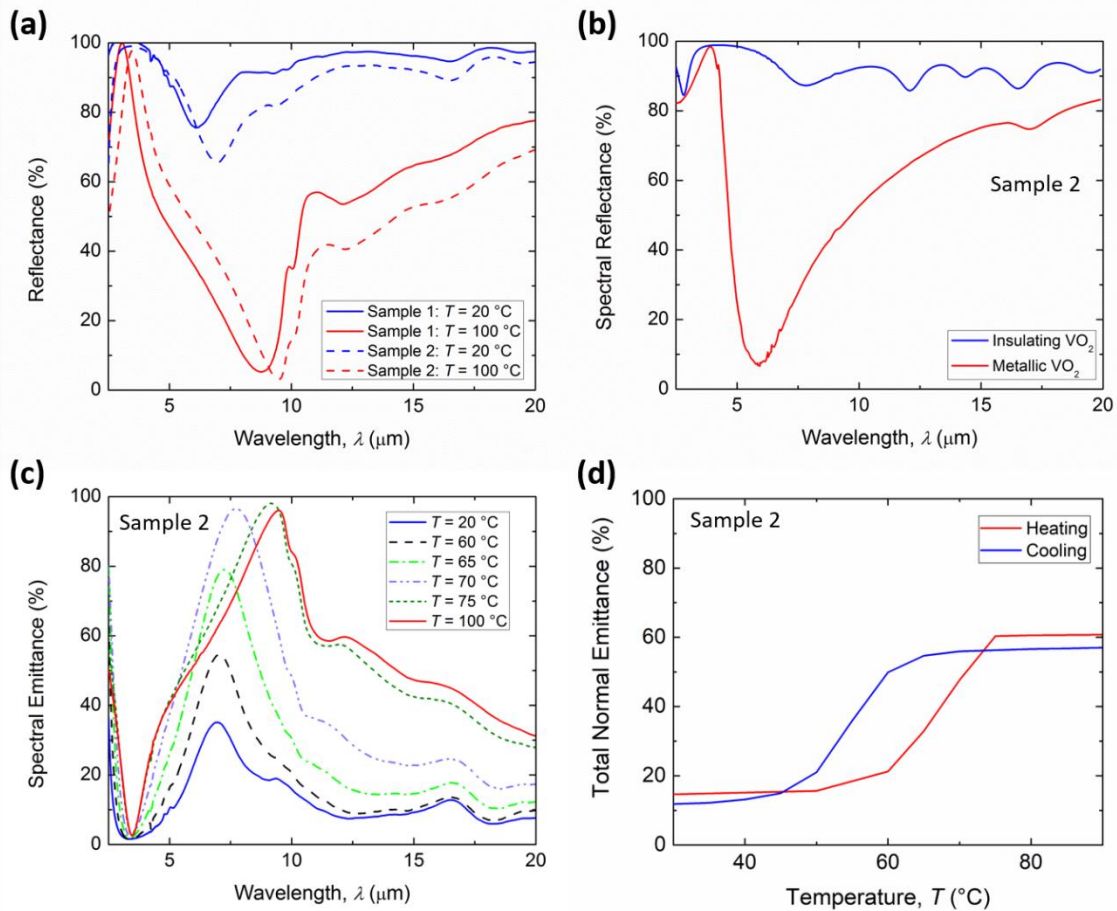
Figure 22. (a) Measured spectral reflectance of two fabricated tunable metafilm emitters at 20°C and 100°C (Sample 1 and Sample 2 respectively have a spacer thickness of 430 nm and 500 nm), (b) calculated spectral reflectance, (c) measured temperature-dependent spectral emittance, and (d) total normal emittance with temperature for Sample 2.

4.2 Bell Jar Thermal Test for Terrestrial Radiative Cooling

The variable heat rejection of the fabricated VO_2-based tunable metafilm emitter was demonstrated via a thermal measurement in vacuum, where Figure 23(a) illustrates the thermal vacuum measurement setup placed inside a 2 ft diameter bell jar vacuum chamber (Kurt J. Lesker Co.). The sample mount consisted of a 1" × 1" copper block which was

adhered to an identically sized kapton patch heater (Omega Inc.). The bottom surface of the patch heater was covered by aluminum foil to reduce the radiative loss. The emitter sample was placed on top of a copper block for uniform heating, while thermal paste (Ceramique Arctic Silver) was used at every interface to minimize the contact thermal resistance. A K-type thermocouple was inserted into the copper block to measure the sample temperature (T_s) and the wall temperature of the stainless-steel vacuum chamber ($T_w = 20\ °C$) was also monitored with another thermocouple. Due to the high thermal conductivity of the copper and the minimized contact thermal resistance, the sample temperature was assumed to be equal to the copper block temperature at steady state, which was defined by a less than 0.5 °C temperature change in 10 minutes. Electrical power was supplied to the patch heater in 0.5 V increments from 0 V to 9 V using a DC power supply (Keithley 2230-30-1), and the current I was measured to calculate the corresponding heater power from $Q_{heater} = I^2R$, where the heater resistance R was measured separately with a digital multimeter at room temperature.

In addition to the fabricated tunable VO_2 metafilm emitter (Sample 2), three other materials were also measured in the thermal vacuum emission tests for comparison. An aluminum mirror with a 200-nm-thick Al film deposited on a polished silicon wafer with nearly zero infrared emissivity represented the worst radiative cooling case, while a black sample (Acktar, Metal Velvet) with almost unity infrared emissivity was considered the best thermal emitter. It is expected that, for a given heater power, the aluminum should reach the highest steady state surface temperature while the black sample should reach the lowest, setting the upper and lower bounds for the thermal emission test. A double-side-

polished heavily-doped silicon wafer (Virginia Semiconductor, $\rho < 0.005$ Ω-cm) was also measured as a reference static emitter with negligible change in spectral emittance from room temperature up to 100°C to compare with the tunable VO_2 metafilm emitter with temperature-variable emittance. The spectral emittance of all three reference samples was measured via FTIR at room temperature as shown in Figure 23(b), making it possible to calculate their total emittance at a given temperature.

Figure 23(c) shows the steady-state sample temperature reached as a function of heater power input for all four samples. At low heater power, the VO_2 metafilm emitter achieved a steady-state temperature close to the aluminum mirror, since the total emittance is low (i.e., 0.14) at temperatures below the phase transition. As the sample was heated beyond the onset of the VO_2 phase transition around 60°C, the behavior changed abruptly and the VO_2 steady-state temperature trended sharply towards the behavior of the heavily-doped silicon sample, since the emittance of the tunable metafilm was significantly increased due to the strong FP resonance with the metallic phase of VO_2. Once the tunable metafilm sample was heated beyond the completion of the VO_2 transition, the trend changed again as the spectral emittance became static with high total emittance around 0.60 at 60°C.

The radiated heat flux of each sample can be determined from the experimental results and heat transfer model. As illustrated in Figure 23(a), the energy balance for the sample and mount at steady state is:

$$Q_{\text{heater}} - Q_{\text{rad}} - Q_{\text{cond}} - Q_{\text{sides}} - Q_{\text{bottom}} = 0 \tag{32}$$

where Q_{heater} is the heater power input, Q_{rad} is the heat radiated from the sample surface, Q_{cond} is the conduction loss through the pins used to mount the sample, Q_{sides} is the radiative loss from the sides of the sample mount, and Q_{bottom} is the radiative loss from the bottom of the sample mount. As the three major loss mechanisms were all dependent on the sample temperature, they can be combined into a total heat loss term as:

$$Q_{loss} = Q_{cond} + Q_{sides} + Q_{bottom} \tag{33}$$

The temperature-dependent heat loss Q_{loss} was obtained by fitting the experimental data from the aluminum sample as a function of sample temperature T_s. The aluminum sample was chosen to fit Q_{loss} due to its extremely low total emittance ($\varepsilon_{Al} = 0.03$) such that most of the heater power was dissipated through the losses. Thus, Q_{loss} was calculated from:

$$Q_{loss}(T_s) = Q_{heater} - \sigma \varepsilon_{Al} A_s (T_s^4 - T_w^4) \tag{34}$$

where σ is the Stefan-Boltzmann constant, and A_s is the sample surface area (i.e., 1 inch square). A linear fit, $Q_{loss} = aT_s + b$, was applied with the constants obtained as a = 0.0055 and b = 0.1113, to describe the Q_{loss} as a function of steady-state sample temperature as shown in Figure 23(d). With fitted expression for $Q_{loss}(T_s)$, the experimental radiated heat flux from other samples including the tunable VO_2 metafilm, black sample, and doped silicon, can be calculated via:

$$Q_{rad}(T_s) = Q_{heater} - Q_{loss}(T_s) \tag{35}$$

Figure 23(e) shows the heat flux, $q = Q_{rad}/A_s$, emitted by the surface of each sample measured at different steady-state sample temperatures T_s. As expected, the black sample has the highest emitted heat flux, while the aluminum has the lowest one. At temperatures

63

below the VO₂ transition temperature regime, the tunable metafilm emitter exhibits little heat rejection, as is desired at low temperatures, due to its low thermal emittance. As the temperature increases through the phase transition range, the emitted heat flux trends sharply upwards as the emittance of the tunable VO₂ metafilm increases. Finally, at temperatures beyond 75 °C, the slope of the emissive power with respect to temperature decreased as the tunable metafilm emitter completed the phase transition, since its spectral emittance became static again with a maximum total emittance value of 0.60. Note that for each sample, three independent thermal vacuum tests were performed with the steady-state temperatures averaged to calculate Q_{rad}. The uncertainty of the thermal vacuum tests was considered from both statistical variation u_A, calculated as the standard deviation of the three tests, as well as system error u_B, obtained by the error propagation analysis from the accuracy of the current, heater resistance, temperature, and area measurements for Q_{rad}. The unexpanded combined error $u_C = \sqrt{u_A^2 + u_B^2}$ is reported here.

To validate the experimental results from the thermal vacuum tests, the theoretical radiative heat flux of each sample was also predicted. The total emittance ε is 0.685 for heavily-doped Si and 0.93 for the black sample [112], as determined by integrating the spectral emittance and spectral blackbody power at room temperature according to Eq. 30. By assuming the negligible change in the total emittance from room temperature to 100°C, the theoretical radiative heat flux for the black sample and doped silicon can be simply obtained from $Q_{rad} = \sigma \varepsilon A_s (T_s^4 - T_w^4)$. On the other hand, the theoretical radiative heat flux for the tunable VO₂ metafilm emitter is calculated from:

$$q = \int_{2.5\,\mu\text{m}}^{20\,\mu\text{m}} \varepsilon_\lambda(\lambda, T_\text{s}) E_{\text{b}\lambda}(\lambda, T_\text{s}) d\lambda - \int_{2.5\,\mu\text{m}}^{20\,\mu\text{m}} \varepsilon_\lambda(\lambda, T_\text{s}) E_{\text{b}\lambda}(\lambda, T_\text{w}) d\lambda \qquad (36)$$

where ε_λ is the measured spectral emittance of the tunable VO_2 metafilm emitter (Sample 2) at a given temperature. From Figure 23(e), excellent agreement between the experimental results and theoretical calculations can be clearly observed for the black, doped silicon, and tunable metafilm emitter samples, within the uncertainty.
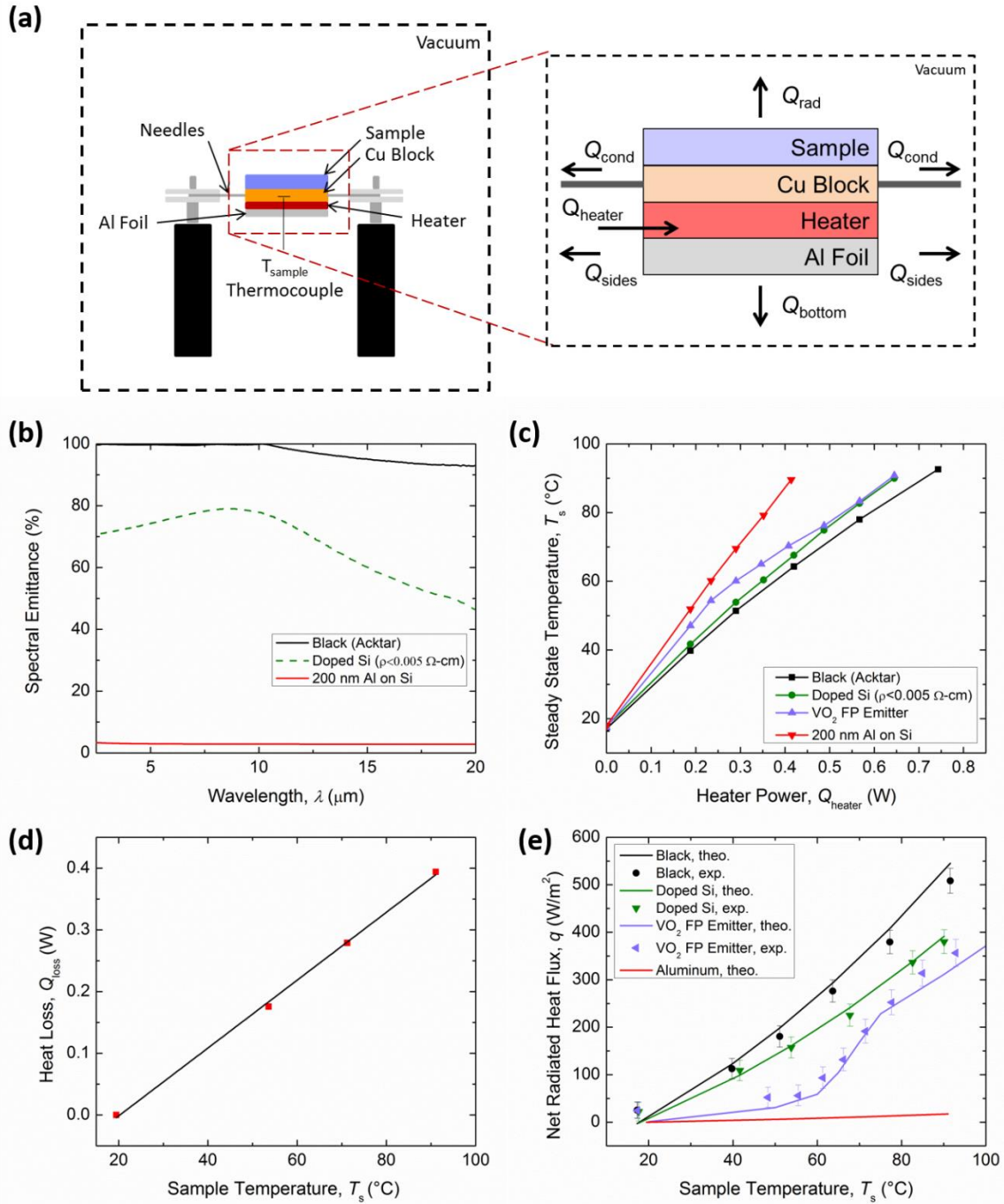
Figure 23. (a) Schematic for the thermal measurement (left) and heat transfer model (right), (b) spectral emittance for each reference sample measured at room temperature, (c) steady-state temperature achieved for a given sample and heater power input, (d) linear fitting for Q_{loss} as a function of sample temperature from the aluminum sample, and (e) the experimental (markers) and theoretical (solid lines) emissive power from each sample.

The wavelength-selective emittance peak in the 8 µm to 13 µm atmospheric window of the fabricated tunable metafilm emitter with metallic VO_2 indicates great promise for radiative cooling for terrestrial applications. If solar heating and convective heat transfer are neglected, the terrestrial radiative cooling power of the coating ($q_{rad,terr}$) can be calculated from [11], [22], [82]:

$$q_{rad,terr} = q_{rad,extraterr} - q_{atm} \tag{37}$$

Note that $q_{rad,extraterr}$ is the extraterrestrial radiative cooling power to outer space at 3 K:

$$q_{rad,extraterr} = \varepsilon_N \sigma T^4 \tag{38}$$

and q_{atm} is the radiation absorbed from the atmosphere:

$$q_{atm} = \int_{2.5 \ \mu m}^{20 \ \mu m} \varepsilon_{atm}(T_{atm}, \lambda) \varepsilon'_\lambda(T, \lambda) E_{b\lambda}(T_{atm}, \lambda) d\lambda \tag{39}$$

where T_{atm} is taken as 300 K for the atmospheric temperature. The atmospheric emittance is given by $\varepsilon_{atm}(\lambda) = 1 - t(\lambda)$, where $t(\lambda)$ is the AM1.5 transmittance spectra of the atmosphere in the zenith direction. Figure 24 shows the predicted radiative cooling power for both the extraterrestrial and terrestrial cases, where a significant switch upon the VO_2 phase transition can be observed. For the extraterrestrial case, a cooling power difference of 510 W/m^2 is achieved from 20 °C to 100 °C, whereas for the terrestrial case a cooling power difference of 445 W/m^2 is achieved. This clearly indicates good potential to use the tunable VO_2 metafilm emitter as a smart radiative cooling coating for both terrestrial and extraterrestrial thermal control applications. In practical systems, a solar reflector can be incorporated to minimize the solar absorption during daytime and maximize the performance of the VO_2-based dynamic radiative cooler. Several studies have investigated

67

1D photonic crystals and nano-particle embedded top layers that have near ideal solar reflectance and IR transmittance [10], [11], [21], [108]. Simulations with these solar reflectors have shown that they have minimal impact on the IR performance of the radiative coating while reducing the solar absorption to near zero. Therefore, the radiative cooling performance of the VO_2 FP emitter sample indicates good potential for use in both terrestrial and extraterrestrial thermal control applications.
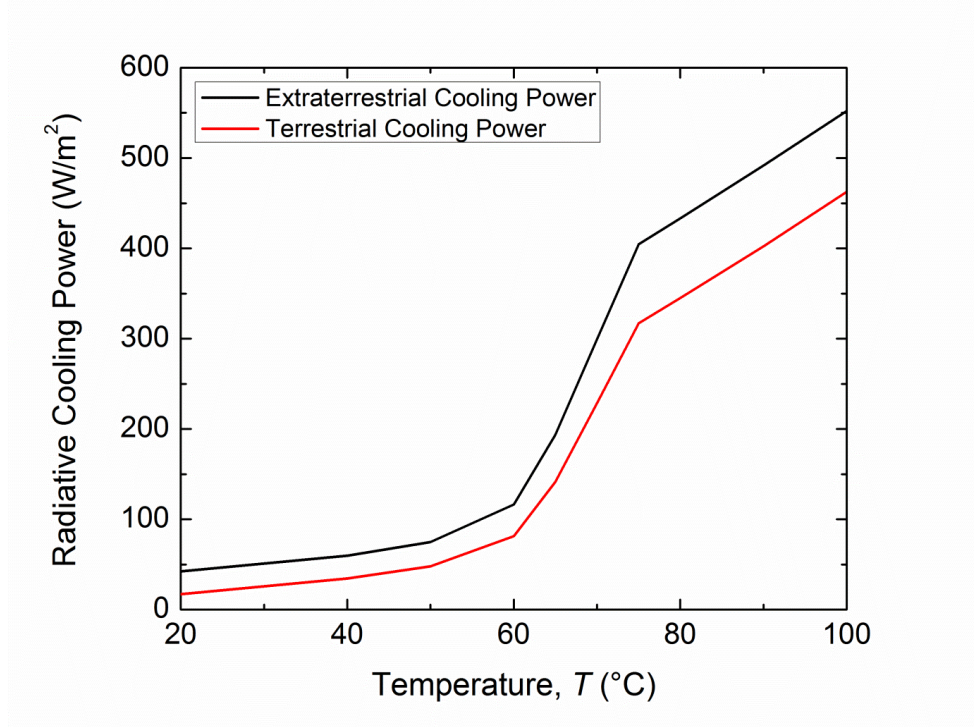
Figure 24. Calculated radiative cooling powers for extraterrestrial case to the outer space at 3 K (black line) and for terrestrial applications with ambient at 300 K (red line).

4.3 Cryothermal Test for Extraterrestrial Radiative Cooling

In addition to the ambient temperature bell jar experiment meant to simulate terrestrial applications, a cryothermal measurement was also developed to demonstrate the performance of the fabricated FP emitter in a "space-like" environment. A Janis VPF-800 liquid nitrogen cooled cryostat (Figure 25a) was used to conduct the variable heat rejection thermal measurement. The vacuum pressure was maintained below 1×10^{-3} Torr throughout the experiment to minimize convection. Figure 25(b) shows the schematic for the thermal vacuum measurement. The sample is secured with thermal paste (Ceramique Arctic Silver) to a 1" × 1" copper plate with a K-type thermocouple inserted, which is used to monitor the sample temperature. A 1" × 1" kapton patch heater is secured to the opposite face of the copper, where the exposed surface of the heater is covered by aluminum foil to minimize the radiation losses from the back side of the sample mount. The sample mount consisting of the sample, copper plate, and heater is pinned to the sample holder using needles to minimize the conductive heat transfer between the sample mount and cold finger. The needles were inserted into L-shaped brackets that bolted onto the cryostat cold finger. The 2" × 2" cold finger surface was covered by black Acktar to achieve an emissivity near unity, where the black surface was also secured by thermal paste (Ceramique Arctic Silver). The cold finger and sample mount were spaced such that the view factor from the sample surface to the cold finger was approximately equal to 1. The temperature of the cold finger was monitored using two E-type thermocouples (one at the top and one at the tip of the coldfinger surface) and was maintained between 77 K and 85 K throughout the experiment.

The heater power to the sample mount was increased in small increments for each sample and the steady-state temperature was observed for each heater input. Steady-state temperature is considered to be when the sample temperature has changed by less than 0.2 °C over 5 mins. Figure 25(c) shows the steady-state temperature achieved by each sample for a given heater input. As seen in the figure, each sample underwent three trials to ensure repeatability of the measurement results. As expected, the aluminum mirror achieved the highest steady-state temperature due to its low emissivity and minimal heat rejection (Figure 25d). The black sample achieved the lowest steady-state temperature due to its high emissivity and resulting high rejection. At low temperatures, the variable emitter sample exhibits behavior similar to the aluminum mirror due to its low emittance at low temperatures. As the temperature increases beyond the onset of the VO_2 transition range, the trend shifts as the emittance starts to increase. After the VO_2 transition is complete, the trend shifts again, exhibiting behavior more similar to the black Acktar due to its high emittance.

As with the ambient temperature bell jar set-up, the energy balance of the sample mount is described as:

$$Q_{\text{heater}} = Q_{\text{rad}} + Q_{\text{sides}} + Q_{\text{bot}} + Q_{\text{cond}} \tag{40}$$

where Q_{heater} is the heat supplied by the heater, Q_{rad} is the heat emitted from the sample surface to the black cold finger, Q_{sides} is the radiative heat loss from the sides of the sample mount, Q_{bot} is the radiative heat loss from the bottom of the sample mount, and Q_{cond} is the heat loss through the needles used to pin the sample mount in place. Since Q_{sides}, Q_{bot}, and

Q_{cond} are independent of the sample being measured, they can be combined in a single loss term, Q_{loss}, that is only a function of the steady-state temperature.

$$Q_{loss} = Q_{sides} + Q_{bot} + Q_{cond} \qquad (41)$$

So then the energy balance for the sample mount in steady state becomes:

$$Q_{heater} = Q_{rad} + Q_{loss} \qquad (42)$$

The heater power is measured in the experiment and the loss term can be fitted using a reference sample. The aluminum sample was chosen as the reference due to its low heat rejection. Since the heat rejection is minimal, most of the heater input power is lost via conduction through the needles, as well as radiation from the bottom and sides of the sample mount. Given the theoretical emittance of the aluminum, as in the previous section, the loss term as a function of steady-state temperature can be determined for the cryothermal sample mount (Figure 25d). This expression, $Q_{loss} = 0.007T_s + 0.46$, can be used to find the radiated heat flux from the sample surface for the VO_2 FP emitter and black sample. The temperature-dependent shift in heat flux is readily apparent for VO_2 in Figure 25(e), where is switches rapidly from 150 W/m^2 at the onset of the VO_2 phase transition at 60 °C, to 450 W/m^2 at the conclusion of the VO_2 phase transition at approximately 80 °C. On the other hand, the other two samples showed a linear increase in heat flux with temperature, as expected for static emittance coatings.

The experimental performance of the FP emitter and black sample is also in good agreement with the theory, as seen in Figure 25(e). The contribution from the 77 K cold

finger radiative sink is assumed to be negligible, therefore the radiative heat flux from the coating surface can be calculated as:

$$Q_{\text{rad}} = \sigma \varepsilon A_{\text{s}} (T_{\text{s}}^4 - T_{\text{w}}^4) \tag{43}$$

The variable heat rejection observed for the VO$_2$ FP emitter in the "space-like" cryothermal experiment indicates good potential for the Fabry-Perot coating to be used in spacecraft thermal control applications. A practical concern is the hysteresis behavior of the Fabry-Emitter coating during partial heating and cooling cycles. The Fabry-Perot emitter was heated to one quarter and one half of the way through the VO$_2$ transition temperature regime to illustrate the hysteresis behavior. In Figure 26, the radiated heat flux as a function of steady-state temperature can be seen for the Fabry-Perot sample, with the red solid curve representing the full VO$_2$ phase transition, the black dash dotted curve representing the cooling hysteresis when the VO$_2$ is heated one quarter of the way through the transition, and the blue dashed curve representing the cooling hysteresis when the VO$_2$ is heated one half of the way through the transition. Similar to the VO$_2$ thin films, a proportional expression can be introduced to describe the emittance hysteresis of the VO$_2$ Fabry-Perot emitter for cooling after partial heating.

$$\frac{\varepsilon_{\text{f}}(T) - \varepsilon_{\text{i}}}{\varepsilon_{\text{m}} - \varepsilon_{\text{i}}} = \frac{\varepsilon_{\text{p}}(T) - \varepsilon_{\text{i}}}{\varepsilon_{\text{p}}(T_{\text{h}}) - \varepsilon_{\text{i}}} \tag{44}$$

where $\varepsilon_{\text{p}}(T)$ is the emittance during cooling after the partial heating for a given temperature T, $\varepsilon_{\text{f}}(T)$ is the emittance for the full cooling curve at temperature T, ε_{i} is the emittance when the VO$_2$ is insulating at low temperatures, ε_{m} is the emittance when the VO$_2$ is metallic, and $\varepsilon_{\text{p}}(T_{\text{h}})$ is the emittance when the VO$_2$ was partially heated to temperature T_{h}.

72
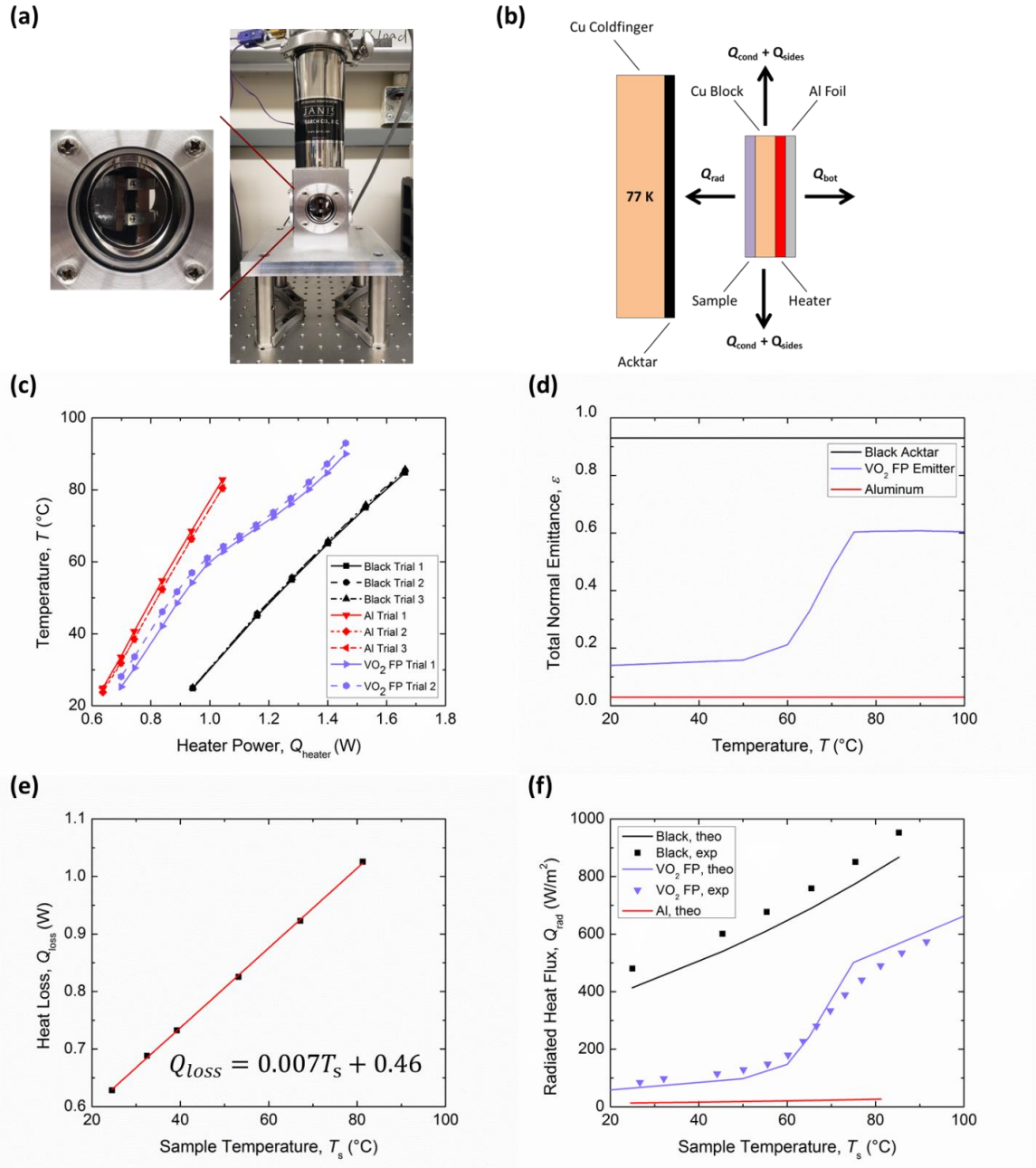
Figure 25. (a) Photo of the cryothermal vacuum experiment set-up, (b) experiment schematic, (c) steady-state temperature achieved by each sample trial as a function of input heater power, (d) total normal emittance for the measured samples, (e) heat loss term fitting to the aluminum sample, and (f) temperature-dependent heat rejection for the measured samples.
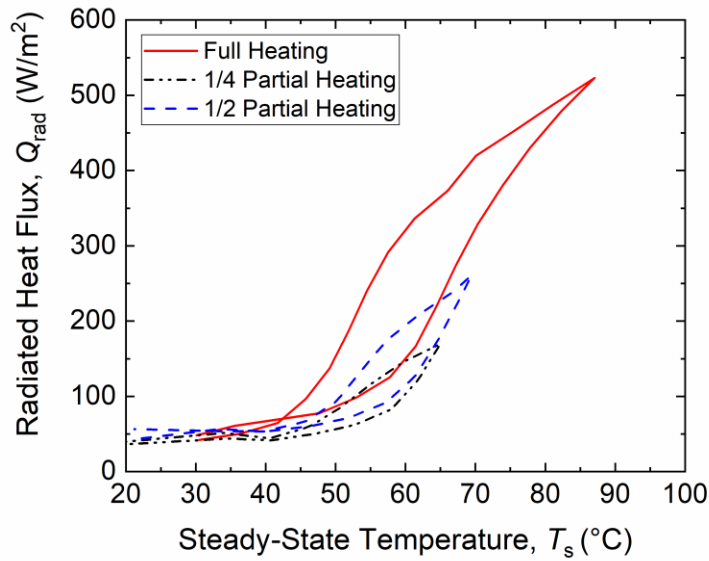
Figure 26. Partial heating and cooling hysteresis of Fabry-Perot emitter measured from the cryothermal experiment.
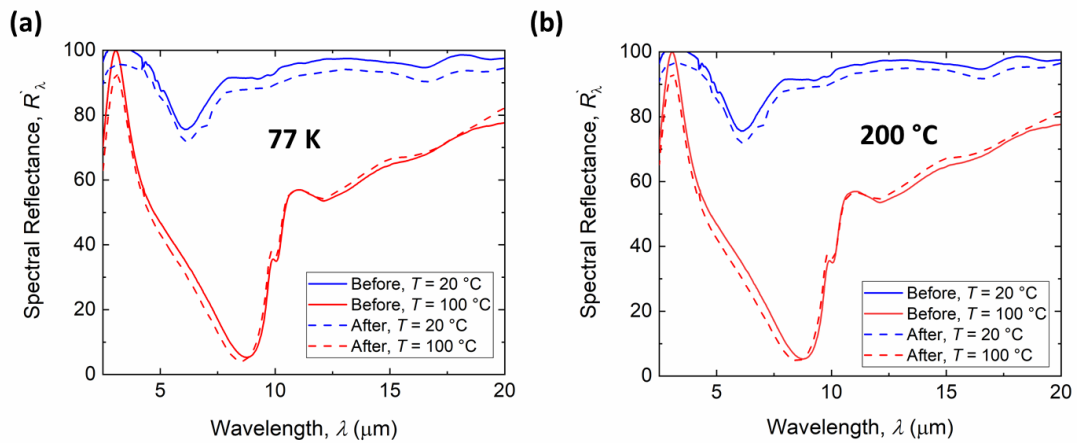
Figure 27. Before and after FTIR measurements for: (a) 77 K cryogenic cold soak and (b) 200 °C high temperature soak.

As with the VO_2 thin films, the temperature stability of the FP emitter sample is assessed for both cryogenic and high temperatures. Sample 1 was cleaved into two pieces,

used to test the cryogenic and high temperature stability, respectively. First the "before" spectral reflectance was measured at both room temperature, $T = 20$ °C, and at high temperature, $T = 100$ °C, past the VO_2 transition range. Then the samples were placed in the FTIR cryostat and were cooled or heated for 4 hours under vacuum. Figure 27(a) shows the before and after reflectance measurements for the FP emitter piece that was cooled, while Figure 27(b) shows the before and after measurements for the piece that was heated. From both figures, it is clear that the reflectance has not substantially changed for both the insulating and metallic VO_2 phases, indicating excellent temperature stability within the temperature range of interest for spacecraft thermal control.

Several challenges remain to be overcome before VO_2-based tunable emitters are practical for spacecraft or building thermal control. Foremost, the VO_2 phase transition temperature must be reduced to near room temperature for the coating to be practical for building thermal control applications, which might be achieved via impurity doping [46], [65], [78], [113], [114] and defect engineering with argon ion irradiation [57], [115]. Another concern is the durability of the VO_2 thin films under heating, humidity, and other relevant environmental factors [116]. Despite the remaining concerns that must be addressed, thermochromic tunable emitters have the potential to be useful for energy conservation in buildings and spacecraft thermal control by varying their heat rejection according to changing environmental conditions.

CHAPTER 5 THERMAL SYSTEMS MODELING FOR SPACECRAFT APPLICATIONS

In this chapter, a representative thermal model is developed to help determine what minimum performance the variable emittance must have to be useful for spacecraft thermal control applications. As part of this dissertation work, a representative human spacecraft modeling effort was undertaken to determine requirements for the variable emitter and to investigate its potential impact for human spaceflight vehicles. There are four major objectives for this modeling effort:

1. Determine what transition temperature range is required for human spaceflight applications

2. Determine the minimum emittance change required to achieve an acceptable turndown

3. Identify what types of missions would or would not benefit from variable emittance

4. Identify the most effective radiator designs for variable emitters

First, a simple steady-state hand calculation was performed in MATLAB to assess the transition temperature and emittance change needs for a representative human spaceflight mission. Then the assessment was broadened to include alternative radiator and thermal control configurations. The final analysis will include transient modeling of the VO_2-based variable emittance coating.

5.1 Steady-State Analysis of a Simple Variable Emittance Radiator

The spacecraft is assumed to be cylindrical with a diameter of 5 m (based on the current design for the Orion capsule) with body-mounted radiators fixed to the lateral surface of the cylinder. The radiator surface is discretized into 360 panels along the circumference of the cylinder [117], and each panel is further discretized into 10 blocks along its length. Figure 28 shows the discretization for the representative human spacecraft.
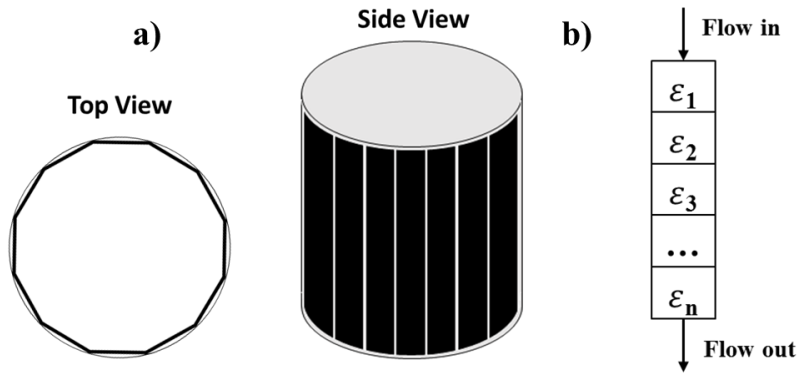
Figure 28. (a) Body-mounted radiator discretization for the cylindrical representative human spacecraft and (b) Radiator panel discretization into blocks with temperature-dependent emissivity.

The fluid lines are assumed to be a single path from one cylinder base to the opposite base. The flow path is as follows: (1) the total mass flow rate flows through a spacecraft heat exchanger which rejects $Q_{load} = 8500$ W to the working fluid, (2) the fluid is split evenly among the radiator fluid lines, (3) the 8500 W is rejected across all 360 panels, according to their surface temperature, (4) after the outlet of the radiator panels, the fluid is combined into a single line with the total mass flow, and (5) the fluid returns to the heat exchanger.

Figure 29(a) shows the fluid path through the spacecraft heat exchanger and the radiator panels.

The radiator is sized according to the hot case (Figure 29b), where a flat radiator perpendicular to the incident solar rays is considered. The temperature of the radiating flat panel was taken to be an average of the initial inlet temperature and the desired outlet temperature, $T_{rad} = \frac{(T_{in} - T_{out})}{2}$. The sink temperature, T_∞, is then calculated from:

$$T_\infty = \left(\frac{1}{\sigma}\left(\frac{\alpha}{\varepsilon} q_{sol} + q_{IR}\right)\right)^{1/4} \tag{45}$$

where σ is the Stefan-Boltzmann constant, ε is the high temperature emissivity of the variable radiator, and α is its absorptivity. The incident solar heat flux, q_{sol}, is taken as 432.5 W/m^2, which is the average heat flux over the lateral face of a cylinder where one half of the cylinder is shaded. For the initial study, the incident infrared heat flux, q_{IR}, is neglected. From the sink temperature, the radiator area, A_{Rad} is then sized by:

$$A_{Rad} = \frac{Q_{load}}{\varepsilon\sigma(T_{Rad}^4 - T_\infty^4)} \tag{46}$$

The variable emittance is modeled with a simple linear relation in the transition regime, with no hysteresis considered. Below the transition temperature lower bound, T_{low}, the coating has low emissivity, ε_{low}. Above the transition temperature upper bound, T_{high}, the coating has high emissivity, ε_{high}. The emissivity in the transition regime is modeled as $\varepsilon(T)$ = mT+b. The envelope considered for the four coating parameters is:

1. ε_{low} can vary between 0.3 and 0.6

2. ε_{high} can vary between 0.6 and 0.9

3. T_{high} must be between 4 and 20 degrees higher than T_{low}

78

This envelope is based on fabrication limitations and what seems possible based on the literature. With all of these elements in hand, a steady-state MATLAB code was developed to predict the radiator exit temperature (parameter of interest for human spaceflight applications) based on the four coating parameters listed above and the given heat load. The flowchart for the code is shown in Figure 30.
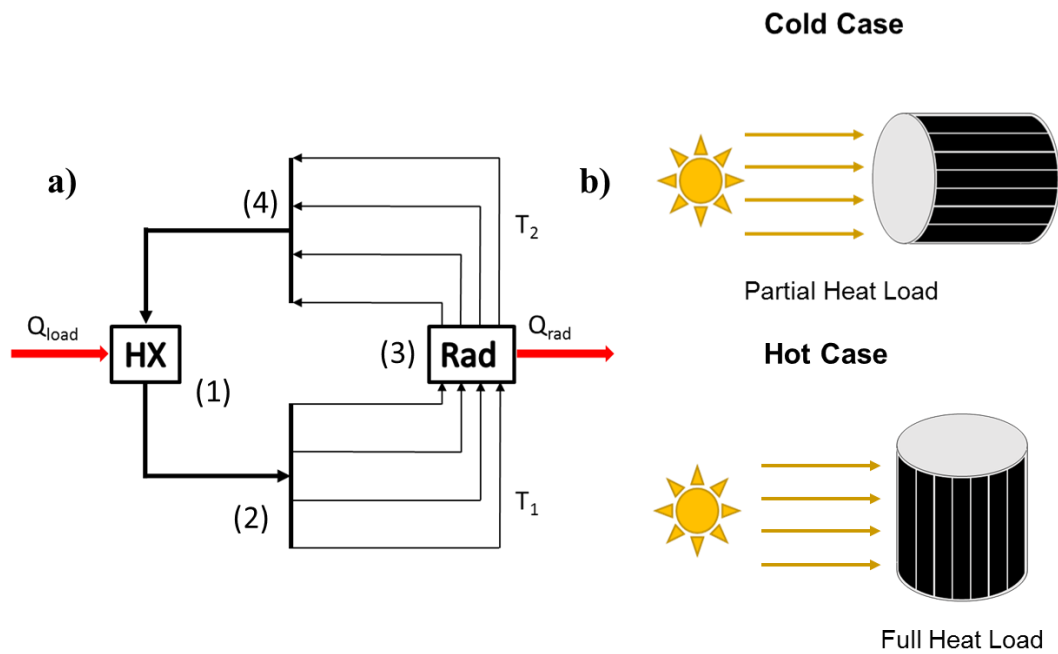
Figure 29. (a) Flow path of the representative human spacecraft and (b) cases considered for the study.
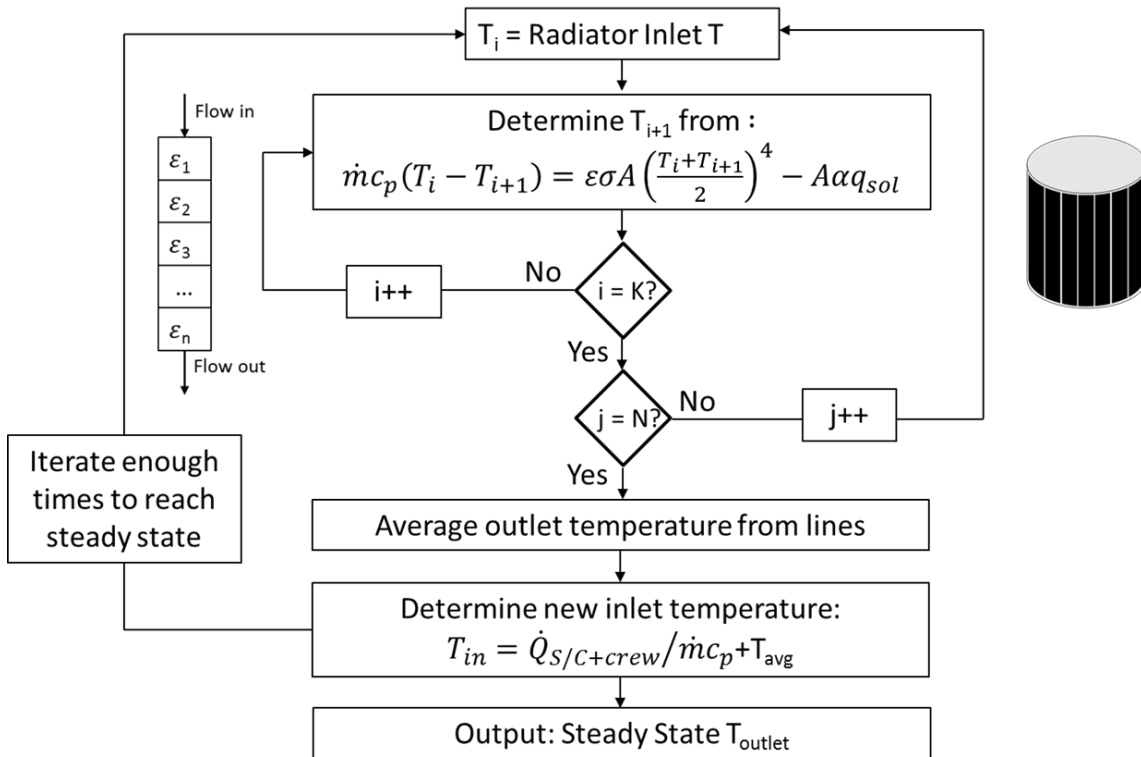
Figure 30. Flow chart for MATLAB code logic. First the temperature at the start and at the end of each radiator block is determined, and then the emissivity is updated based on the average temperature. The outlet temperature is determined for each radiator panel along the circumference of the cylinder and the new radiator inlet temperature is calculated based on the heat load input from the spacecraft heat exchange. This routine is iterated until a steady state solution is found.

The steady-state solution is found for both the hot case and the cold case in Figure 29(b). The performance of the variable radiator is then compared against a static radiator with $\varepsilon = \varepsilon_{high}$ and the same area to see the benefit over current technology. Figure 31 shows an example output for the model. In the hot case for both radiators, the maximum radiator outlet temperature occurs at a panel location of 90°, which is the subsolar point, or orientation exactly perpendicular to the incident solar rays. The variable radiator is shown

to run hotter than the static radiator in the cold case. This is because the emissivity at the end of the panels and on the cold of the cylinder is lower, so a high radiator area would be required to get the same outlet temperature as the static radiator. Therefore, the tradeoff for variable emittance radiators is potentially added radiator area to accommodate the hot case requirements versus turndown capabilities in the cold case. In the cold cases in Figure 31 the outlet temperature is consistent along the circumference of the spacecraft because there is no environmental heat load being imposed.
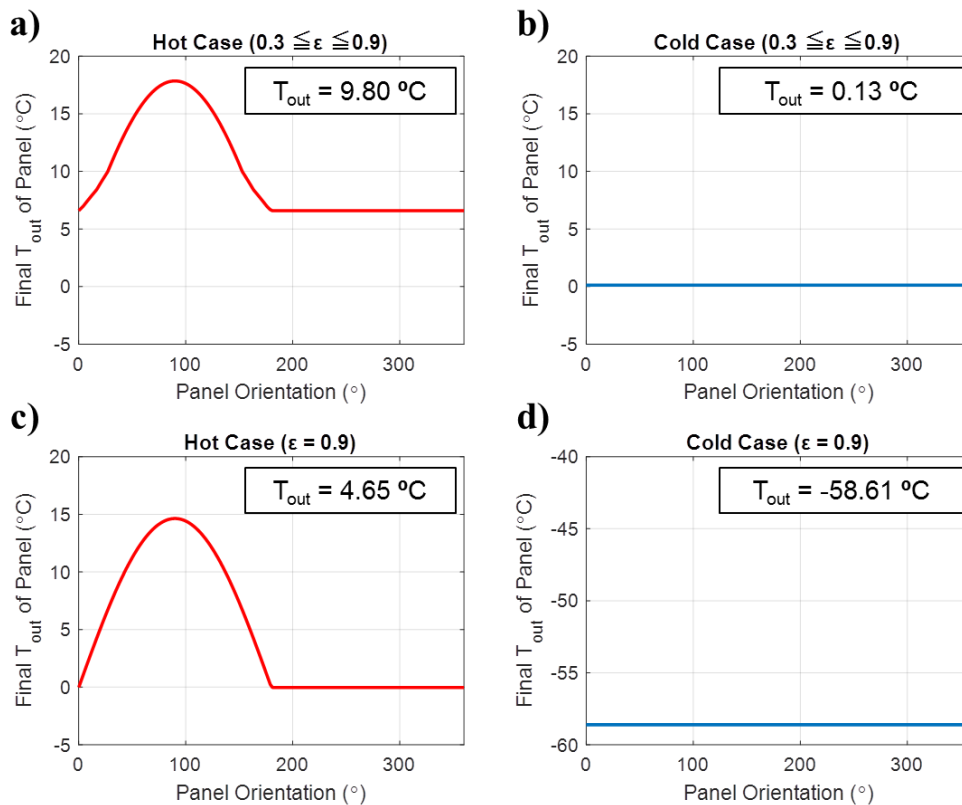
Figure 31. Radiator panel outlet temperature as a function of position on cylinder for (a) variable radiator in the hot case, (b) variable radiator in the cold case, (c) static radiator in the hot case, and (d) static radiator in the cold case. The boxed value is the average radiator outlet temperature for that scenario. The cold case considers 40% of the full spacecraft load.

81

The next step in this investigation was to determine the optimum transition temperature. There are two primary requirements for the optimization:

1. The average outlet temperature must be between 0 °C and 10 °C

2. The temperature of each radiator panel must be above -10 °C

The first requirement is derived from the needs of cabin heat exchangers and the second requirement is intended to prevent freezing of the transport fluid, propylene glycol water, in the radiator. The variable to be optimized is the turndown percentage, or the percentage of the maximum load that can be reduced to while still meeting the requirements. The optimization employed was a simple field search, where the steady solution was determined for a mesh of T_{low} and T_{high} temperatures. The emissivities were not optimized since the solution for these is clear: the bigger the difference in emissivity the better, and the higher both values are the better. For the optimization in Figure 32, $\varepsilon_{low} = 0.3$ and $\varepsilon_{high} = 0.9$, which represents the best possible emittance change expected from the fabricated coatings. The minimum turndown percentage is 40% for a transition from 7 °C to 11 °C. An interesting trend to note is that the best results are achieved with a very narrow transition range, which is something that could be addressed by changing the fabrication technique or the process conditions for the current furnace oxidation technique. Figure 32(b) shows the requirements that bound the search space.
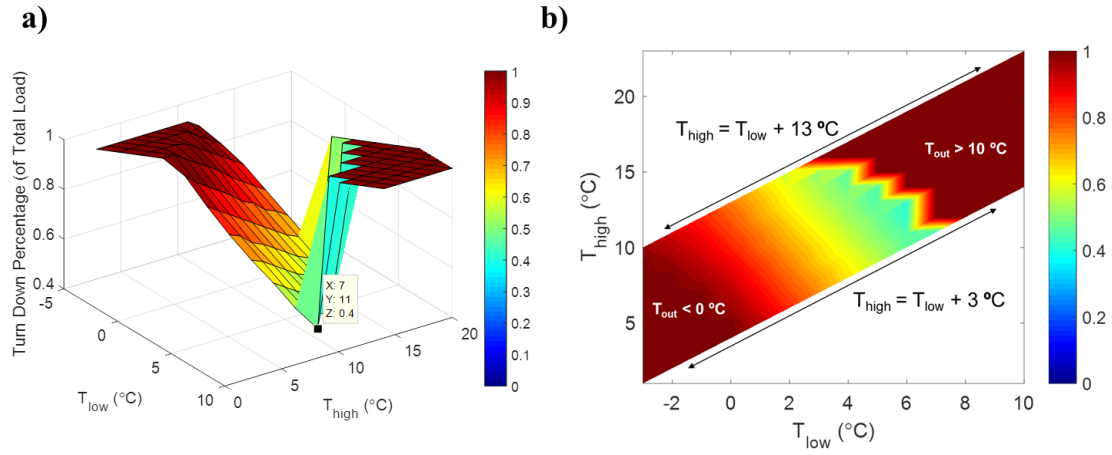
Figure 32. (a) Surface plot for the optimization space considered and (b) contour plot of the optimization envelope with the requirement limits denoted.

5.2 Investigation on Alternative Radiator Geometries

Additional investigations were done to assess what types of radiator geometries could best take advantage of variable emissivity technology. The previous section considered single flow radiator panels, with no thermal communication between panels. One idea to improve the radiator design was to have the fluid lines run along the circumference of the radiator, rather than from cylinder base to cylinder top. Figure 33(a) shows the configuration for the radial flow radiator. The MATLAB implementation for this geometry is similar to the implementation for the straight flow radiator, except that the panels are considered to be five circumferential fluid lines and the blocks are subdivided into 360 blocks along the circumferential line.

Figure 33(b) shows the outlet temperature of each block along the circumference of the cylinder and the corresponding emissivity for the optimized case. A lower turndown percentage of 35% is achieved for this geometry with a transition range of 8 °C to 13 °C. The behavior of the radial radiator did not seem to be as dependent on the location of the Sun as expected. The best performance was obtained with the subsolar point 90° clockwise from the inlet and outlet in Figure 33(a). Future alternative designs to consider may include counter-flow radiators, as well as other system elements like bypass valves, regenerators, etc. The results in this chapter provide a target transition temperature and minimum emittance change to aim for when designing variable emittance coatings for spacecraft thermal control applications.
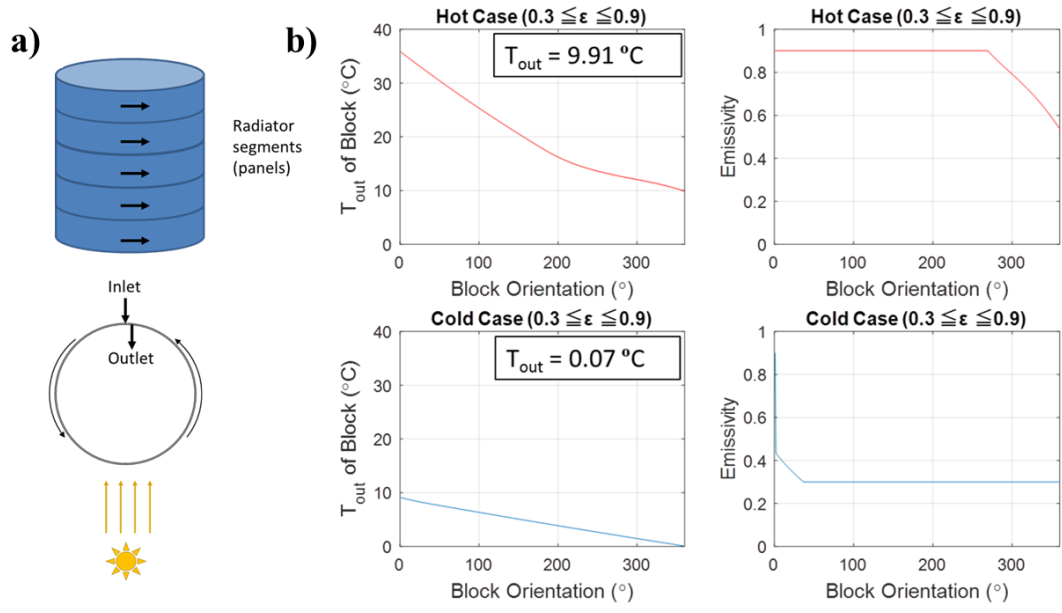
Figure 33. (a) Diagram for radial flow radiator and (b) block outlet temperature and emissivity as a function of orientation.

CHAPTER 6 VARIABLE REFLECTANCE COATING FOR OPTICAL FORCE MODULATION

The potential of VO_2 for another spacecraft application, optical force modulation, is explored in this chapter. Optical force modulation can be useful for spacecraft micropropulsion and attitude control. First, vanadium dioxide thin films are prepared on quartz substrates using a simple two-step thermal oxidation technique [111]. The film composition is investigated using x-ray diffraction and Raman spectroscopy, while the temperature-dependent optical properties are measured via FTIR spectroscopy. The heating and cooling curves are presented to demonstrate both the transition temperature range and hysteresis effect in the visible and near-IR. The optical properties for both the insulating and metallic phases of the fabricated VO_2 are fitted for the visible and near-IR wavelength ranges. Then the optical behavior of the VO_2 at cryogenic and high-temperatures is examined to elucidate the thermal stability of the fabricated films. Finally, a preliminary design for an optical force modulation coating is introduced and the performance is calculated both with properties available from literature, and from the properties derived from the furnace fabricated VO_2.

6.1 Visible and Near-Infrared Optical Characterization of Vanadium Dioxide Thin Films

A large change in the VO_2 transmittance is desired to facilitate the tunable behavior for optical force coatings for micropropulsion applications. For a variety of fabrication methods, VO_2 has exhibited a significant chance in optical properties in the near-IR

wavelength regime. For example, Malarde et al. [118] fabricated VO_2 on floating glass substrates via APCVD deposition which showed a 58% change in transmittance at a wavelength of $\lambda = 2.5$ µm for smart window applications. Similarly, Taha et al. [63] also fabricated VO_2 on several substrates using DC magnetron sputtering and were able to achieve a 50% change in transmittance for their VO2 on quartz samples at $\lambda = 2$ µm. Chang et al. [68] also fabricated Cr_2O_3/VO_2 bilayers via a low-temperature DC sputtering process with a V_2O_3 ceramic target which achieved a ~55% change at $\lambda = 2$ µm. The visible range, by comparison, changed little with temperature in each of these studies, however both the visible and near-infrared property change must be assessed to determine if VO_2 is suitable for optical force modulation applications. In addition to the property fitting, the cryogenic and high-temperature stability is also of interest for spacecraft applications where the temperature of the modulating surface may vary considerably.

A 60-nm-thick VO_2 thin film was fabricated on a 0.75" diameter, 0.50-mm-thick double side polished Z-cut quartz wafer (Precision Micro-Optics). First, 30-nm-thick pure vanadium was deposited onto the quartz substrate using electron beam evaporation (Lesker PVD75 Electron Beam Evaporator) from 99.99% pure 1/4" diameter 1/4" long vanadium pellets (Kurt. J. Lesker Co.). The deposition rate and chamber pressure were maintained at 0.7 Å/s and 3×10^{-6} Torr, respectively, during the deposition process. After the pure metal deposition, the precursor film was oxidized at 300 °C for 3 hours in a Thermco Minibrute ambient pressure tube furnace to produce a 60-nm-thick VO_2 thin film. Throughout the oxidation process, a mixture of 0.5 SLPM of pure O_2 and a 60 SLPM N_2 was flowed through the quartz tube. After the oxidation, the sample was allowed to cool in a pure N_2

purge flow for 10 minutes in the cold end of the furnace. The composition change of the thin film from metallic vanadium to insulating VO_2 is accompanied by a visual color change from grey to yellow. Figure 34(a) shows a photo of an unoxidized 30-nm-thick pure vanadium thin film (left) and the furnace oxidized vanadium dioxide film (right).

The composition of the prepared thin film sample was characterized by XRD and Raman spectroscopy. Figure 34(b) shows the XRD pattern for the VO_2 prepared on quartz substrate, where the peaks at the 2θ angles of 28°, 37°, 43°, 56°, and 65° are typical of polycrystalline vanadium dioxide [77]. There are no additional XRD peaks indicating the presence of other vanadium oxides, such as vanadium pentoxide (V_2O_5) or vanadium sesquioxide (V_2O_3), which do not contribute to the thermochromic switch of the fabricated thin film. Similarly, the Raman spectrum of the fabricated film as shown in Figure 34(c) was also measured with a 488 nm laser source and 100× objective (Renishaw InVia spectroscopy system), which was also consistent with polycrystalline VO_2. The thin film thicknesses of both the pure V metal (30 nm) and the VO_2 (60 nm) were determined using a contact profilometer (Bruker Dektak) to measure the height of a step prepared on the quartz substrate during the sample fabrication before and after the furnace oxidation process.
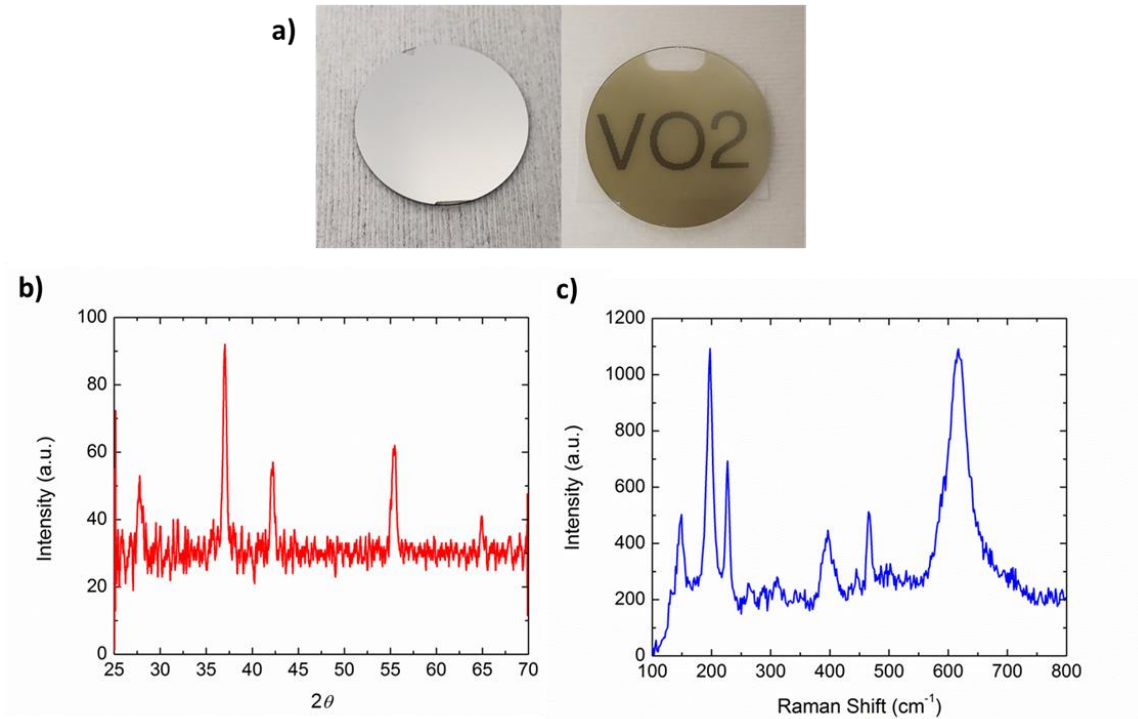
Figure 34. (a) Photos of the pure vanadium metal film on a quartz substrate (left) and the yellow oxidized vanadium dioxide thin film on a quartz substrate (right). (b) XRD pattern and (c) Raman spectrum for the oxidized film with typical peaks for vanadium dioxide thin film on a quartz substrate (right).

The temperature-dependent spectral transmittance at normal incidence was measured by a Fourier-transform spectrometer (Thermo Scientific, Nicolet iS50) with extended spectrum from mid-infrared to near-infrared and visible range enabled by a white light source and a quartz beam splitter. A silicon detector was used for the wavelengths from 400 nm to 1 µm, while a DTGS detector captured the spectra at longer wavelengths from 1 to 2.5 µm, with each spectral measurement averaged over 32 scans at a resolution of 16 cm^{-1}. The sample was mounted on the cold finger inside a variable-temperature cryostat (Janis, VPF-800-FTIR) optically coupled through quartz windows with the spectrometer, and the sample temperature

was accurately controlled in a wide range from 77 K to 800 K by a temperature controller (Lakeshore 335) along with liquid nitrogen and a built-in heater. Throughout the measurement the cryostat chamber was maintained at a vacuum pressure less than 1×10^{-4} Torr.

Figure 35(a) shows the transmittance at room temperature when the VO_2 is insulating, and also at 100 °C when the VO_2 is metallic. Both the metallic and insulating VO_2 have 40-50% transmittance in the visible wavelengths, with the transmittance of the metallic phase 7% greater than the insulating phase. In the longer wavelengths, the fabricated VO_2 achieved a transmittance change of 57% at $\lambda = 2.5$ μm. This large change in near-infrared transmittance suggests that the furnace oxidized VO_2 would have considerable potential as a switching material for near-IR device applications. To investigate the nature of the insulator to metal phase transition of the furnace oxidized VO_2 sample, the heating and cooling curves were also measured. The in-situ temperature-dependent transmittance spectra were taken incrementally between room temperature and 370 K. After each set-point temperature was reached, 15 minutes were allotted for the sample temperature to stabilize at the set-point. Figure 35(b) shows the heating and cooling curves at a wavelength of $\lambda = 2.5$ μm for the VO_2 thin film fabricated on quartz. The heating curve shows a typical VO_2 transition temperature of 345 K, while the cooling curve shows a considerably lower transition temperature of 325 K, yielding a hysteresis of 20 K.
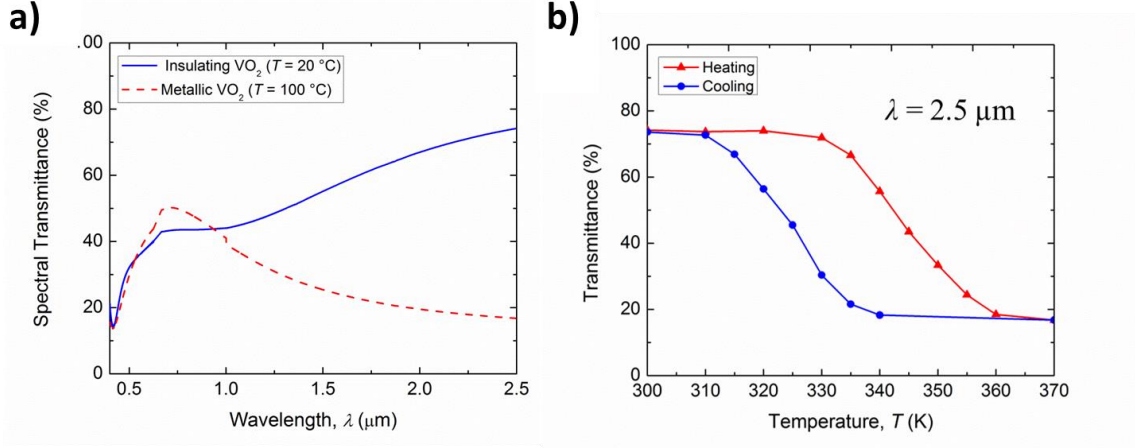
Figure 35. (a) Temperature-dependent spectral transmittance of the fabricated VO2 thin film on quartz in the visible and near-infrared wavelength ranges. (b) Heating and cooling transmittance curves for the fabricated VO2 at $\lambda = 2.5$ µm.

The dielectric constants for both the insulating and metallic VO$_2$ are fitted to a dispersion model [103] via a least-squares method by minimizing the objective function as:

$$F = \sum_{k=1}^{N} (T_{\text{exp}} - T_{\text{theo}})^2 \tag{47}$$

where T_{exp} is the experimentally measured transmittance data at each wavelength with index k and T_{theo} is the theoretical transmittance calculated by considering the sample as a thin film on an incoherent slab with ray-tracing optics [32], [87]:

$$T_{\text{theo}} = \frac{\tau_a \tau_s \tau}{1 - \rho_s \rho_b \tau^2} \tag{48}$$

where τ is the internal transmittance of the slab, τ_a is the transmittance from the air through the thin film layer, τ_s is the transmittance between the substrate and air below, ρ_s is the air-substrate reflectance, and ρ_b is the reflectance for the slab-air interface. τ_a and ρ_s are

91

determined from Fresnel's equations, while τ_s and ρ_b are determined from thin-film optics [87]. The optical properties of the quartz substrate are taken from Palik's Handbook [90], while the VO$_2$ optical properties are fitted to the Drude-Lorentz dispersion model [103], [119]:

$$\varepsilon(\omega) = \varepsilon_\infty - \frac{\omega_n^2}{\omega^2 + i\omega_c\omega} + \sum_{j=1}^{N} \frac{S_j}{1 - \omega^2/\omega_j^2 - i\gamma_j\,\omega/\omega_j} \tag{49}$$

where ε_∞ is the high-frequency dielectric constant, ω_n is the density parameter and ω_c is the collision frequency for free carriers. S_j, ω_j, and γ_j are respectively the high-frequency dielectric constant, phonon strength, phonon frequency, and damping coefficient for each oscillator. Four oscillators were used for the Lorentz term to achieve a satisfactory fit for both the metallic VO$_2$ and insulating VO$_2$. The least-squares parameter F was minimized according to ε_∞, ω_n, ω_c, ω_j, S_j, and γ_j using a genetic algorithm routine subject to bounds for each parameter. ε_∞ was constrained to be between -10 and 10, ω_n and ω_c were limited between 500 and 30000, and S_j and γ_j were set to be between 0 and 10. The phonon frequency was bounded between 500 and 30000 cm^{-1}.

The fitted parameters for both the insulating and metallic VO$_2$ are summarized in Table 6 and Table 7, respectively. Figure 36(a) and (b) show the comparison of the experimental data from optical measurements and the calculation results from the fitted model the spectral transmittance for wavelengths from 0.4 to 2.5 μm for the insulating and metallic phases, respectively, where excellent agreement is clearly seen. The real and imaginary parts of the dielectric constants calculated from the dispersion model are shown in Figure 36(c) and (d) for both insulating and metallic VO$_2$. Note that the optical properties

of fabricated VO_2 depend significantly on the fabrication method used, and hence the dielectric constants should be determined based on the optical spectroscopic measurements for accurate modeling to facilitate the design of novel optical devices based on VO_2 films fabricated using this simple furnace oxidation process.

Table 6. Fitting parameters for the dielectric constants of fabricated VO_2 film at the insulating phase in the visible/NIR range.

Insulating VO₂ Properties						
ε_∞	ω_c	ω_n	Oscillator Index j	S_j	ω_j	γ_j
5.16	27876	993	1	0.2711	25948	1.1436
			2	0.2946	23277	0.0787
			3	0.5720	16158	1.3605
			4	0.7577	27127	0.7264
			5	0.5052	29574	0.6017
			6	0.0065	7733	0.9867
			7	0.0189	24330	1.1995
			8	0.6293	8652	0.7314

Table 7. Fitting parameters for the dielectric constants of fabricated VO_2 film at the metallic phase in the visible/NIR range.

Metallic VO₂ Properties						
ε_∞	ω_c	ω_n	Oscillator Index j	S_j	ω_j	γ_j
5.08	7197	24410	1	0.06352	22043	0.6738
			2	0.82578	4639	0.8577
			3	0.75794	22149	0.2311
			4	0.09844	21208	1.8399
			5	0.85808	4715	0.4489
			6	1.63554	1634	1.7125
			7	0.20847	24103	0.3586
			8	1.16358	4292	1.0351
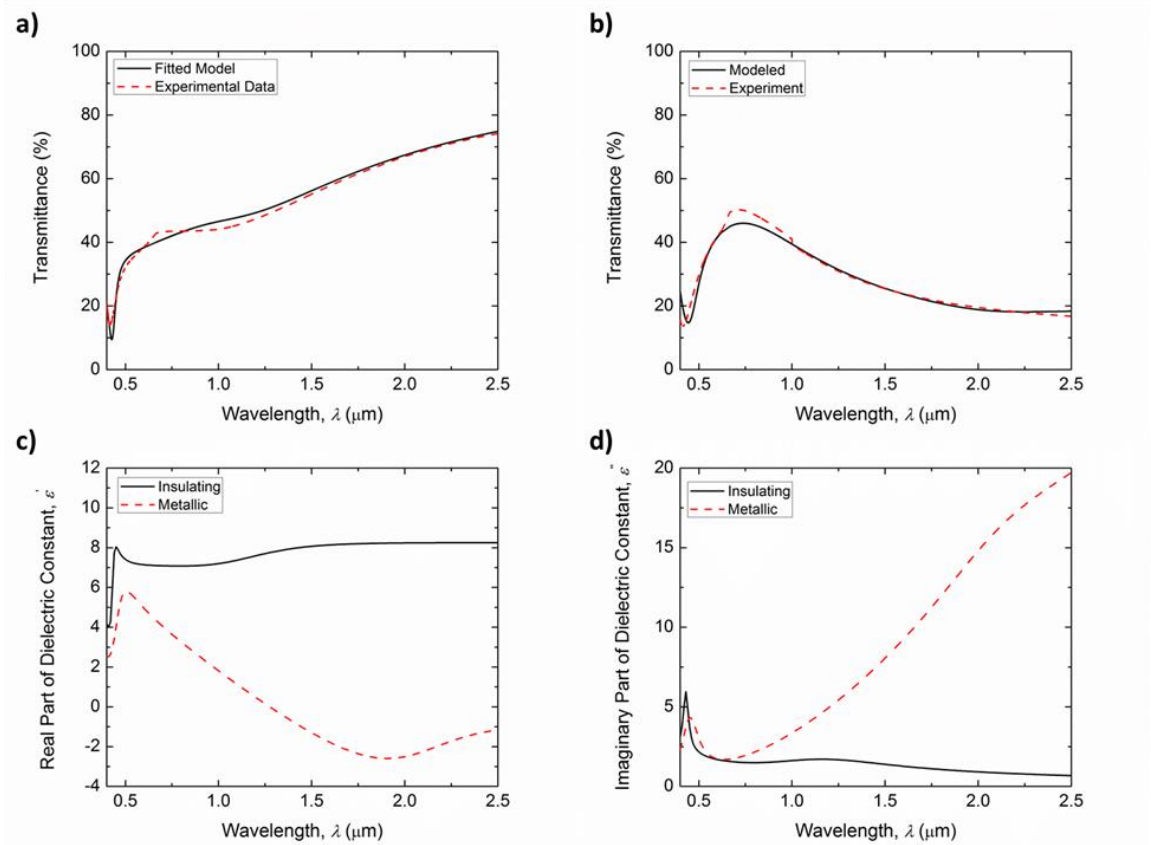
Figure 36. (a) Comparison between the fitted model (solid black) and the experimental data for insulating VO_2 (dashed red). (b) Comparison between the fitted model (black) and the experimental data for metallic VO_2 (dashed red). (c) Real part of the dielectric function for insulating and metallic VO_2. (d) Imaginary part of the dielectric function for insulating and metallic VO_2.

Though it has not been previously studied, the thermal stability of VO_2 films across a wide temperature range from cryogenic to high temperatures is of great interest for a number of applications, in particular for space applications like radiative thermal control and optical force modulation. The temperature-dependent spectral transmission provides a viable way to experimentally study the optical properties at different temperatures. First,

the behavior of the insulating VO_2 thin film on quartz sample at cryogenic temperatures was investigated with the custom cryostat coupled with the spectrometer using liquid nitrogen to cool the sample down to a minimum temperature of 77 K. With a built-in heater, the sample temperature was sequentially held at 77 K, 150 K, 250 K, and 300 K for 15 minutes at each temperature to ensure that the steady state was reached. Similarly, the VO_2 on quartz sample was heated beyond the phase transition at 373 K, 450 K, 550 K, 650 K and 750 K, where VO_2 is in the metallic phase, to inspect its high temperature behavior. Figure 37 shows the temperature-dependent spectral transmittance in wavelengths from 0.4 to 2.5 µm for cryogenic to high temperatures. As it can be seen, the spectral transmission for the insulating VO_2 changes little (less than 3% variation) from 77 K to 300 K within the visible and near-IR. The metallic phase behaves similarly, with little change in spectral transmission (less than 10%) at high temperatures from 737 K to 750 K. The results clearly demonstrate the excellent thermal stability of VO_2 thin films of both phases prepared from the furnace oxidation method, from cryogenic to high temperatures in vacuum conditions from visible to near-IR wavelengths. Note that there is a jump at a wavelength of 1 µm for the transmittance spectra at all temperatures. This is due to using different detectors above and below 1 µm, at which both detectors have low responsivity with relatively larger error (about 5%).

Given the significant property shift in the near-IR, and the excellent temperature stability, the furnace prepared VO_2 may have some potential as a tunable material for optical force modulation applications. In the next section, a preliminary design is proposed

95

and calculations are done for the performance with properties available from literature, and from the fitting procedure.
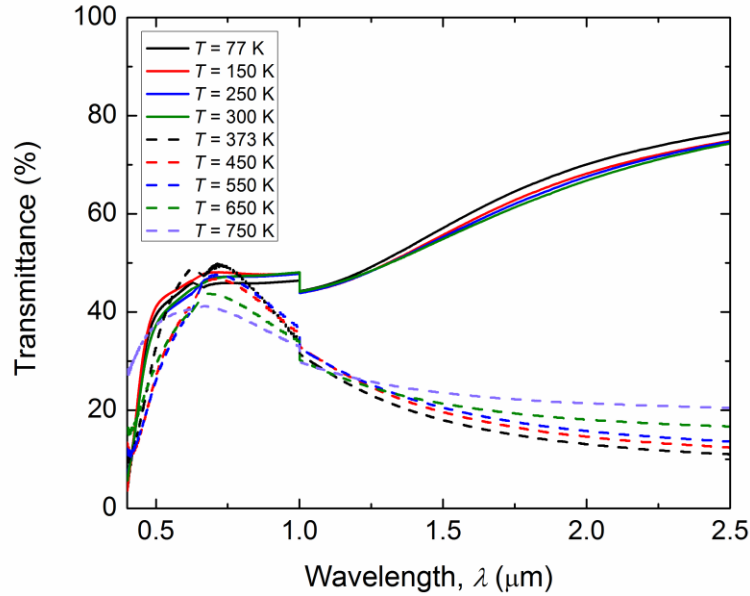
Figure 37. In-situ optical spectroscopic transmission measurements of 60-nm-thick VO_2 thin film on quartz substrate from cryogenic to high temperatures. Note that the VO_2 is in the insulating phase from 77 K to 300 K, and in the metallic phase from 373 K to 750 K.

6.2 Design of Optical Force Coating with Variable Reflectance

The objective with a VO_2-based solar radiation pressure modulation coating is to have high reflectivity in the "on" state and low reflectivity in the "off" state. Attitude control or steering can be realized using such a coating by placing the variable coating on the edges of the solar sail or spacecraft. If one edge has a high reflectivity while the other has a low reflectivity, then a torque is generated on the spacecraft, allowing the spacecraft

to adjust its orientation (Figure 38a). A Fabry-Perot resonance cavity with an anti-reflection layer is proposed to deliver thermochromic or electrochromic variable reflectivity over the solar spectrum. The Fabry-Perot resonator is composed of two mirrors, a gold thin film and a tungsten substrate, that are separated by a VO_2 spacer. At low temperatures, the Fabry-Perot cavity is formed because VO_2 is a relatively lossless spacer. At high temperatures (or an applied voltage), VO_2 is metallic and the entire structure is reflective, since all four layers are metallic. Figure 38(b) shows the overall high reflectance of the coating when the VO_2 is metallic (high reflectance), while Figure 38(c) shows the Fabry-Perot effect that is achieved with insulating VO_2.
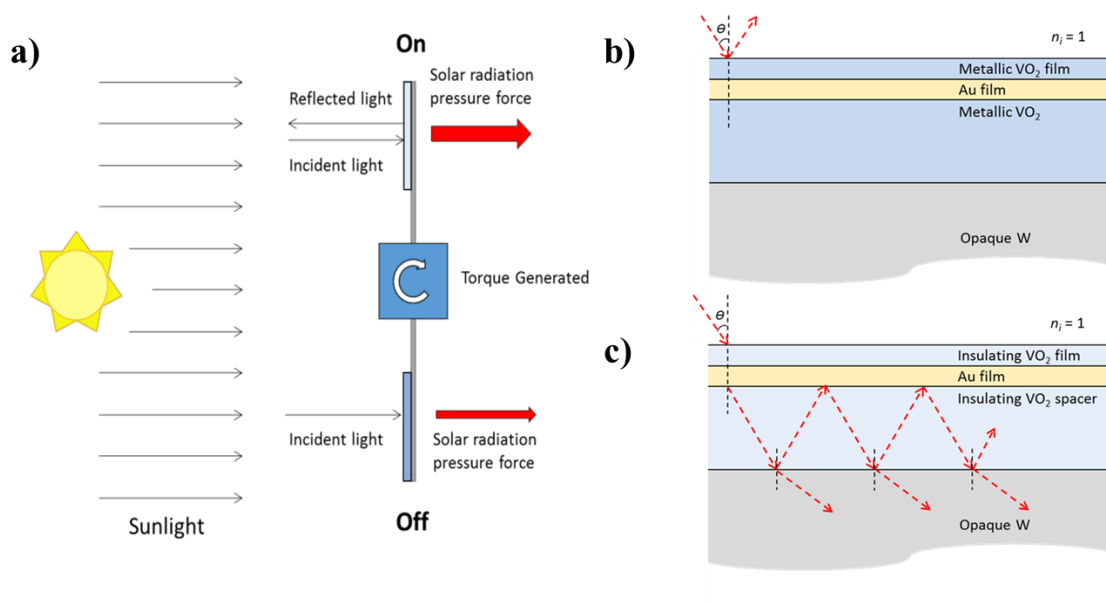
Figure 38. (a) Schematic for attitude control via variable reflectivity coatings. In the "on" state the coating is highly reflective and the incident solar radiation pressure is twice the magnitude of the "off" case where the coating is absorbing. Initial dynamic solar radiation pressure coating with (b) insulating VO_2 and (c) metallic VO_2.

The geometry, specifically the thin film layer thickness and the spacer thickness, of the Fabry-Perot cavity provides the spectral selectivity needed to modulate the radiative properties in the solar spectrum. The spacer thickness is chosen as the cavity thickness required to observe Fabry-Perot resonance in the visible wavelength regime. As with the variable emitter, a thinner spacer material will lead to smaller resonance wavelengths and likewise a larger spacer thickness will produce a larger resonance wavelength. The effect of the gold thin film in the structure is to determine the amplitude of the enhancement. A thinner, or less reflective thin film will yield a weaker enhancement. As the thickness is increased, a tradeoff must be found between the increased reflectivity of the interface and decreasing penetration depth, which decreases the strength of the enhancement.

The VO_2 properties used in this theoretical investigation are drawn from Barker et al. [84], as in Chapter 2. The insulating properties are calculated from the Drude model and the metallic properties are calculated from the Lorentz oscillator model. Similarly, the transitioning VO_2 properties are determined from the Bruggeman EMT using the depolarization factor q and volume fraction f published by Qazilbash et al. [39]. The uniaxial Bruggeman EMT expression presented in Chapter 2 is used to determine the effective dielectric constant of the composite medium of the transition VO_2. The temperature-dependent refractive index and extinction coefficient for both the ordinary and extraordinary cases are shown in Figure 39. In Ref [84], the dielectric constant was fit to measurements ranging from 500 nm to 100 µm, therefore the modeling efforts in this section focus on 500 nm to 4 µm. The upper limit, 4 µm is selected because it is the maximum wavelength that solar intensity data is publicly available for. A single epsilon

near pole phonon mode of VO2 is observed at 1 µm, which is characteristic of the Lorentz model used to calculate the insulating VO2 properties. As the temperature increases throughout the phase transition regime, the dramatic change in optical properties is evident. This shift in optical properties is seen across the entire wavelength spectrum considered and is the basis for the variable reflectance sought for radiation pressure modulation.
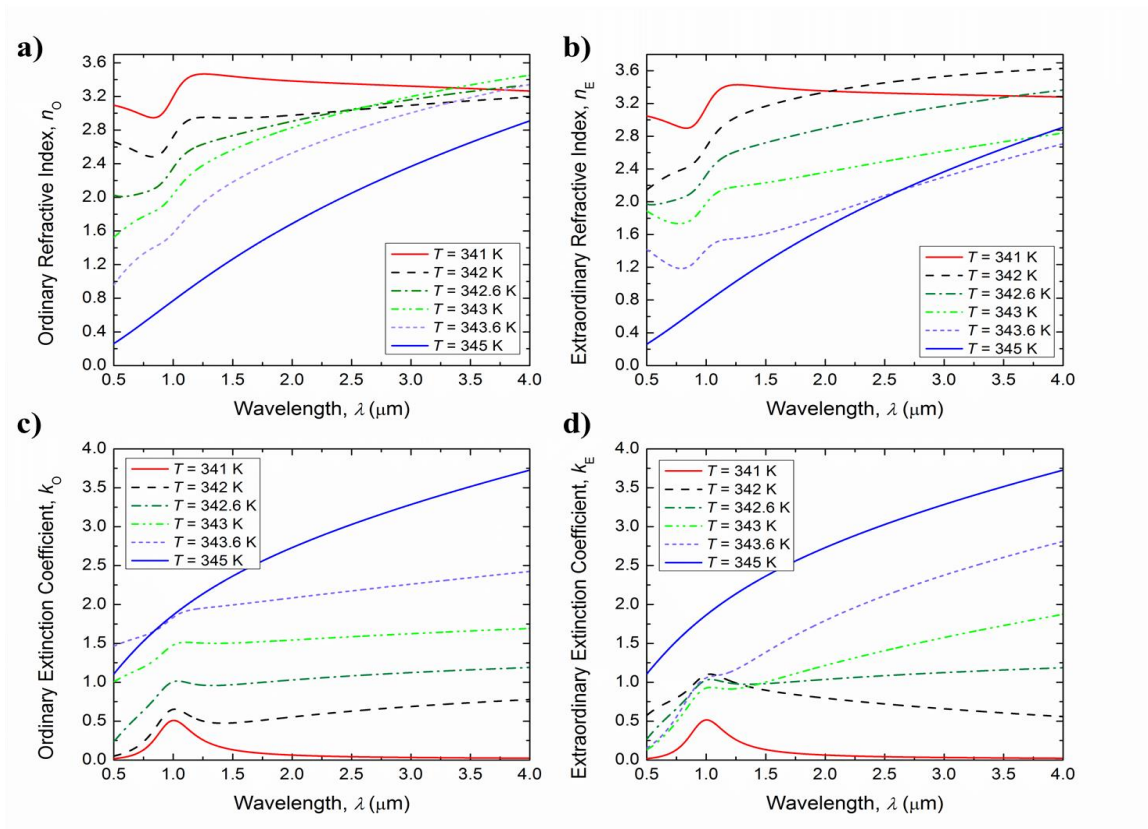
Figure 39. Temperature-dependent refractive index for (a) ordinary case and (b) extraordinary case. Extinction coefficient for the (c) ordinary case and (d) extraordinary case.

The temperature-dependent reflectance for the multilayer stack is calculated via the uniaxial transfer matrix method presented in Chapter 2. The layer thicknesses are optimized to be 30 nm, 15 nm, and 50 nm for the VO_2 antireflection coating, gold thin film, and VO_2 Fabry-Perot cavity spacer, respectively. The thickness of the tungsten substrate is chosen as 200 nm so that the tungsten is sufficiently opaque. The optical properties for the gold are calculated via a Drude model with constants from Palik's Handbook of Optical Constants [90]. The optical properties for tungsten are also taken as those measured in Ref. [90].

Figure 40(a) shows the spectral reflectance for the initial design, where the insulating VO_2 leads to low reflectance in the solar spectrum and the metallic VO_2 leads to high reflectance across all wavelengths considered. From the figure, it can be seen that the reflectance is over 85% for the entire wavelength spectrum considered when VO_2 is metallic. This high reflectance will yield high solar radiation pressure. Conversely, the reduced reflectance when the VO_2 is insulating will yield lower solar radiation pressure. For the visible wavelengths, the spectral reflectance is less than 20% and for near-infrared wavelengths between 0.8 and 1.6 µm, the spectral reflectance is less than the metallic case.
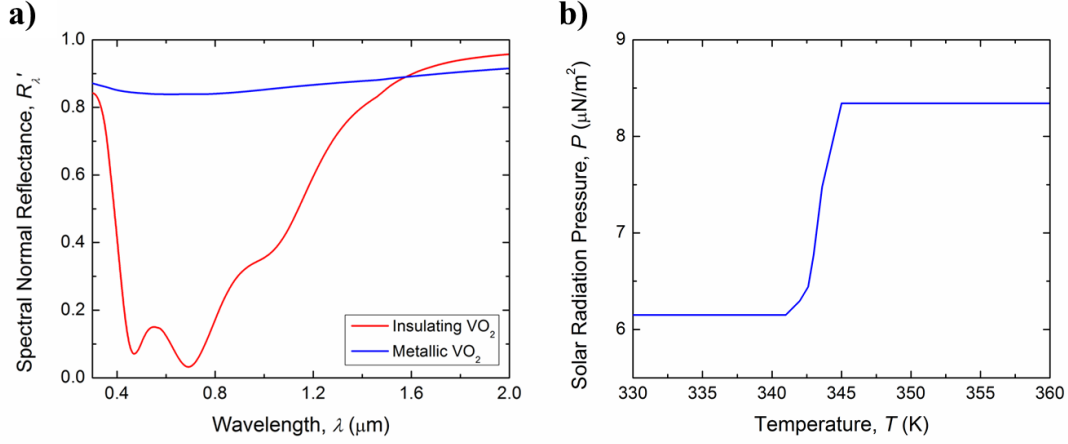
Figure 40. (a) Spectral normal reflectance for the variable reflector and (b) total radiation pressure variation with temperature.

After the spectral reflectance is determined, the solar radiation pressure P can be calculated from [32]:

$$P = \int_{0.5\mu m}^{4\mu m} I_{AM1.5}(2R(\lambda,0) + A(\lambda,0))d\lambda \tag{50}$$

Where R is the spectral normal reflectance of the proposed coating and $I_{AM1.5}$ is the extraterrestrial solar intensity where the spacecraft is assumed to be at the same distance from the Sun as the Earth. Since the proposed structure is opaque, the spectral normal absorptance, A_λ, can be calculated from $A_\lambda' = 1 - R_\lambda'$. The solar radiation pressure due to the reflectance is twice that from the absorbed photons, since the momentum transfer when is a photon is reflected is double that when it is simply absorbed. The maximum solar radiation pressure for a given structure naturally occurs when the reflectance is 1, whereas

the lowest solar radiation pressure for an opaque structure occurs when the reflectance is 0. Eq. 49 assumes that the solar intensity is normal to the coating surface.

For a perfectly reflective surface, the maximum solar radiation pressure that can be achieved is 9 μN/m^2, whereas a perfectly absorbing surface will yield a solar radiation pressure of 4.5 μN/m^2. Therefore, the maximum attainable radiation pressure modulation for an opaque surface is 4.5 μN/m^2. Figure 40(b) shows the solar radiation pressure for the proposed surface as the temperature is increased through the transition regime of VO_2. When the VO_2 is insulating, the solar radiation pressure is 6.1 μN/m^2, while the radiation pressure for metallic VO_2 is 8.4 μN/m^2, yielding a radiation pressure modulation of 2.3 μN/m^2. This is a little over half of the total possible radiation pressure. This result indicates that the proposed coating could be a good starting point for a multilayer variable reflectivity device based on the phase transition of VO_2. As with the variable emitter in Chapter 2, the angle-dependent spectral reflectance was also modeled and was likewise determined to be insensitive to incidence angle (Figure 41).
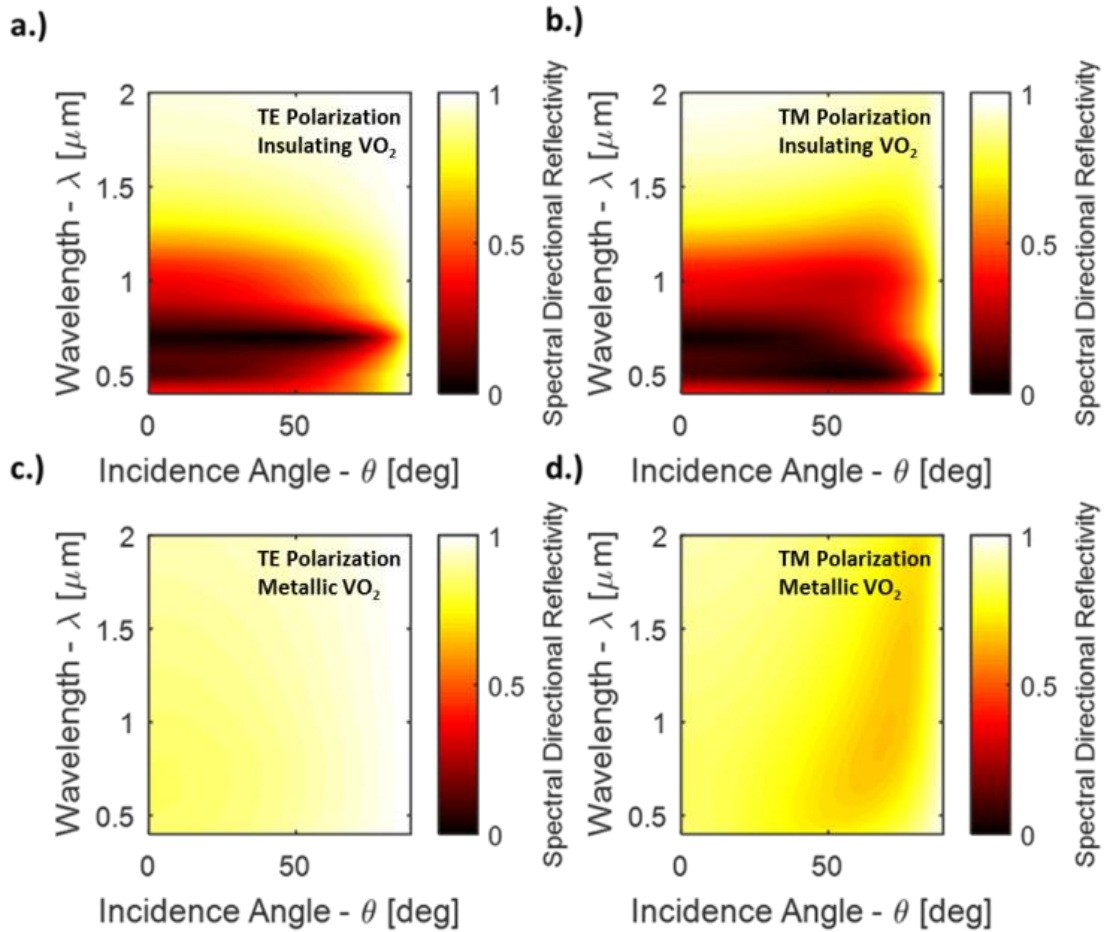
Figure 41. Spectral directional reflectance as a function of wavelength and incidence angle for (a) TE polarization and (b) TM polarization when VO₂ is insulating. Spectral directional reflectance as a function of wavelength and incidence angle for (c) TE polarization and (d) TM polarization when VO₂ is metallic. All four contour plots show that the performance of the proposed coating structure's performance has little dependence on incidence angle.

After the initial design and analysis using the properties found in [84], the performance for the variable reflector was calculated using the fitted properties from the furnace fabricated VO₂. From Figure 42 it is clear that the proposed variable reflectance

103

device based on furnace oxidized VO_2 will not significantly modulate the solar reflectance in the visible and NIR regimes, since the reflectance in both the insulating and metallic states is very similar. This is due to a much smaller change in optical properties in the visible and NIR wavelength regimes for the furnace fabricated VO_2. Other works have reported a similarly small change in the VO_2 properties below 1 µm in wavelength [103]. Although VO_2 does not exhibit good potential to be used a variable reflectance device for optical force modulation applications, there are several other transition materials that may offer a much larger change in solar radiation pressure upon transition.
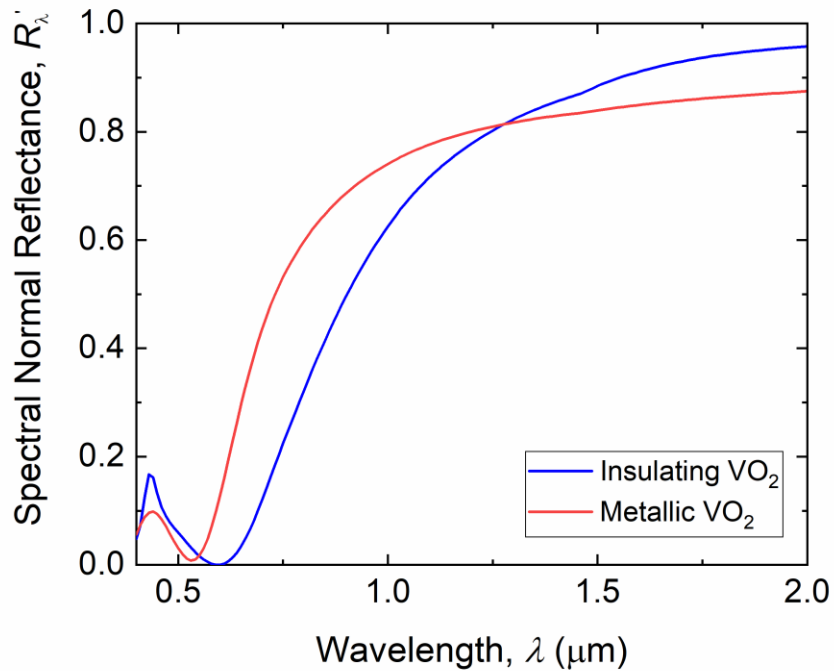
Figure 42. Calculated spectral normal reflectance for the proposed variable reflectance coating with insulating VO_2 (blue) and metallic VO_2 (red).

CHAPTER 7 CONCLUSIONS AND FUTURE WORK

The primary objective of this dissertation was to design, fabricate, and experimentally demonstrate a VO_2-based variable emittance coating for dynamic thermal management applications. In Chapter 2, the theoretical design and analysis of a VO_2 variable emitter was discussed. To aid in the design of a VO_2-based variable emitter, uniaxial expressions of the transfer matrix method and Bruggeman effective medium theory were introduced. The uniaxial properties of the VO_2 in the insulating, transition, and metallic states were presented and the VO_2 phonon modes were discussed. The physical mechanism, Fabry-Perot resonance, was illustrated and shown to be responsible for the observed emittance enhancement. Lastly, the thermal performance of the proposed emitter was determined for both extraterrestrial and terrestrial radiative cooling applications. With an approximately 0.40 change in emittance, the VO_2-based emitter showed good potential for use in dynamic radiative cooling applications. Future work on the emitter design could focus on reducing the solar absorptance via selective photonic crystal or nanoparticle solar reflectors.

In Chapter 3, a furnace oxidation technique was developed to fabricate stoichiometric VO_2 thin films that displayed a high degree of thermochromism. A parametric study was undertaken to determine the optimum temperature, O_2 and N_2 flow rates, and oxidation time. The fabricated films were characterized and the optical properties were fitted to better predict the performance of devices fabricated using the new fabrication technique. The nature of the VO_2 hysteresis, including the hysteresis under partial transition, was explored. Likewise, the thermal stability and thermal cycling durability

were assessed for the VO$_2$ thin films. To further this research for variable emittance thermal control applications, the transition temperature of the variable emitter must be reduced significantly. As discussed in this dissertation, several methods exist to reduce the transition temperature, including doping, defect engineering, and process controls. Using the furnace oxidation method discussed in this dissertation, I plan to develop a co-sputtering recipe for vanadium metal and tungsten to produce tungsten-doped vanadium precursor films. These will then be oxidized with the goal of fabricating tungsten doped vanadium dioxide with a substantially reduced transition temperature. These films will then be characterized with temperature-dependent FTIR spectroscopy and an optical property model will be developed.

Next, a VO$_2$ FP emitter was fabricated, characterized and experimentally demonstrated in Chapter 4. First the temperature-dependent radiative properties of the emitter were measured using FTIR spectroscopy. Then the variable heat rejection was demonstrated via two calorimetry-based thermal measurements, one simulating ambient temperature applications and the other simulating a "space-like" environment with a cryogenic radiative sink. In both cases, the temperature-dependent variable heat rejection of the fabricated emitter was demonstrated. The experimental and theoretical performance of the fabricated emitter were in good agreement, and the difference was less than the uncertainty for this experiment. Currently I am assessing the hysteresis behavior of the VO$_2$ FP emitter under partial heating using the cryothermal measurement technique developed in this dissertation. Future work will include transient analyses of the variable emitter performance, and assessments of emitters with reduced transition temperature.

In Chapter 5, the theoretical modeling of a representative human spacecraft mission revealed the target temperature and minimum required emittance changed for human spaceflight applications. This information can serve as a guide for both my work to reduce the transition temperature, and for future researchers working on human spaceflight thermal control. Future work will include the transient systems modeling of VO_2-based variable emitters, in particular the effect of the hysteresis behavior on the temperature control of the spacecraft. Additionally, future work should include similar studies for robotic spacecraft missions.

Another recommendation is to conduct degradation studies on both VO_2 thin films and the proposed Fabry-Perot emitter coating. Especially in the space environment, there are several effects which can cause considerable degradation of thermal control coatings, including atomic oxygen, UV exposure, solar wind irradiation, and contamination. Additionally, for missions far beyond Earth, a typical requirement is that the coating be electrically dissipative. Future studies should also assess the electrical dissipation capability of VO_2-based coatings, as well as the potential to add an electrically conductive overlayer like indium tin oxide (ITO). Another useful study would be to coat the proposed multilayer variable emittance coating on flexible substrates such as Teflon, mylar, etc. that are commonly used in both the spacecraft industry and residential energy saving applications. While there are several challenges remaining, the design, analysis, fabrication, and experimental demonstration of the variable emitter proposed in this dissertation illustrates the potential for VO_2 variable emitters to be useful for thermal control applications. Furthermore, the VO_2 hysteresis behavior that has been presented in

this dissertation work provides some useful insight for how VO_2-based coatings may function in transient systems. Finally, the thermal stability and thermal cycling assessments conducted in this dissertation support the use of VO_2 as a suitable material for spacecraft thermal control applications.

A secondary objective of this dissertation research was to assess the potential for VO_2 to be used to modulate optical force (Chapter 6). Although VO_2 did not display good potential for being used in this application, there are several other materials that could be used in optical force modulation coatings, including tungsten trioxide (WO_3), niobium pentoxide (Nb_2O_5), and liquid crystals, which all exhibit electrochromic optical property shifts in the solar spectrum. Future studies could also focus on proposed coatings that switch between specular reflectance and transmittance, rather than absorptance and reflectance as proposed in this dissertation. Finally, the extraction of the visible and NIR properties for the furnace fabricated VO_2 could be useful to predict the performance in the visible and NIR for any applications involving furnace fabricated VO_2, such as smart window performance, solar absorptance of radiator coatings, and high temperature thermal emitters.

The following is a list of journal publications and conference presentations during the PhD study:

First-Author Journal Publications (Dissertation-Related)

1. **Taylor, S.**, Boman, N., Chao, J., and Wang, L.P., "Cryothermal Vacuum Measurement of Thermochromic Variable Emissivity Coatings for Spacecraft Thermal Management," in preparation.
2. **Taylor, S.**, Long, L., McBurney, R., Sabbaghi, P., Chao, J., and Wang, L.P., 2020, "Spectrally-Selective Vanadium Dioxide Based Tunable Metafilm Emitter for Dynamic Radiative Cooling," Solar Energy Materials and Solar Cells, 217, 110739.
3. **Taylor, S.**, Chao, J., Long, L.S., Vlastos, N., and Wang, L.P., 2019, "Temperature-Dependent Optical Property Characterization of VO_2 Thin Film Prepared from Furnace Oxidation Method," ES Manufacturing and Materials, 6, 62-67.
4. **Taylor, S.**, Long, L., and Wang, L.P., 2019, "Fabrication and characterization of furnace oxidized VO_2 thin films," Thin Solid Films, 682, 29-36.
5. **Taylor, S.**, Yang, Y., and Wang, L.P, 2017, "Vanadium Dioxide-Based Fabry-Perot Emitter for Dynamic Radiative Cooling Applications," Journal of Quantitative Spectroscopy and Radiative Transfer, 197, 76-83.

Co-Author Publications (Non-Dissertation-Related)

1. Alshehri, H., **Taylor, S.**, and Wang, L.P., "Selective Color Absorber Made of Aluminum Nanodisk Arrays by Exciting Magnetic Polariton," to be submitted.
2. Chang, J.-Y., **Taylor, S.**, McBurney, R., Ying, X.Y., Allu, G., Chen, Y.-B., and Wang, L.P., "Enhancing Solar Thermal Energy Conversion with Wavelength-Selective Silicon-Cored Tungsten Nanowire Metamaterial Absorbers," under review.
3. Long, L., **Taylor, S.**, and Wang, L.P., 2020, "Enhanced Infrared Emission by Thermally Switching the Excitation of Magnetic Polariton with Scalable Microstructured VO_2 Metasurfaces," ACS Photonics, 7, 2219-2227.
4. Sabbaghi, P., Long, L., Ying, X., Lambert, L., **Taylor, S.**, Messner, C., and Wang, L.P., 2020, "Super-Planckian radiative heat transfer between macroscale surfaces due to near-field and thin-film effects," Journal of Applied Physics, 128, 025305.
5. Alshehri, H., Ni, Q., **Taylor, S.**, McBurney, R., and Wang, H., 2020, "High-Temperature Solar Thermal Energy Conversion Enhanced by Spectrally-Selective Metafilm Absorber under Concentrated Solar Irradiation," ES Energy & Environment, accepted.
6. Long, L., **Taylor, S.**, Ying, X., and Wang, L.P., 2019, "Thermally-switchable spectrally-selective infrared metamaterial absorber/emitter by tuning magnetic polariton with a phase-change VO2 layer," Materials Today Energy, 13, 214-220.
7. Yang, Y., **Taylor, S.**, and Wang, L.P., 2017, "Wavelength-selective and diffuse infrared thermal emission mediated by magnetic polaritons from silicon carbide metasurfaces," Applied Physics Letters, 111, 051904.

Conference Presentations:

1. **Taylor, S.**, Hernandez, Z., and Iovine, J., 2020, "Model Validation for Bigelow Expandable Activities Module (BEAM) with Stowage," Thermal and Fluids Analysis Workshop (TFAWS), Oral Presentation, Abstract TFAWS20-PT309, Jet Propulsion Lab, August 18-20.

2. **Taylor, S.**, Boman, N., Chao, J., and Wang, L.P., 2019, "Cryothermal Vacuum Measurement of Thermochromic Variable Emissivity Coatings for Spacecraft Thermal Management," ASME International Mechanical Engineering Congress and Exposition (IMECE), Oral Presentation, Abstract No. IMECE2019-12558, Salt Lake City, UT, November 10-14.

3. **Taylor, S.**, Boman, N., Chao, J., and Wang, L.P., 2019, "Cryothermal Vacuum Measurement of Thermochromic Variable Emissivity Coatings for Spacecraft Thermal Management," ASME International Mechanical Engineering Congress and Exposition (IMECE), Poster Presentation, Abstract No. IMECE2019-12551, Salt Lake City, UT, November 10-14.

4. **Taylor, S.**, and Wang, L.P., 2019, "Thermal Vacuum Testing and Feasibility Investigations for VO2-Based Variable Emittance Coatings," NASA 2019 Thermal and Fluids Analysis Workshop (TFAWS), Oral Presentation, Abstract TFAWS-PT-13, NASA Langley Research Center, Hampton, VA, August 26-30.

5. **Taylor, S.**, Long, L., and Wang, L.P., 2019, "Tunable Metafilms and Metasurfaces Based on Thermochromic VO2 for Dynamic Control of Infrared Thermal Emission," MRS Spring Meeting, Poster Presentation, Abstract No. 3121976, Phoenix, AZ, April 22-26.

6. **Taylor, S.**, and Wang, L.P., 2018, "Thermochromic VO_2-Based Variable Emittance Coatings for Spacecraft Thermal Control," ASME 2018 International Mechanical Engineering Congress and Exposition (IMECE), Poster Presentation, Abstract No. IMECE2018-89217, Pittsburgh, PA, November 9-15.

7. **Taylor, S.**, and Wang, L.P., 2018, "Thermochromic VO_2-Based Variable Emittance Coatings for Spacecraft Thermal Control," ASME 2018 International Mechanical Engineering Congress and Exposition (IMECE), Oral Presentation, Abstract No. IMECE2018-89215, Pittsburgh, PA, November 9-15.

8. **Taylor, S.**, Massina, C.J., and Wang, L.P., 2018, "Thermal Systems Modeling of a Variable Emittance Coating for Human Spacecraft Applications," NASA 2018 Thermal and Fluids Analysis Workshop (TFAWS), Oral Presentation, Abstract TFAWS-PT-10, Houston, TX, August 20-24.

9. **Taylor, S.** and Wang, L.P., 2018, "Fabrication and Characterization of Fabry-Perot Based Variable Emissivity Coatings for Passive Thermal Control," 48th International Conference on Environmental Systems (ICES), Poster Presentation, Student Poster Competition, Albuquerque, NM, July 8-12.

10. **Taylor, S.** and Wang, L.P., 2017, "Thermochromic Variable Emittance Radiation Coatings for Spacecraft Thermal Management," NASA 2017 Thermal and Fluids Analysis Workshop, Oral Presentation, Abstract TFAWS2017-PT03, Huntsville, AL, August 21-25.

11. **Taylor, S.**, Wang, H., Hanson, J., Feinglass, J., and Wang, L.P., 2016, "Cryogenic to High Temperature Spectrometric Platform for Characterizing Temperature Dependent Radiative Properties," ASME 2016 International Mechanical Engineering Congress and Exposition (IMECE), Oral Presentation, Abstract No. IMECE2016-66435, Phoenix, AZ, November 11-17.
12. **Taylor, S.** and Wang, L.P., 2016, "Vanadium Dioxide-Based Variable Reflectivity Radiation Coatings for Optical Propulsion Applications," 67th International Astronautical Congress, Oral Presentation, Guadalajara, Mexico, September 26-30.
13. **Taylor, S.**, Yang, Y., and Wang, L.P., 2016, "Tunable Vanadium Dioxide Based Fabry-Perot Emitter for Dynamic Radiative Cooling Applications," 8th International Symposium on Radiative Transfer (RAD16), Cappadocia, Turkey, June 6-10.
14. **Taylor, S.** and Wang, L.P., 2016, "Dynamic Radiative Thermal Management with Switchable Vanadium Dioxide Based Fabry-Perot Thermal Emitters," 2016 MRS Spring Meeting, Poster Presentation, Abstract No. 2411925, Phoenix, AZ, March 28 - April 1.

REFERENCES

[1]   P. O. Wieland, "Designing for human presence in space: an introduction to environmental control and life support systems (ECLSS)," 2005.

[2]   T. D. Swanson and G. C. Birur, "NASA thermal control technologies for robotic spacecraft," *Appl. Therm. Eng.*, vol. 23, no. 9, pp. 1055–1065, 2003.

[3]   J. L. Champion, R. Osiander, M. A. Darrin, and T. D. Swanson, "MEMS louvers for thermal control," 1998.

[4]   R. B. Mulford, M. R. Jones, and B. D. Iverson, "Dynamic control of radiative surface properties with origami-inspired design," *J. Heat Transfer*, vol. 138, no. 3, 2016.

[5]   C. L. Bertagne, T. J. Cognata, R. B. Sheth, C. E. Dinsmore, and D. J. Hartl, "Testing and analysis of a morphing radiator concept for thermal control of crewed space vehicles," *Appl. Therm. Eng.*, vol. 124, pp. 986–1002, 2017.

[6]   F. Lang, H. Wang, S. Zhang, J. Liu, and H. Yan, "Review on variable emissivity materials and devices based on smart chromism," *Int. J. Thermophys.*, vol. 39, no. 1, p. 6, 2018.

[7]   H. Demiryont and D. Moorehead, "Electrochromic emissivity modulator for spacecraft thermal management," *Sol. Energy Mater. Sol. Cells*, vol. 93, no. 12, pp. 2075–2078, 2009.

[8]   M. Soltani, M. Chaker, E. Haddad, and R. Kruzelecky, "Thermochromic vanadium dioxide (VO 2) smart coatings for switching applications," *Transw. Res. Netw.*, vol. 37661, no. 2, pp. 978–81, 2008.

[9]   B. E. D. Book, "Energy efficiency and renewable energy," *US Dep. energy*, 2011.

[10]   E. Rephaeli, A. Raman, and S. Fan, "Ultrabroadband photonic structures to achieve high-performance daytime radiative cooling," *Nano Lett.*, vol. 13, no. 4, pp. 1457–1461, 2013.

[11]   A. P. Raman, M. A. Anoma, L. Zhu, E. Rephaeli, and S. Fan, "Passive radiative cooling below ambient air temperature under direct sunlight," *Nature*, vol. 515, no. 7528, pp. 540–544, 2014, doi: 10.1038/nature13883.

[12]   L. Zhu, A. P. Raman, and S. Fan, "Radiative cooling of solar absorbers using a visibly transparent photonic crystal thermal blackbody," *Proc. Natl. Acad. Sci. U. S. A.*, vol. 112, no. 40, pp. 12282–12287, 2015, doi: 10.1073/pnas.1509453112.

[13]   S. Fan, "Thermal photonics and energy applications," *Joule*, vol. 1, no. 2, pp. 264–273, 2017.

[14]   L. Zhu, A. Raman, and S. Fan, "Color-preserving daytime radiative cooling,"

Appl. Phys. Lett., vol. 103, no. 22, p. 223902, 2013.

[15]   H. Ye, H. Wang, and Q. Cai, "Two-dimensional VO2 photonic crystal selective emitter," *J. Quant. Spectrosc. Radiat. Transf.*, vol. 158, pp. 119–126, 2015, doi: 10.1016/j.jqsrt.2015.01.022.

[16]   P. Nagpal, S. E. Han, A. Stein, and D. J. Norris, "Efficient low-temperature thermophotovoltaic emitters from metallic photonic crystals," *Nano Lett.*, vol. 8, no. 10, pp. 3238–3243, 2008, doi: 10.1021/nl801571z.

[17]   A. Narayanaswamy and G. Chen, "Thermal emission control with one-dimensional metallodielectric photonic crystals," *Phys. Rev. B - Condens. Matter Mater. Phys.*, vol. 70, no. 12, pp. 1–4, 2004, doi: 10.1103/PhysRevB.70.125101.

[18]   I. Celanovic, D. Perreault, and J. Kassakian, "Resonant-cavity enhanced thermal emission," *Phys. Rev. B - Condens. Matter Mater. Phys.*, vol. 72, no. 7, pp. 2–7, 2005, doi: 10.1103/PhysRevB.72.075127.

[19]   S. Shu, Z. Li, and Y. Y. Li, "Triple-layer Fabry-Perot absorber with near-perfect absorption in visible and near-infrared regime," *Opt. Express*, vol. 21, no. 21, p. 25307, 2013, doi: 10.1364/oe.21.025307.

[20]   J. Kou, Z. Jurado, Z. Chen, S. Fan, and A. J. Minnich, "Daytime radiative cooling using near-black infrared emitters," *Acs Photonics*, vol. 4, no. 3, pp. 626–630, 2017.

[21]   Z. Huang and X. Ruan, "Nanoparticle embedded double-layer coating for daytime radiative cooling," *Int. J. Heat Mass Transf.*, vol. 104, pp. 890–896, 2017.

[22]   M. M. Hossain, B. Jia, and M. Gu, "A metamaterial emitter for highly efficient radiative cooling," *Adv. Opt. Mater.*, vol. 3, no. 8, pp. 1047–1051, 2015.

[23]   X. Liu, T. Tyler, T. Starr, A. F. Starr, N. M. Jokerst, and W. J. Padilla, "Taming the blackbody with infrared metamaterials as selective thermal emitters," *Phys. Rev. Lett.*, vol. 107, no. 4, pp. 4–7, 2011, doi: 10.1103/PhysRevLett.107.045901.

[24]   Y. Zhai *et al.*, "Scalable-manufactured randomized glass-polymer hybrid metamaterial for daytime radiative cooling," *Science (80-.).*, vol. 355, no. 6329, pp. 1062–1066, 2017.

[25]   S. Wang, M. Liu, L. Kong, Y. Long, X. Jiang, and A. Yu, "Recent progress in VO2 smart coatings: Strategies to improve the thermochromic properties," *Prog. Mater. Sci.*, vol. 81, pp. 1–54, 2016, doi: 10.1016/j.pmatsci.2016.03.001.

[26]   D. Fan, Q. Li, Y. Xuan, and Y. Xia, "Thermal radiation from silicon microcavity coated with thermochromic film," *Sol. Energy Mater. Sol. Cells*, vol. 144, pp. 331–338, 2016.

[27] L. Johnson, R. M. Young, and E. E. Montgomery Iv, "Recent advances in solar sail propulsion systems at NASA," *Acta Astronaut.*, vol. 61, no. 1–6, pp. 376–382, 2007.

[28] B. Wie, "Solar sail attitude control and dynamics, part 1," *J. Guid. Control. Dyn.*, vol. 27, no. 4, pp. 526–535, 2004.

[29] K. D. Kumar, H. C. Bang, and M.-J. Tahk, "New attitude control approach for satellites in elliptic orbits using solar radiation pressure," *Acta Astronaut.*, vol. 59, no. 6, pp. 462–473, 2006.

[30] Y. Tsuda *et al.*, "Flight status of IKAROS deep space solar sail demonstrator," *Acta Astronaut.*, vol. 69, no. 9–10, pp. 833–840, 2011.

[31] Y. Tsuda *et al.*, "Achievement of IKAROS—Japanese deep space solar sail demonstration mission," *Acta Astronaut.*, vol. 82, no. 2, pp. 183–188, 2013.

[32] M. F. Modest, *Radiative heat transfer*. Academic press, 2013.

[33] E. Mettler, A. Acikmese, and S. Ploen, "Attitude dynamics and control of solar sails with articulated vanes," in *AIAA Guidance, Navigation, and Control Conference and Exhibit*, 2005, p. 6081.

[34] B. Fu and F. O. Eke, "Attitude control methodology for large solar sails," *J. Guid. Control. Dyn.*, vol. 38, no. 4, pp. 662–670, 2015.

[35] T. R. Patel, K. D. Kumar, and K. Behdinan, "Variable structure control for satellite attitude stabilization in elliptic orbits using solar radiation pressure," *Acta Astronaut.*, vol. 64, no. 2–3, pp. 359–373, 2009.

[36] R. Funase *et al.*, "On-orbit verification of fuel-free attitude control system for spinning solar sail utilizing solar radiation pressure," *Adv. Sp. Res.*, vol. 48, no. 11, pp. 1740–1746, 2011.

[37] A. Borggräfe, J. Heiligers, M. Ceriotti, and C. R. McInnes, "Distributed reflectivity solar sails for extended mission applications," in *Advances in Solar Sailing*, Springer, 2014, pp. 331–350.

[38] C. Colombo, C. Lücking, and C. R. McInnes, "Orbit evolution, maintenance and disposal of SpaceChip swarms through electro-chromic control," *Acta Astronaut.*, vol. 82, no. 1, pp. 25–37, 2013.

[39] M. M. Qazilbash *et al.*, "Mott transition in VO2 revealed by infrared spectroscopy and nano-imaging," *Science (80-.).*, vol. 318, no. 5857, pp. 1750–1753, 2007.

[40] S. Y. Li, G. A. Niklasson, and C. G. Granqvist, "Nanothermochromics: Calculations for VO2 nanoparticles in dielectric hosts show much improved luminous transmittance and solar energy transmittance modulation," *J. Appl.*

Phys., vol. 108, no. 6, 2010, doi: 10.1063/1.3487980.

[41] M. Li, H. Wu, L. Zhong, H. Wang, Y. Luo, and G. Li, "Active and dynamic infrared switching of VO 2 (M) nanoparticle film on ITO glass," *J. Mater. Chem. C*, vol. 4, no. 8, pp. 1579–1583, 2016.

[42] Y. Gao *et al.*, "VO 2--Sb: SnO 2 composite thermochromic smart glass foil," *Energy Environ. Sci.*, vol. 5, no. 8, pp. 8234–8237, 2012.

[43] H. Ye *et al.*, "The demonstration and simulation of the application performance of the vanadium dioxide single glazing," *Sol. Energy Mater. Sol. Cells*, vol. 117, pp. 168–173, 2013, doi: 10.1016/j.solmat.2013.05.061.

[44] M. J. Powell *et al.*, "Intelligent multifunctional VO2/SiO2/TiO2 coatings for self-cleaning, energy-saving window panels," *Chem. Mater.*, vol. 28, no. 5, pp. 1369–1376, 2016.

[45] J. Zhang *et al.*, "Mesoporous SiO2/VO2 double-layer thermochromic coating with improved visible transmittance for smart window," *Sol. Energy Mater. Sol. Cells*, vol. 162, pp. 134–141, 2017.

[46] S.-Y. Li, G. A. Niklasson, and C. G. Granqvist, "Thermochromic undoped and Mg-doped VO2 thin films and nanoparticles: Optical properties and performance limits for energy efficient windows," *J. Appl. Phys.*, vol. 115, no. 5, p. 53513, 2014.

[47] F. Xu, X. Cao, H. Luo, and P. Jin, "Recent advances in VO 2-based thermochromic composites for smart windows," *J. Mater. Chem. C*, vol. 6, no. 8, pp. 1903–1919, 2018.

[48] L. Dai *et al.*, "F-doped VO 2 nanoparticles for thermochromic energy-saving foils with modified color and enhanced solar-heat shielding ability," *Phys. Chem. Chem. Phys.*, vol. 15, no. 28, pp. 11723–11729, 2013.

[49] H. Wang, Y. Yang, and L. Wang, "Switchable wavelength-selective and diffuse metamaterial absorber/emitter with a phase transition spacer layer," *Appl. Phys. Lett.*, vol. 105, no. 7, 2014, doi: 10.1063/1.4893616.

[50] H. Wang, Y. Yang, and L. Wang, "Wavelength-tunable infrared metamaterial by tailoring magnetic resonance condition with VO2phase transition," *J. Appl. Phys.*, vol. 116, no. 12, pp. 1–5, 2014, doi: 10.1063/1.4896525.

[51] M. Benkahoul *et al.*, "Thermochromic VO2 film deposited on Al with tunable thermal emissivity for space applications," *Sol. Energy Mater. Sol. Cells*, vol. 95, no. 12, pp. 3504–3508, 2011, doi: 10.1016/j.solmat.2011.08.014.

[52] Y. Yang, S. Basu, and L. Wang, "Radiation-based near-field thermal rectification with phase transition materials," *Appl. Phys. Lett.*, vol. 103, no. 16, p. 163101,

2013.

[53] K. Ito, K. Nishikawa, H. Iizuka, and H. Toshiyoshi, "Experimental investigation of radiative thermal rectifier using vanadium dioxide," *Appl. Phys. Lett.*, vol. 105, no. 25, p. 253503, 2014.

[54] A. Ghanekar, G. Xiao, and Y. Zheng, "High contrast far-field radiative thermal diode," *Sci. Rep.*, vol. 7, no. 1, pp. 1–7, 2017.

[55] J. Zheng, S. Bao, and P. Jin, "TiO2 (R)/VO2 (M)/TiO2 (A) multilayer film as smart window: Combination of energy-saving, antifogging and self-cleaning functions," *Nano Energy*, vol. 11, pp. 136–145, 2015.

[56] R. L. Voti, M. C. Larciprete, G. Leahu, C. Sibilia, and M. Bertolotti, "Optimization of thermochromic VO2 based structures with tunable thermal emissivity," *J. Appl. Phys.*, vol. 112, no. 3, p. 34305, 2012.

[57] J. Rensberg *et al.*, "Active optical metasurfaces based on defect-engineered phase-transition materials," *Nano Lett.*, vol. 16, no. 2, pp. 1050–1055, 2016.

[58] L. Long, S. Taylor, X. Ying, and L. Wang, "Thermally-switchable spectrally-selective infrared metamaterial absorber/emitter by tuning magnetic polariton with a phase-change VO2 layer," *Mater. Today Energy*, vol. 13, pp. 214–220, 2019.

[59] M. Nakano *et al.*, "Infrared-sensitive electrochromic device based on VO2," *Appl. Phys. Lett.*, vol. 103, no. 15, p. 153503, 2013.

[60] E. Gagaoudakis *et al.*, "Low-temperature rf sputtered VO2 thin films as thermochromic coatings for smart glazing systems," *Sol. Energy*, vol. 165, pp. 115–121, 2018.

[61] H. Asayesh-Ardakani *et al.*, "Direct evidence of M2 phase during the monoclinic-tetragonal (rutile) phase transition of W-doped VO2 nanowires," *Appl. Phys. Lett.*, vol. 110, no. 5, p. 53107, 2017.

[62] P. Jin and S. Tanemura, "Formation and thermochromism of VO2 films deposited by RF magnetron sputtering at low substrate temperature," *Jpn. J. Appl. Phys.*, vol. 33, no. 3R, p. 1478, 1994.

[63] M. Taha *et al.*, "Insulator--metal transition in substrate-independent VO 2 thin film for phase-change devices," *Sci. Rep.*, vol. 7, no. 1, pp. 1–10, 2017.

[64] S.-Y. Li, K. Namura, M. Suzuki, G. A. Niklasson, and C. G. Granqvist, "Thermochromic VO2 nanorods made by sputter deposition: Growth conditions and optical modeling," *J. Appl. Phys.*, vol. 114, no. 3, p. 33516, 2013.

[65] Y.-K. Dou *et al.*, "Oxidizing annealing effects on VO2 films with different microstructures," *Appl. Surf. Sci.*, vol. 345, pp. 232–237, 2015.

[66] M. Jiang, X. Cao, S. Bao, H. Zhou, and P. Jin, "Regulation of the phase transition temperature of VO2 thin films deposited by reactive magnetron sputtering without doping," *Thin Solid Films*, vol. 562, pp. 314–318, 2014.

[67] X. Liu, S.-W. Wang, F. Chen, L. Yu, and X. Chen, "Tuning phase transition temperature of VO2 thin films by annealing atmosphere," *J. Phys. D. Appl. Phys.*, vol. 48, no. 26, p. 265104, 2015.

[68] T. Chang *et al.*, "Facile and low-temperature fabrication of thermochromic Cr2O3/VO2 smart coatings: enhanced solar modulation ability, high luminous transmittance and UV-shielding function," *ACS Appl. Mater. Interfaces*, vol. 9, no. 31, pp. 26029–26037, 2017.

[69] G. Sun, X. Cao, X. Gao, S. Long, M. Liang, and P. Jin, "Structure and enhanced thermochromic performance of low-temperature fabricated VO2/V2O3 thin film," *Appl. Phys. Lett.*, vol. 109, no. 14, p. 143903, 2016.

[70] G. Sun *et al.*, "Low-temperature deposition of VO2 films with high crystalline degree by embedding multilayered structure," *Sol. Energy Mater. Sol. Cells*, vol. 161, pp. 70–76, 2017.

[71] M. Currie, M. A. Mastro, and V. D. Wheeler, "Characterizing the tunable refractive index of vanadium dioxide," *Opt. Mater. Express*, vol. 7, no. 5, pp. 1697–1707, 2017.

[72] X. Lv, Y. Cao, L. Yan, Y. Li, and L. Song, "Atomic layer deposition of VO2 films with Tetrakis-dimethyl-amino vanadium (IV) as vanadium precursor," *Appl. Surf. Sci.*, vol. 396, pp. 214–220, 2017.

[73] G. Y. Song, C. Oh, S. Sinha, J. Son, and J. Heo, "Facile phase control of multivalent vanadium oxide thin films (V2O5 and VO2) by atomic layer deposition and postdeposition annealing," *ACS Appl. Mater. Interfaces*, vol. 9, no. 28, pp. 23909–23917, 2017.

[74] L. Mathevula *et al.*, "Thermochromic VO2 on Zinnwaldite Mica by pulsed laser deposition," *Appl. Surf. Sci.*, vol. 314, pp. 476–480, 2014.

[75] B. N. Masina *et al.*, "Phase-selective vanadium dioxide (VO2) nanostructured thin films by pulsed laser deposition," *J. Appl. Phys.*, vol. 118, no. 16, p. 165308, 2015.

[76] S. Lafane *et al.*, "Direct growth of VO2 nanoplatelets on glass and silicon by pulsed laser deposition through substrate temperature control," *Thin Solid Films*, vol. 632, pp. 119–127, 2017.

[77] L. Zhao *et al.*, "Solution-processed VO 2-SiO 2 composite films with simultaneously enhanced luminous transmittance, solar modulation ability and anti-oxidation property," *Sci. Rep.*, vol. 4, p. 7000, 2014.

[78] L. Whittaker, T.-L. Wu, C. J. Patridge, G. Sambandamurthy, and S. Banerjee, "Distinctive finite size effects on the phase diagram and metal--insulator transitions of tungsten-doped vanadium (IV) oxide," *J. Mater. Chem.*, vol. 21, no. 15, pp. 5580–5592, 2011.

[79] M. M. Seyfouri and R. Binions, "Sol-gel approaches to thermochromic vanadium dioxide coating for smart glazing application," *Sol. Energy Mater. Sol. Cells*, vol. 159, pp. 52–65, 2017.

[80] N. R. Mlyuka, G. A. Niklasson, and C. G. Granqvist, "Mg doping of thermochromic VO2 films enhances the optical transmittance and decreases the metal-insulator transition temperature," *Appl. Phys. Lett.*, vol. 95, no. 17, pp. 1–4, 2009, doi: 10.1063/1.3229949.

[81] T. D. Manning, I. P. Parkin, M. E. Pemble, D. Sheel, and D. Vernardou, "Intelligent Window Coatings: Atmospheric Pressure Chemical Vapor Deposition of Tungsten-Doped Vanadium Dioxide," *Chem. Mater.*, vol. 16, no. 4, pp. 744–749, 2004, doi: 10.1021/cm034905y.

[82] S. Taylor, Y. Yang, and L. Wang, "Vanadium dioxide based Fabry-Perot emitter for dynamic radiative cooling applications," *J. Quant. Spectrosc. Radiat. Transf.*, vol. 197, pp. 76–83, 2017.

[83] M. A. Kats *et al.*, "Ultra-thin perfect absorber employing a tunable phase change material," *Appl. Phys. Lett.*, vol. 101, no. 22, p. 221101, 2012.

[84] A. S. Barker Jr, H. W. Verleur, and H. J. Guggenheim, "Infrared optical properties of vanadium dioxide above and below the transition temperature," *Phys. Rev. Lett.*, vol. 17, no. 26, p. 1286, 1966.

[85] D. A. G. Bruggeman, "Dielectric constant and conductivity of mixtures of isotropic materials," *Ann. Phys.(Leipzig)*, vol. 24, pp. 636–679, 1935.

[86] S. Molesky, C. J. Dewalt, and Z. Jacob, "High temperature epsilon-near-zero and epsilon-near-pole metamaterial emitters for thermophotovoltaics," *Opt. Express*, vol. 21, no. 101, pp. A96--A110, 2013.

[87] Z. M. Zhang, *Nano/microscale heat transfer*. Springer, 2007.

[88] L. P. Wang, S. Basu, and Z. M. Zhang, "Direct and indirect methods for calculating thermal emission from layered structures with nonuniform temperatures," *J. Heat Transfer*, vol. 133, no. 7, 2011.

[89] H. Wang, X. Liu, L. Wang, and Z. Zhang, "Anisotropic optical properties of silicon nanowire arrays based on the effective medium approximation," *Int. J. Therm. Sci.*, vol. 65, pp. 62–69, 2013, doi: 10.1016/j.ijthermalsci.2012.08.018.

[90] E. D. Palik, *Handbook of optical constants of solids*, vol. 3. Academic press, 1998.

[91] H. H. Li, "Refractive index of silicon and germanium and its wavelength and temperature derivatives," *J. Phys. Chem. Ref. Data*, vol. 9, no. 3, pp. 561–658, 1980.

[92] D. Chandler-Horowitz and P. M. Amirtharaj, "High-accuracy, midinfrared (450 cm- 1⩽ $ω$⩽ 4000 cm- 1) refractive index values of silicon," *J. Appl. Phys.*, vol. 97, no. 12, p. 123526, 2005.

[93] L. P. Wang, B. J. Lee, X. J. Wang, and Z. M. Zhang, "Spatial and temporal coherence of thermal radiation in asymmetric Fabry--Perot resonance cavities," *Int. J. Heat Mass Transf.*, vol. 52, no. 13–14, pp. 3024–3031, 2009.

[94] X. Fang, C. Y. Zhao, and H. Bao, "Study on a Novel Selective Solar Absorber With Surface Ultrathin Metal Film," in *International Conference on Micro/Nanoscale Heat Transfer*, 2016, vol. 49651, p. V001T05A009.

[95] "Atmospheric Transmittance," *IR Transmission Spectra, Gemini Observatory*, 2012. http://www.gemini.edu/ sciops/telescopes-and-sites/observing-condition-constraints/ir-transmission-spectra.

[96] R. Chen *et al.*, "Shape-controlled synthesis and influence of W doping and oxygen nonstoichiometry on the phase transition of VO 2," *Sci. Rep.*, vol. 5, p. 14087, 2015.

[97] L. Hongwei *et al.*, "Size effects on metal-insulator phase transition in individual vanadium dioxide nanowires," *Opt. Express*, vol. 22, no. 25, pp. 30748–30755, 2014.

[98] L. Kang *et al.*, "Asymmetrically modulating the insulator--metal transition of thermochromic VO2 films upon heating and cooling by mild surface-etching," *Appl. Surf. Sci.*, vol. 311, pp. 676–683, 2014.

[99] X. Wang *et al.*, "Tunable Bragg filters with a phase transition material defect layer," *Opt. Express*, vol. 24, no. 18, pp. 20365–20372, 2016.

[100] D. F. Edwards and E. Ochoa, "Infrared refractive index of silicon," *Appl. Opt.*, vol. 19, no. 24, pp. 4130–4131, 1980.

[101] F. A. Johnson, "Lattice absorption bands in silicon," *Proc. Phys. Soc.*, vol. 73, no. 2, p. 265, 1959.

[102] J. H. Holland and others, *Adaptation in natural and artificial systems: an introductory analysis with applications to biology, control, and artificial intelligence*. MIT press, 1992.

[103] H. W. Verleur, A. S. Barker Jr, and C. N. Berglund, "Optical properties of V O 2 between 0.25 and 5 eV," *Phys. Rev.*, vol. 172, no. 3, p. 788, 1968.

[104] K. Sun *et al.*, "VO2 thermochromic metamaterial-based smart optical solar reflector," *ACS Photonics*, vol. 5, no. 6, pp. 2280–2286, 2018.

[105] M. Tazawa, P. Jin, K. Yoshimura, T. Miki, and S. Tanemura, "New material design with V1- xWxO2 film for sky radiator to obtain temperature stability," *Sol. energy*, vol. 64, no. 1–3, pp. 3–7, 1998.

[106] M. Tazawa, P. Jin, and S. Tanemura, "Thin film used to obtain a constant temperature lower than the ambient," *Thin Solid Films*, vol. 281, pp. 232–234, 1996.

[107] W. J. M. Kort-Kamp, S. Kramadhati, A. K. Azad, M. T. Reiten, and D. A. R. Dalvit, "Passive radiative 'thermostat' enabled by phase-change photonic nanostructures," *ACS Photonics*, vol. 5, no. 11, pp. 4554–4560, 2018.

[108] M. Ono, K. Chen, W. Li, and S. Fan, "Self-adaptive radiative cooling based on phase change materials," *Opt. Express*, vol. 26, no. 18, pp. A777--A787, 2018.

[109] A. Hendaoui, N. Émond, S. Dorval, M. Chaker, and E. Haddad, "VO2-based smart coatings with improved emittance-switching properties for an energy-efficient near room-temperature thermal control of spacecrafts," *Sol. energy Mater. Sol. cells*, vol. 117, pp. 494–498, 2013.

[110] S. Taylor, L. Long, R. McBurney, P. Sabbaghi, J. Chao, and L. Wang, "Spectrally-selective vanadium dioxide based tunable metafilm emitter for dynamic radiative cooling," *Sol. Energy Mater. Sol. Cells*, vol. 217, p. 110739, 2020.

[111] S. Taylor, L. Long, and L. Wang, "Fabrication and characterization of furnace oxidized vanadium dioxide thin films," *Thin Solid Films*, vol. 682, pp. 29–36, 2019.

[112] H. Alshehri, Q. Ni, S. Taylor, R. McBurney, H. Wang, and L. Wang, "Solar Thermal Energy Conversion Enhanced by Selective Metafilm Absorber under Multiple Solar Concentrations at High Temperatures," 2019.

[113] N. Shen *et al.*, "Lowered phase transition temperature and excellent solar heat shielding properties of well-crystallized VO 2 by W doping," *Phys. Chem. Chem. Phys.*, vol. 18, no. 40, pp. 28010–28017, 2016.

[114] N. Wang, S. Liu, X. T. Zeng, S. Magdassi, and Y. Long, "Mg/W-codoped vanadium dioxide thin films with enhanced visible transmittance and low phase transition temperature," *J. Mater. Chem. C*, vol. 3, no. 26, pp. 6771–6777, 2015.

[115] F. C. Case, "Modifications in the phase transition properties of predeposited VO2 films," *J. Vac. Sci. Technol. A Vacuum, Surfaces, Film.*, vol. 2, no. 4, pp. 1509–1512, 1984.

[116] Y.-X. Ji, S.-Y. Li, G. A. Niklasson, and C. G. Granqvist, "Durability of

thermochromic VO2 thin films under heating and humidity: Effect of Al oxide top coatings," *Thin Solid Films*, vol. 562, pp. 568–573, 2014.

[117] C. J. Massina and D. M. Klaus, "Defining a Discretized Space Suit Surface Radiator With Variable Emissivity Properties," *J. Therm. Sci. Eng. Appl.*, vol. 7, no. 4, 2015.

[118] D. Malarde *et al.*, "Optimized atmospheric-pressure chemical vapor deposition thermochromic VO2 thin films for intelligent window applications," *ACS omega*, vol. 2, no. 3, pp. 1040–1046, 2017.

[119] S. Taylor, J. Chao, L. Long, N. Vlastos, and L. Wang, "Temperature-dependent Optical Characterization of VO2 Thin Film Prepared from Furnace Oxidation Method," *ES Mater. Manuf.*, vol. 6, pp. 62–67, 2019.

VITA

SYDNEY TAYLOR

Sydney Taylor was born in Lafayette, Indiana in 1991. She received her Bachelor's degree from Purdue University in 2013 in aeronautical and astronautical engineering. Sydney began her PhD in aerospace engineering at Arizona State University in Fall 2014 and joined Dr. Liping Wang's research group in Spring 2015. Her research focuses on dynamic radiative thermal management and optical force modulation with tunable materials. During her PhD study, Sydney has published four first-authored journal papers and has presented at over 10 international conferences, such as the *8th International Symposium on Radiative Transfer*, *ASME International Mechanical Engineering Congress and Exposition, NASA Thermal and Fluids Analysis Workshop*, and *International Conference on Environmental Systems*. She received the 1st Place Award in the ICES2018 student poster competition, the Most Innovative Experimental Poster award at IMECE2019, and a Spring 2020 Co-Op Award for her NASA Pathways internship. She has also been a NASA Space Technology Research Fellow since Fall 2016 and has received numerous travel grants through the ASU GPSA, Graduate College, and NSF. Besides, she has been active in a number of professional service activities, such as reviewing manuscripts and mentoring students in the FURI and Space Grant undergraduate research programs. She also is involved in several community service activities, including Big Brothers Big Sisters of Arizona and ASU's Martin Luther King Jr. Day committee.